BIORENEWEABLE POLYMER NANOCOMPOSITES: A STUDY OF THE DESIGN SPACE AVAILABLE FOR CELLULOSE NANOCRYSTAL/POLY(3-HYDROXYBUTYRATE) NANOCOMPOSITES

A Dissertation
Presented to
The Academic Faculty

By

Stephanie Lin

In Partial Fulfillment
of the Requirements for the Degree
Doctor of Philosophy in the School of Materials Science and Engineering

Georgia Institute of Technology
August 2014

BIORENEWABLE POLYMER NANOCOMPOSITES: A STUDY OF THE DESIGN SPACE AVIALABLE FOR CELLULOSE NANOCRYSTAL/POLY(3-HYDROXYBUTYRATE) NANOCOMPOSITES

Approved by:

Dr. Meisha Shofner, Advisor
School of Materials Science and Engineering
Georgia Institute of Technology

Dr. Dong Qin
School of Materials Science and Engineering
Georgia Institute of Technology

Dr. Yulin Deng
School of Chemical and Biomolecular Engineering
Georgia Institute of Technology

Dr. Donggang Yao
School of Materials Science and Engineering
Georgia Institute of Technology

Dr. Karl Jacob
School of Materials Science and Engineering
Georgia Institute of Technology

Date Approved: May 9th 2014

ACKNOWLEDGEMENTS

I would like to express my sincerest thanks and gratitude to my advisor, Prof. Meisha Shofner, for her amazing support and guidance during my research. I would like to thank my committee members Dr. Yulin Deng, Dr. Karl Jacob, Dr. Dong Qin and Dr. Donggang Yao for their input towards my PhD research and thesis.

I would like to thank the people at the Institute of Paper Science and Technology, and in particular Dr. Norman Marsolan for providing amazing support for my research. I would also like to thank Michael Zemo and Steven Sauerbrunn from Mettler Toledo for providing so much help with the set up and troubleshooting of the Flash DSC. I would also like to thank my current labmates Cait Meree, Prateek Verma for insightful discussions and support. I would also like to thank my former group member Ji Hoon Lee for helping me with getting started in the Shofner Lab. I would also like to thank Varun Gopal for helping me with the hot stage experiments.

I am thankful for my friends and family, who have been a constant source of support and encouragement for me. I would like to also acknowledge and thank Ted Conrad, who has been a pillar of support for me. Without his daily words of encouragement and guidance, this endeavor would not have been possible for me.

TABLE OF CONTENTS

LIST OF TABLES

LIST OF FIGURES

LIST OF SYMBOLS AND ABBREVIATIONS

PHB	Poly(3-hydroxybutyrate)
CNC	Cellulose nanocrystals
RAF	Rigid Amorphous Fraction
OMMT	Organophilic montmorillonite
PHBV	Poly(3-hydroxybutyrate-co-3-hydroxyvalerate)
HDPE	High density polyethylene
FTIR	Fourier transform-infrared spectroscopy
NMR	Nuclear magnetic resonance
CNT	Carbon nanotube
$CaCO_3$	Calcium carbonate
T_g	Glass transition temperature
DSC	Differential scanning calorimetry
iPP	Isotactic polypropylene
CD-glasses	Conformational disordered glasses
XRD	X-ray diffraction
PET	polyethylene terephthalate
MAF	mobile amorphous fraction
TMDSC	Temperature modulated DSC
PS	polystyrene
MMT	montmorillonite
PLLA	poly(l-lactide) acid
FDSC	Fast scanning differential scanning calorimetry
PA	Poly amide
PLA	polylactic acid

TEMPO	2,6,6-tetramethyl-piperidinyl-oxyl
PHA	polyhydroxyalkanoates
α form	helix conformation of PHB
β form	planar zigzag conformation of PHB
SC-EtOH	Solvent casting with ethanol
SC-H_2O	Solvent casting with water
AS	Anti-solvent
ASCM	Anti-solvent compression molding
T_m	peak melting temperature
T_c	peak crystallization temperature
X_c	weight fraction of crystalline component
ΔH_m	enthalpy of the melting peak
m_c	nanocomposite weight
m_p	weight of PHB in the nanocomposite
MRR	melting recrystallization-remelting
CAB	cellulose acetate butyrate
$\alpha(t)$	extent of transformation at time t
n	Avrami constant
k	kinetic constant
$t^{0.5}$	time at 50% transformation
VH-CC	Variable heating- constant cooling
CH-VH	Constant heating-variable heating
IC-VH	Isothermal crystallization-variable heating
T_{on}	melting onset temperature
$c_{p,solid}$	heat capacity of the solid PHB
$c_{p,liquid}$	heat capacity of the liquid PHB

T_{RAF}	enthaplic relaxation of RAF temperature
DMA	dynamic mechanical analysis
E’	storage modulus
E”	loss modulus
δ	phase lag between stress and strain(sinusoidal loading)

SUMMARY

This research is directed toward determining the design space that is available for cellulose nanocrystals /poly(3-hydroxybutyrate)(CNC/PHB) composites. In order to develop this understanding, the processing-structure-properties relationships of CNC/PHB nanocomposites were examined at several different steps in a stepwise processing method. The as-processed morphology of solvent cast (SC) and anti-solvent compression molded (ASCM) samples were examined using DSC, optical microscopy and ATR-FTIR and the effect of processing and CNC addition on the isothermal and nonisothermal crystallization was examined using DSC, hot stage microscopy, and a novel fast scanning chip calorimeter, the Flash DSC. The results show that the addition of water during SC processing significantly reduced the rate of crystallization at both isothermal and nonisothermal conditions. This reduction in crystallization rate was due to the presence of water suppressed the intramolecular hydrogen bonding. When CNCs were added, the overall crystallization kinetics were increased for isothermal crystallization and crystallization upon cooling occurred at higher temperature. These results indicated CNCs act as a nucleating agent. Even though the overall kinetics of crystallization were increased with CNC addition, the growth rate of the spherulites was reduced with the addition of CNCs.

From the variable heating experiments performed on the Flash DSC, the addition of CNCs suppressed the reorganization behavior of PHB upon heating. The isothermal crystallization experiments performed on the Flash DSC examined in how the RAF, MAF and crystallinity change during the initial stages of primary crystallization with the addition of nanofillers. Results from the isothermal experiments showed that during short isothermal hold times the RAF parallels the crystallinity whereas for long isothermal hold times the amount of RAF decreased significantly. The effect of processing on the

mechanical behavior of CNC/PHB composites was examined for one SC processing method and the ASCM processing method the viscoelastic nature of the composite was influenced by the processing method. The addition of CNCs increased the strain to failure of both types of samples initially but as storage time increased, embrittlement caused decreases in the strain to failure of samples from both processing methods. However the ASCM processing method slowed down the embrittlement processs more due to the reduction in mobility of the amorphous content. The knowledge that was obtained from this work can be used when designing processing protocols and heat treatments for PHB-based nanocomposites materials to allow greater control over crystallization processes and mechanical properties expanding opportunities for materials design.

CHAPTER 1

INTRODUCTION

Polymer nanocomposites are polymer-based materials with a filler material having at least one dimension in the nanometer range. These materials have received great interest due to the ability of a small amount of nanofiller to drastically change the properties of the polymer matrix.[1–3] These property differences have motivated much research to describe how the structure of the polymer is altered by the addition of nanofillers.[2,4,5] Most of this work has been focused on creating stronger and more durable polymer-based materials;[2] however, in the last decade, research in the development of biodegradable nanocomposites made of renewable resources has increased.[6,7] Biodegradable polymer nanocomposites are made of materials that can be decomposed by microorganisms into smaller products such as carbon compounds and water;[8] therefore, these materials provide environmental advantages such as reduced ecological impact when compared to the petroleum-based polymers. Poly(3-hydroxybutyrate) (PHB) is one of the biodegradable polymers that is currently being used in the development of the next generation of renewable biodegradable nanocomposites,[9–14] and cellulose nanocrystals (CNCs) are a type of biodegradable nanofiller that has generated research interest as a reinforcing nanofiller.[4,15,16] This research was directed at developing a bio-based, biodegradable nanocomposite using PHB and CNCs through examining the relationship between the crystallization behavior of CNC/PHB nanocomposite and the resulting properties as a function of the different processing conditions. Therefore, the objectives of this research were:

1. Examination of how component interactions and nanocomposite morphology evolve through a series of step-wise processing operations.

2. Characterization of the semi-crystalline structure formed in CNC/PHB composites to understand interfacial structure formed during isothermal crystallization.
3. Describe the structure-property relationships in CNC/PHB systems through mechanical performance.

Based on the objectives, this work has been structured into 3 studies presented in Chapters 3-5 and in Chapter 2 background relevant to the research is reviewed. In Chapter 2 research results concerning polymer nanocomposites with amorphous and semicrystalline matrices and crystallization behavior in semicrystalline polymers are discussed. A general description of CNCs and how they are synthesized are described in this chapter, and background regarding the different crystalline phases and crystallization behavior of PHB are also discussed. Chapter 3 examines how the processing affected the nanocomposite morphology by characterizing the change in the structure at different steps in a step-wise processing method. Studies of how the addition of nanoparticles affected the evolution of the semicrystalline structure of PHB during isothermal and nonisothermal conditions is described in Chapter 4. In Chapter 5, the changes in mechanical behavior of CNC/PHB nanocomposites are compared neat PHB, and the effect of nanoparticle addition as well as processing methods on the mechanical properties are discussed. The overall conclusion of this work and the future recommendations are reported in Chapter 6.

CHAPTER 2

BACKGROUND

How the addition of nanoparticles and the processing can affect the crystallization behavior of a semicrystalline polymer is discussed in this chapter. The literature relevant to polymer nanocomposites and the different methods used to process nanocomposites is reviewed. In particular, the concept of an interphase and its role in the material properties of a nanocomposite is examined. Mesophases and the rigid amorphous fraction (RAF) are described in this chapter, and their role in the evolution of a semicrystalline polymer is described. The method of characterizing mesophases and RAF is reviewed. A review of the literature relevant to current state of research of fast scanning calorimetry is examined. Also background regarding the nanoparticle (CNC) and matrix (PHB) being used in this research is discussed.

2.1 **Nanocomposites: An Introduction**

Nanocomposites are defined as composite materials with a matrix containing fillers where at least one of the dimensions of the fillers is less than 100nm. Nanocomposites are important because a small addition of nanofiller can drastically improve the properties of a material.[2,17,18] Nanocomposites first generated research interest in the late 1980s and early 1990s when researchers at the Toyota Central Research Laboratories reported that the addition of a relatively small amount of clay nanofiller in Nylon-6 resulted in a significant increase in the storage modulus at elevated temperatures and increased the heat distortion temperature.[19] The addition of nanofillers has also been shown to increase mechanical properties such as flexural strength,[20,21] fracture toughness[22,23] and impact resistance.[24] Beyond mechanical properties, nanofillers have been added to epoxy matrices to reduce thermal expansion characteristics allowing for the system to be used for cryogenic applications.[25,26] In a likewise manner, the

addition of nanofillers to biodegradable polymers has decreased the rate of biodegradation in soil.[27,28] For organophilic montmorillonite/poly(3-hydroxybutyrate-co-3-hydroxyvalerate) (OMMT/PHBV) nanocomposites, the authors attributed the decrease in the biodegradation rate of the composite to the interaction between the PHBV and the silicate layers of the OMMT, restricting the segmental motion at the interface. This restricted segmental motion formed a more tortuous path for the degrading enzymes, thus inhibiting the degradation of the PHBV.[28] Similar behavior was observed when OMMT was added to poly(butylene succinate) (PBS), the rate of biodegradation was decreased with OMMT addition.[27] However it is worth noting that the authors did mention the 3 wt. % OMMT/PHBV degraded more rapidly than the neat PHBV in the first 350 hours, and the authors attributed this to lower crystallinity of the 3% OMMT/PHBV composite.

The enhanced material properties of polymer nanocomposites have often been attributed to the interphase region, which is formed by the interaction between the polymer chains and the nanofiller.[2,29–31] Most of the interactions between the polymer chain and the nanofiller involve adsorption of the polymer onto the nanofiller.[32] Figure 2.1 is a schematic of the interphase region with different possible interactions that are associated with the interphase. This interfacial region has been described before in traditional composite theory, but in nanocomposites, the large surface area to volume ratio of the nanofiller results in a greater amount of interphase. Also, the geometry of the nanofiller can play an important role in the structure of nanocomposites.

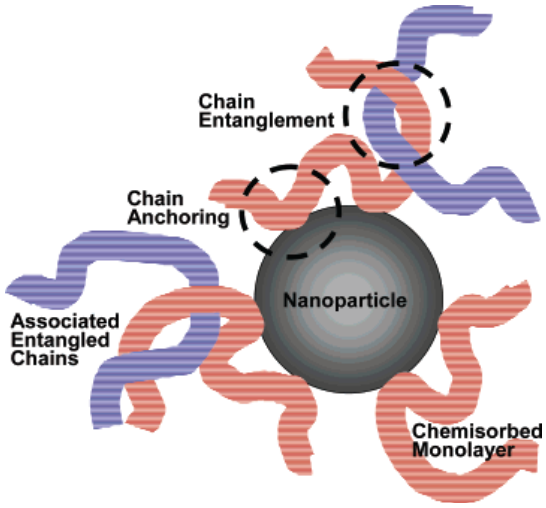

Figure 2.1. Schematic of the interphase.[33]

The geometry of the particle can affect the ordering behavior of a polymer system through interfacial interactions because the radius of gyration of a polymer is on the same length scale as at least one dimension of the nanofiller.[34,35] There are 3 common nanoparticle shapes: particulate, fibrous and plate-like nanoparticles.[2,3] Particulate shaped nanoparticles have a spherical shape or polyhedral shape.[3] Examples of the nanofillers with particulate geometry include silica and carbon black. For the fibrous and plate-like nanoparticles, the surface area to volume ratios are determined by the radius and the thickness of particle, respectively.[3] For the fibrous particle geometry, carbon nanotubes are one of the most well-known nanoparticles used for polymer nanocomposites. For the plate-like particle geometry, examples of nanoparticles used in polymer nanocomposites are montmorillonite[27,28] and graphene sheets.[36,37] Figure 2.2 illustrates how the dimensionality of crystal growth decreases as the dimensionality of the filler increases. For the 1 and 2-D fillers, polymer chains must root or adsorb onto the surface of the filler and begins to crystallize whereas for the 0-D fillers, the crystallites grow in all directions and form spherulites.[38] In isothermal crystallization experiments performed where high density polyethylene was processed with carbon nanofillers with different dimensionality

(0-D, 1-D, 2-D), the crystallization rate decreased and induction time increased as the dimensionality of the nanofiller decreased; however, nonisothermal crystallization experiments on the same carbon nanofiller/HDPE system indicated that the 0-D nanoparticle had the greatest crystallization rate. The authors attributed these differences to differences in the crystallization mechanisms for the isothermal and nonisothermal crystallization condtions.[38] During nonisothermal crystallization, the nucleating effect of the 2-D systems were slower than the 0-D systems due to steric effects at the beginning of non-isothermal crystallization whereas during isothermal crystallization adsorption of the polymer chain onto the surface changes the dimensionality of crystal growth. [38]

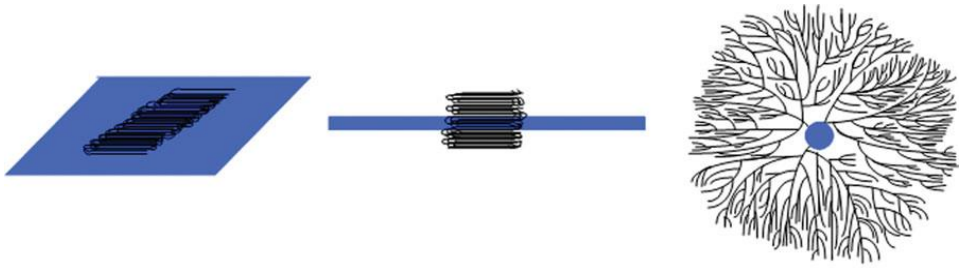

Figure 2.2. Schematic of the crystal as a function of nanoparticle dimension.[38]

The dispersion of nanofillers within the polymer matrix can influence the material properties of the nanocomposite. For plate-like particles, the particles have a tendency to form ordered stacks with small interlayer spacings. If no polymer can penetrate between individual particles, the properties of nanocomposite would be similar to that of the microcomposite.[2] If the polymer is able penetrate the plate-like particles but an ordered-multilayered structure with an expanded interlayer spacing remains, an intercalated structure is formed. If the plate-like particles are uniformly dispersed and order is

disrupted, an exfoliated structure is formed. The properties of an intercalated and exfoliate nanocomposites with the same nanoparticle loading can differ significantly.

For fibrous particles, the dispersion of the nanoparticle within the matrix and the interactions between the particle and the nanofiller greatly influence the material properties of a nanocomposite. Strong interactions between the nanoparticle and the matrix have resulted in an increase in the elastic modulus of a nanocomposite, whereas weak interactions between the nanofiller and the matrix could result decreased mechanical properties.[39]

In this research, fibrous nanoparticles will be used to make a nanocomposite. Previous research has shown that the fibrous nanoparticles increase the crystallization kinetics more than the spherical nanoparticles do when added into a polymer matrix,[40–42] and fibrous nanoparticles have the best reinforcement efficiency when compared with the other nanoparticle geometries.[5]

2.1.1 Interphase and Matrix-filler interactions

There are two main types of interactions within a nanocomposite, particle-particle interactions and particle-matrix interactions. Particle–particle interactions are as important as polymer-filler interactions in determining the effectiveness of adding a nanofiller into a polymer matrix as a method enhance the material properties.[29] However, the research here concerns nanocomposites with low loadings of nanoparticles, so the polymer-filler interactions and its effect on the material properties of a nanocomposite will be discussed in greater detail.

The formation of the interphase region are determined by the chemical and physical interactions between the polymer and the nanofiller.[2,43–45] The material properties of the interphase differs from that of the polymer matrix and the nanofiller.[29,30] The strength of interactions between the polymer and the matrix can vary from strong bonding such as ionic or covalent bonding to limited interaction.[29,30]

The characteristics of the interphase such as thickness and stiffness are difficult to quantify. Several attempts have been made to quantify these properties through mechanical testing[31] and Fourier transform-infrared spectroscopy (FT-IR),[33] rheology,[46] and nuclear magnetic resonance (NMR)[47] with limited success. Therefore modeling of the interphase and its impact on mechanical properties of a nanocomposite has been an area of research interest. Most of the modeling techniques use theories of adhesion to describe the mechanisms associated with interphase phase formation and to calculate its properties.[30] Most of methods for calculating the strength of the interactions involve calculating the work of adhesion between the polymer and the matrix.[29] The adhesion strength is calculated through a combination of surface tension and interfacial tension.

According to the literature, there is a linear relationship between the calculated work of adhesion and the thickness of the interphase,[29] and the amount of polymer associated with the interphase is related to the specific surface area of the filler. With regards to the relationship between the specific surface area of the nanofiller and a nanocomposite's mechanical behavior, the modulus of nanocomposites show a weak dependence on the specific surface area of the nanocomposite, but the mechanical properties at high deformation such as tensile strength and tensile yield are affected by the specific surface area of the nanofiller.[35] For increased mechanical properties, the interphase must be able to transfer stress from the matrix to the filler. CNCs,[48–50] graphene sheets,[48] and carbon nanotubes (CNTs)[36] are some of the nanoparticles where stress transfer between the nanofiller and the matrix has been detected via structural changes in the nanofiller due to strain.

Improvement to other material properties such as fracture, impact resistance, and heat deflection temperature are also related to the strength of the interactions between the matrix and filler, and stronger polymer-matrix interaction often leads to an increase in these material properties.[44] Modifying the surface of the nanofiller is the easiest method

of altering the interfacial interactions.[29] However, modifying the surface chemistry of a nanofiller also alters the particle-particle interactions. Therefore, the properties of a nanocomposite could be drastically altered by nanoparticle surface modification. Some of most common ways the surface of a nanofiller have been altered include covering the surface of the nanoparticle with a small molecular weight compound to make the surface of the nanofiller nonreactive, using coupling agents to form covalent bonds between the polymer and the matrix, coverage of the filler surface with a polymer capable of interdiffusion with the polymer matrix, and directly changing the surface chemistry of the nanofiller to allow for stronger bond between the matrix and the filler.[29,45] One of the most common examples of making the surface of a nanoparticle non-reactive is to coat the surface with stearic acid. Calcium carbonate ($CaCO_3$) nanoparticles[35] and cellulose whiskers have been coated with stearic acid to form non-reactive during nanocomposite processing.[16]

There can be changes in the thermal behavior associated with the presence of a matrix-filler interaction. Much of the literature has focused on using a shift in the glass transition temperature (T_g) to characterize the nature of a matrix-filler interaction. This shift in the T_g due to the constrained mobility of the polymer adsorbed onto the surface of the nanoparticle,[32] whereas others have observed appearance of a second transition above the T_g.[51] The authors have attributed the appearance of this second T_g to changes in the relaxation behavior of the polymer adhered to the surface of the nanoparticle.

2.1.2 Particle-Particle Interactions

The discussion of particle-particle interactions will be limited to describing the phenomena associated with fiber-reinforced nanocomposite systems since only the fibrous geometry nanoparticles will be used in this research. However aggregation of the nanoparticles is one of the particle-particle interactions that occur regardless of the nanoparticle geometry. Nanoparticle aggregation is one of the major problems that occur

when trying to manufacture nanocomposites because the most improvement in the material properties of a nanocomposite dependent on well dispersed nanoparticles within a polymer matrix.

Aggregation is dependent both on the adhesive forces trying to hold the particles together and forces trying to separate the particles. The main forces used to separate particles are shear and extensional forces.[44] Therefore processing methods such as shear mixing and extrusion are used when making fibrous nanocomposites to prevent agglomeration of the nanoparticles. Surface modification of the nanoparticle, which was discussed in the previous sections, is also another method that is used to prevent aggregation of the nanoparticles.

Percolation is another important concept used to describe particle-particle interactions that can influence the material properties of a nanocomposite. In particular, the percolation threshold, which describes threshold at which one phase forms long–range connectivity within another phase, has been used to describe significant increases in the modulus and conductivity at particular loadings.[52–54] There are several different types of percolation thresholds described in the literature. The geometrical percolation threshold and the mechanical percolation threshold are some of the most common ones described in the literature. The geometrical percolation threshold describes the loading of nanoparticles at which nanoparticles are in physical contact with one another, whereas the mechanical percolation threshold is similar to geometrical percolation threshold with an extended radius to account for the interphase.[55] Mechanical percolation is also sometimes described as the rheological percolation threshold. The electrical percolation threshold refers the nanoparticle loading of a conductive nanoparticle at which the nanoparticles are electrically connected to one another through physical contact or through separations less than that needed for electron tunneling or hopping.[56] The geometry of the nanofiller plays a role in the geometrical percolation threshold, thus

influencing the mechanical percolation threshold and electrical percolation threshold. A significantly smaller amount of fibrous nanoparticle is needed to create a mechanically percolated system when compared to a particulate nanoparticle.[5]

When a nanoparticle is used for mechanical reinforcement, a mechanically percolated system can have a modulus several orders of magnitude greater than a system containing isolated nanoparticles,[17,57] and the greatest increase in the modulus is seen at temperatures above the glass transition temperature.[31] In addition to mechanical percolation, bonding between particles can create a network which provides addition reinforcement.

2.1.3 Nanocomposites with CNCs as nanofiller

When CNCs are added into a semicrystalline polymer matrix such as iPP, the CNCs can act as nucleating agents [16,57] and also induce the formation of the β phase of iPP Often times, when high loadings of CNCs are added into a matrix, CNCs have shown strong hydrogen bonding between particles, which results in significant increases in the tensile strength and the modulus. This hydrogen-bonded network can be enhanced or destroyed based upon processing. For CNCs, melt mixing (mixing CNCs into a polymer melt) tends to prevent the particle–particle interactions, whereas evaporation casting processes tend to increase the hydrogen bonding between CNCs.[58] When 6 wt.% CNC was added to iPP and the sample was processed using solvent casting methods, the storage modulus of the sample increased significantly at temperatures above T_g and the value of T_g increased, suggesting the mechanical coupling between the iPP crystallites and the CNC occurred.

2.1.4 Nanocomposites with PHB as the matrix

PHB and PHB-based copolymers have been used as the matrix for many different nanocomposites. Often times the PHB-based polymer are used in the development of

biomedical based material because of its biocompability and biodegradability. The addition of nanofillers into PHB has been shown to control the structure in ordering and to control the rate of biodegradation by creating a more tortuous path for the enzyme to diffusion into the material[59–61] or to increase the biocompability.[12,61] Many different types of nanofillers have been added into PHB, and the changes in the material properties are dependent type of nanoparticle added. The addition of OMMT into PHB and cellulosic materials into PHB have been studied extensively. The effect of adding different types of OMMT on the crystallization behavior of PHB has been examined and a retarded crystallization effect was observed with OMMT addition during non-isothermal experiments, and a slower rate of crystallization was observed during isothermal crystallization experiments.[62] When OMMT is added to PHBV, the β phase of PHBV was formed on the surface of the OMMT particles during processing, and this β phase acted as a primary nucleation center for the epitaxial growth of the β-phase. However after annealing, this β-form was transformed into the α-form, leading to an enhanced total crystallinity of the polymer. When cellulosic particles such as microcrystalline cellulose were added, the rate of crystallization was increased during non-isothermal crystallization and the morphology of PHB changed with the different loadings of the microcrystalline cellulose particles .[63] In a likewise manner, when starch was blended with PHB there was a significant reduction in the size of the spherulites and significant improvements in the thermal and mechanical properties of the material and the authors attributed this improvement enhanced hydrogen bonding between the PHB and the starch.[64]

2.2 **Semicrystalline Polymers and Nanocomposites**

In the proposed research, the crystallization behavior of PHB, a semicrystalline polymer, will be studied. Therefore in this section, the behavior of semicrystalline polymers will be discussed in greater detail. First the concept of the semicrystalline polymer will be described. Then, the different phases and type of crystallization behavior

will be discussed in greater detail. Also the effect of nanoparticle addition and processing will be discussed.

2.2.1 Description of Semicrystalline polymers

Semicrystalline polymers have been described in terms of two phases: a crystalline component and an amorphous component. Generally, they do not crystallize completely, and processing and thermal treatment play a role in the development of the semicrystalline structure. The structure of a semicrystalline polymer is often characterized through combination of structural and thermal analysis. Differential scanning calorimetry (DSC) is a thermal analysis technique often used to identify the important changes in the molecular dynamics associated with the amorphous and crystalline components, and either FT-IR or X-ray diffraction (XRD) is used to identify the crystal phases present in a semicrystalline polymer.

In recent years, the description of semicrystalline polymers has begun to expand to describe semicrystalline structure at different length scales. Semicrystalline polymers are now described as linear flexible macromolecules in a metastable nanophase structure. In this description, the linear flexible macromolecules organize themselves into crystalline and amorphous regions, and because a single macromolecule can cross the amorphous crystalline interphase several times, portions of the crystalline component are coupled with the amorphous component.[65] This region has dimensions within the nanometer range, and this nanophase is often times a described as the RAF.[66] In the following sections, the concept of a mesophase and the RAF will be discussed in greater detail.

2.2.2 Nucleating effect of nanoparticles

Addition of nanoparticles to a semicrystalline polymer matrix can increase the rate of nucleation within the polymer because the nanoparticle can lower the energy needed for crystallization by creating heterogeneous sites for nucleation.[2] This phenomenon is often observed through performing nonisothermal and isothermal

crystallization experiments using DSC. In nonisothermal experiments, the melting behavior of semicrystalline polymers with nanoparticles has been shown to differ from that of the neat polymer. In experments where CNCs were added to isotactic polypropylene (iPP), double melting peaks were observed for samples where CNCs were added to the matrix, whereas only a single melting peak was observed for the neat iPP sample. The authors attributed this behavior to the nucleation effect of the CNCs creating less stable crystallites upon cooling.[16] Additionally, a change in crystal phase was observed in some samples. This change in the crystalline phase from predominantly α-phase to β-phase was observed primarily in samples where the CNCs were either aggregated or surface coated with phosphoric ester.[16] The CNCs with grafted maleated PP chains did not have any of the β-phase present.

Nanoparticles have also been shown to modify the crystalline phase that forms, and often times physical and topological factors determine the nucleation effects of fillers. In a study where CNCs with different surface treatments were mixed into iPP, the resulting crystalline phases and melting behavior differed based upon the surface treatment. For the untreated CNCs and the CNCs coated with a phosphoric ester, a β-phase was observed from the X-ray diffraction patterns.[16] This β-phase has also been observed in iPP when stearic acid coated carbonate nanoparticles have been added to iPP.[67] The authors have attributed the formation of the β-phase to the hydrophilic surface of the nanoparticle altering the energy needed to preferentially form the β-phase crystal structure over the α-phase structure, which is the crystalline phase predominately observed in iPP.[16,67]

2.2.3 Mesophases

A mesophase is described as a state of matter between liquid and a solid. There are three types of mesophases: liquid crystals, plastic crystals, and condis crystals or conformational disordered glasses (CD-glasses).[66,68] Of these three different types of

mesophases, the condis crystal/CD-glass is the mesophase of interest to this research because of its presence in semicrystalline polymer systems. Condis crystals are solid mesophases consisting of flexible molecules that can undergo changes in conformation without losing orientational order,[66] and CD-glasses are formed when a semicrystalline polymer is cooled rapidly from the melt to below its T_g, which prevents the polymer chain from crystallizing,[69] or condis crystals below the T_g of the polymer.

The condis crystal is characterized by a large amount of disorder in the conformation of the change but long range order in the position of the chain axis, and this disorder prevents the structure to be described in terms of a unit cell.[69] The presence of a condis mesophase can be detected with XRD or DSC since the mesophase is thermodynamically distinct from the quasi-equilibrium crystal phases commonly observed.[70,71] Often times the XRD patterns produce diffuse scattering rather than distinct Bragg refections.[69]

Many semicrystalline polymers have solid mesophases, including polyethylene terephthalate (PET),[72–74] polyethylene,[65,75] PHB, [76] and different forms of Nylon.[66,77] For some semicrystalline polymer systems, the condis crystal has been described as a metastable crystalline phase which acts as a precursor to a more stable crystallization phase; thus, the presence of a condis crystal is an indication of crystal formation/thickening.[70,71] For iPP, the latent heat needed to transform the mesophase into the monoclinic form is 7% of the monoclinic heat of fusion.[65,78]

2.2.4 Rigid Amorphous Fraction

As stated previously, the RAF is a nanophase present in semicrystalline polymers, and a schematic of how the RAF and mobile amorphous fraction (MAF) are organized within a semicrystalline polymer is shown in Figure 2.3. Although, to describe the RAF as a separate phase is technically incorrect because there is no phase transition that distinguishes the RAF from the MAF.[79] However, the RAF and the MAF can be

distinguished by their molecular mobility. The RAF has less molecular mobility due to coupling with the crystalline regions. Sometimes the difference in the molecular mobility between the MAF and the RAF can be seen through IR[80] or Raman spectroscopy.[81,82] At temperatures above the T_g , the mobility of the RAF associated with this region is lower than that of the mobile amorphous fraction(MAF), therefore a enthaplic relaxation similar to a glass transition is often seen prior to melting. In a study describing the crystalline structure of PHB, the author suggested that the formation of a RAF should be an indication of linkage between the crystalline region and the amorphous region due to an increase in the RAF associated with longer molecules.[83]

Quantifying the amount of RAF present within a polymer system is rather difficult using conventional DSC due to ordering and disordering constantly occur during the heating or cooling of the DSC scan. In a standard DSC experiment, the relaxation behavior of the RAF could overlap with the melting peak associated with the crystalline component;[79] therefore, temperature modulated DSC (TMDSC) is a technique used to separate the reversible and irreversible thermal transitions from one another. RAF has been experimentally observed using TMDSC in several different types of semicrystalline polymers including Nylon 6,[84] polystyrene (PS),[85] PET,[86] and PHB.[71,83,87]

The role of the RAF in the crystallization behavior of a semicrystalline polymer varies from polymer to polymer. For PHB, the formation of RAF goes parallel with crystallization. From standard DSC experiments and TMDSC experiments performed on PHB, the RAF T_g occurs at temperature above the T_g of the MAF. The devitrification of the RAF , crystallization, and the beginning of melting and the reversing melting are closely related.[87,88] Whereas for iPP, mesophase formation is hindered by the RAF of the monoclinic phase.[65]

In a polymer nanocomposite system, the interphase and the RAF are both "nanophases" where the mobility of the polymer is limited. From a dynamic perspective,

RAF and the interphase are similar; however, from a chain entanglement/configuration perspective, the RAF and the nanocomposite interphase are different.[65] From the literature, the addition of fibrous nanoparticles has caused a change in the RAF. For PET, the addition of the CNTs into an electrospun fiber increased the RAF content.[32]

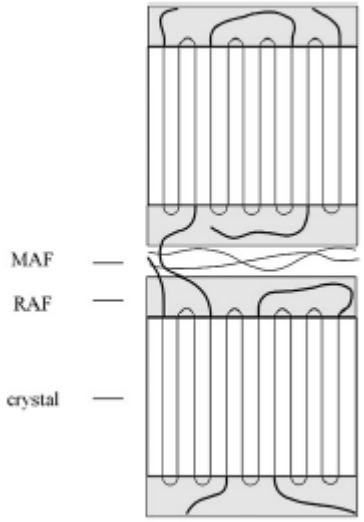

Figure 2.3. Schematic of the organization of the MAF, RAF, and crystal of a PHB, a semicrystalline polymer.[83]

2.2.5 Crystallization in semicrystalline polymers

Crystallization is described as a phase transformation having two different steps, nucleation and growth, and the crystallization rate is the rate at which these two processes occur. Nucleation is the step in which sites of the growth of the crystalline region are formed, and nucleation can be described either as heterogeneous or homogenous. In some semicrystalline polymer systems, adding a nanofiller to the matrix increases the crystallization rate because the nanofiller acts as a heterogeneous nucleation site.[32]

In a study describing the nucleation effect of montmorillonite (MMT) in a Nylon 12,12 matrix, differences the morphology of the MMT/Nylon 12,12 samples were observed when compared with a neat Nylon 12,12 sample.[89] The nanocomposite sample had smaller spherulites when compared to the neat Nylon 12,12, as shown in Figure 2.4. The authors attributed the smaller spherulite size to crystal growth occurring on the surface of the nanofiller. Similar results have been observed for functionalized CNCs in PLA,[90] CNC/poly (3-hydroxybuturate-co-3-hydroxyvalerate) (PHBV), [91] CNT/PP,[92] exfoliated graphite platelets/PHB.[11] Therefore, an increase in crystallization rate has also been used as a measure of nanofiller dispersion quality because it is assumed that rate of crystallization scales with the surface area of the nanofiller and better dispersed nanofillers have more surface area available for crystallization to occur. Several authors have noted at very low loading of nanofiller, the crystallization rate was increased. However at higher nanofiller loadings, the crystallization rate decreases.[32] In addition to an increase in the crystallization rate with nanofiller loading, studies have shown that increasing the nanofiller content initially increased the bulk crystallinity then decreased the bulk crystallinity of the sample at higher nanofiller loadings.[32] For a CNC/PHBV nanocomposite system, the neat PHBV sample had a crystallinity of 58.1%. The 1.0% CNC/PHBV sample had the greatest crystallinity, and as the CNC content was increased further, the crystallinity of the sample was reduced to 53.9% at a loading of 10% CNCs. The author attributed this decrease in bulk crystallinity to the disturbed interactions between the matrix and nanofiller at the higher CNC loadings.[13] For other nanocomposite systems such as CNC/poly(l-lactide) (PLLA), the bulk crystallinity of the matrix was low therefore higher nanofiller loadings increased the bulk crystallinity of the matrix.[90] Thus the effect of nanoparticle loading on the bulk crystallinity of the nanocomposite depended on the crystallinity of the neat polymer matrix. For the proposed research, a polymer

matrix with a relatively high level of crystallinity is be used; therefore, low nanoparticle loadings are used to determine the effect of the loading on the bulk crystallinity.

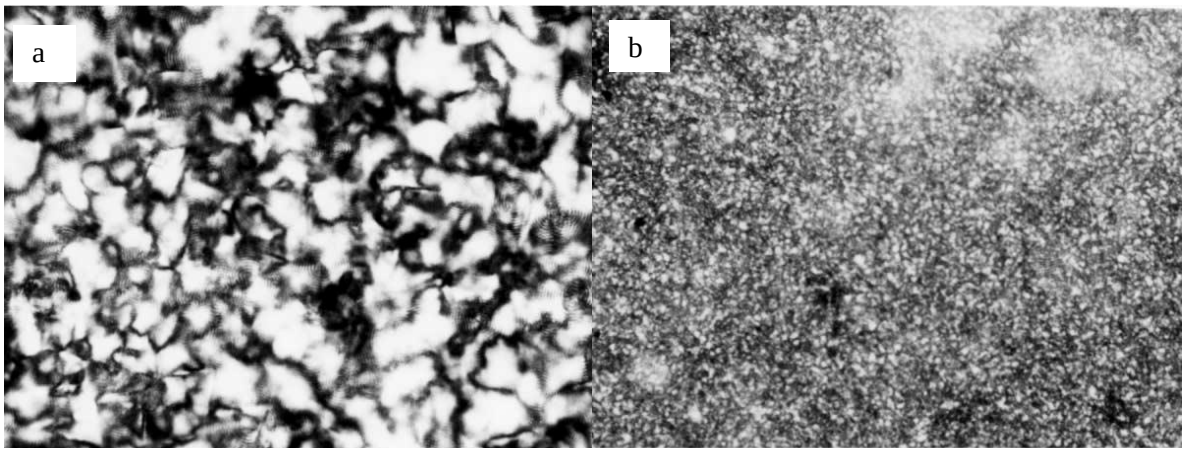

Figure 2.4 Polarized optical microscopy of Nylon12,12 (a), and Nylon 12,12/MMT nanocomposite.[89]

2.3 **Flash DSC**

Characterization of metastable semicrystalline structures by conventional DSC is difficult because these instruments can only heat and cool samples at a rate up to 100 °C/s; therefore, fast scanning differential scanning calorimeters (FSDSCs) are more appropriate tools to study the kinetics of metastable polymer structures because the FSDSC is able to heat and cool at rates up to 10,000 °C/s. FDSC has been used to study mesophase formation and crystallization behavior in numerous polymers including polypropylene,[71] PA 6, [93–95] PA 11,[96] PET,[93,94,97] and silk.[98] The experimental results from FSDSC have been more commonly reported in the research literature in the past two years due to the introduction of the first commercially-available system, the Flash DSC

from Mettler Toledo, which is shown in Figure 2.5. Using a combination of Flash DSC and AFM, the morphology of lamella and mesophase of PA6 at different supercoolings have been resolved.[99] Also, the cold ordering of the PA6 from fast cooling, slow cooling, and isothermal conditions have been studied using the Flash DSC.[100] These studies on PA6 have provided information regarding how the nucleation mechanism can be affected by the temperature and rate of cooling as well as information regarding how the phase (crystal or mesophase) present alters the kinetics of transformation. In a likewise manner, experiments performed on the Flash DSC was used to examine the crystallization behavior of PA11. From these experiments, a bimodal distribution of the crystallization/mesophase formation rate as a function of the temperature was observed, and the authors attributed this behavior to the shift in the crystallization structure from the δ crystalline phase to the δ' mesophase formation, shown in Figure 2.6.[96] The effect of adding 1-butene defects to propylene on its mesophase formation and reorganization upon heating has also been studied using Flash DSC,[71] and Flash DSC has been used characterize the kinetics of mesophase formation within OMMT/PA6 nanocomposites.

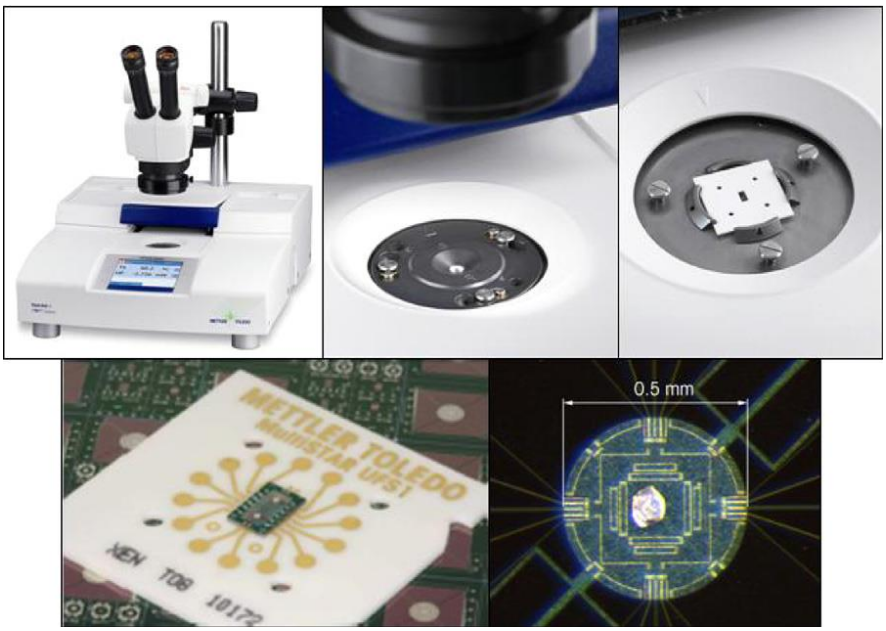

Figure 2.5. The Flash DSC with microscope (top left), mounted sensor (top middle) chip sensor (top right and bottom left) and sample on the target area of chip sensor (bottom right). [93]

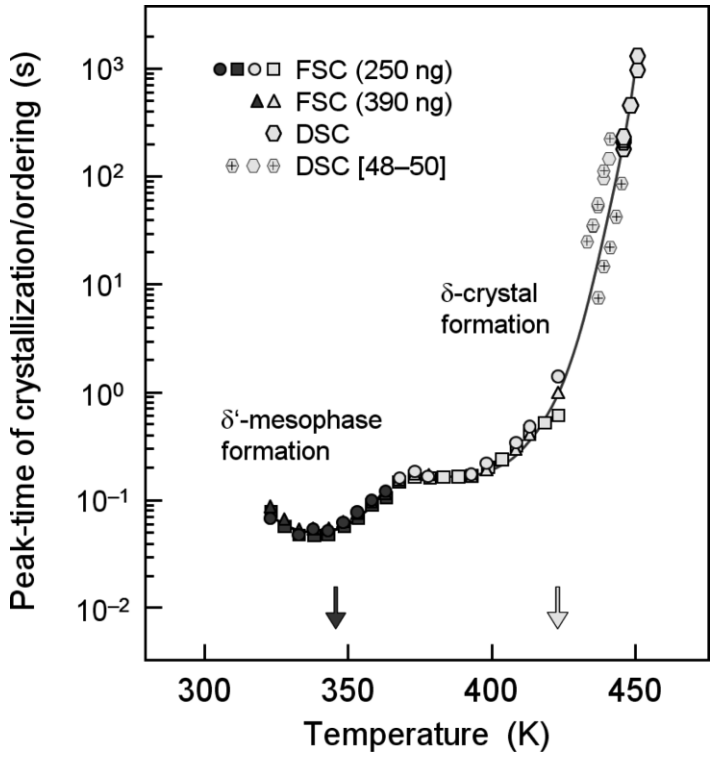

Figure 2.6. Bimodal distribution of the peak time of crystallization/ordering as a function of isothermal crystallization temperature. [96]

2.4 **Cellulose nanocrystals**

Cellulose nanocrystals (CNC) are fibrillar nanoparticles of cellulose. Most CNCs are extracted through an acid hydrolysis process, where the amorphous regions of the cellulose are preferentially attacked leaving behind only the crystalline regions. The size and shape of the extracted CNC will vary based upon the cellulose source because different sources of cellulose contain different amounts of crystallinity and different ratios of the crystal polymorphs (Iα/Iβ).[4,10,101,102] Typically, CNCs extracted from wood will have a length of ~100-200nm and a width of 3-5 nm, whereas CNCs extracted from tunicate are ~500-3000 nm in length and 10-30 nm in width[103]. Figure 2.7shows an image of CNCs that have been extracted from wood.

Figure 2.7. TEM of CNCs extracted from wood.[104]

CNCs generated interest as a reinforcing filler when Favier et al. published results showing that the addition of 6 wt.% CNCs into a latex matrix increased the shear modulus by two orders of magnitude.[105] Since then, CNC have been incorporated into many different polymer matrixes such as PP,[16] polyurethane,[106] and polylactic acid (PLA).[107] In a likewise manner CNCs have been added to many different polymer matrixes such as PLLA,[90] PHB,[63] and PHBV[91,108,109] in order to control the crystallization.

As stated previously, the surface chemistry of a nanocomposite can influence both the dispersion of the nanofiller within the composite as well as the interphase formation; therefore, it is important that the commonly used surface-modification techniques and processing methods be discussed. Figure 2.8 shows some of the common surface modifications of CNCs. Most of the surface modification techniques shown occur during the extraction of the CNCs; however, surface modification via adsorption and covalent attachment of molecules are also other techniques used to create strong interactions between the polymer matrix and the nanofillers. Of the surface functionalization via extraction techniques, sulfuric acid based extraction is one of the most commonly used modification techniques. In this method, the sulfate ester moieties that are formed on the surface of the CNCs create a highly charged surface, stabilizing the dispersion of CNC in polar solvents.[4] Another method of surface functionalization through extraction method that is gaining popularity is the TEMPO-mediated oxidation method. In this method, a 2,2,6,6-tetramethyl-piperidinyl-oxyl (TEMPO) radical is used as a catalyst to oxidize alcohol groups leaving a carboxylic acid surface chemistry.

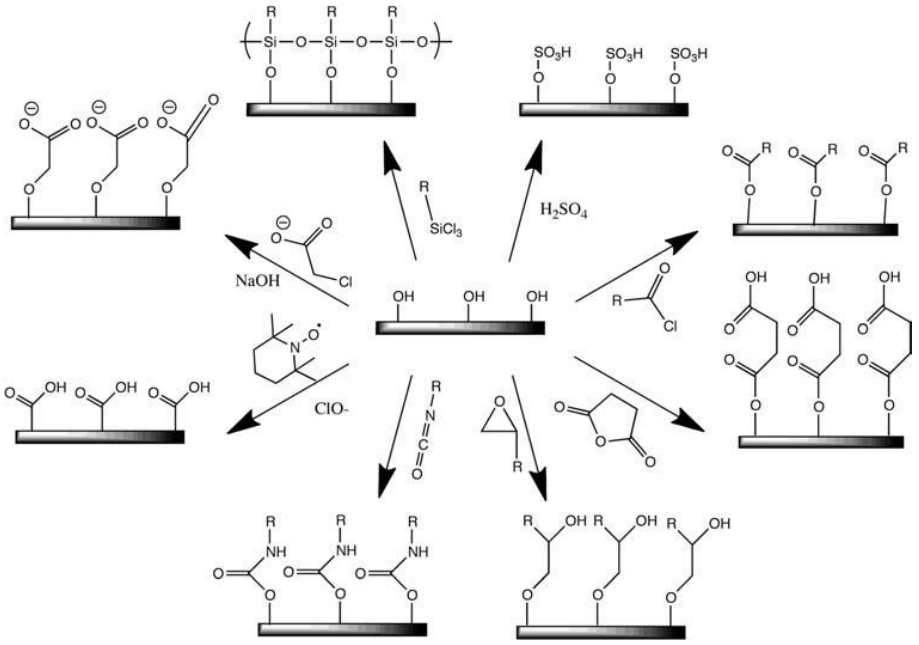

Figure 2.8. Some of the common surface modifications to CNC: sulfuric acid treatment provides sulfate esters, carboxylic acid halides create ester linkages, acid anhydrides create ester linkages, epoxides create ether link, isocyanate create ureathane linkakages, TEMPO mediated oxidation creates carboxylic acids and halogenated acids create carboymethyl surfaces and chlorosilanes create an silylated layer. [4]

Some of the most common methods of processing of CNC-based nanocomposites are casting-evaporation processing and extrusion-based processing. Casting-evaporation processing involves incorporating CNCs in an aqueous solution into a polymer matrix.[103] Typically, an aqueous solution of CNCs is mixed with aqueous polymer solutions, but polymers dissolved in polar solvents have also been used with CNC suspensions.[110,111] Solvent exchange methods need to be used in order to transfer the CNCs from water to organic solvents.[103] For extrusion-based techniques, freeze dried CNCs are often added to a polymer during the mixing process. Aggregation and degradation of the CNCs are some of the common problems that are observed when CNCs are processed using extrusion based techniques.

2.5 **Poly (3-hydroxybutyrate) (PHB)**

PHB is a water-insoluble aliphatic polyester produced by bacteria, and it is used as an energy and carbon reserve. PHB belongs to a larger class of polymers known as polyhydroxyalkanoates (PHAs). The chemical structure of PHB is shown in Figure 2.9. PHB was first isolated and characterized by Maurice Lemoigne in 1926.[112] PHB is amorphous within the bacteria but becomes crystalline once extracted from the cell membrane.[113] There are two molecular conformations for PHB: a 2/1 helix conformation that has an orthorhombic unit cell (α form) and a planar zigzag conformation (β form).[114] In the α form unit cells, the chains are antiparallel with the ester group at the same level[115,116] with the C=O group and the CH_3 oriented outside of the helix.[117,118] The crystalline structure of PHB is shown in Figure 2.10.

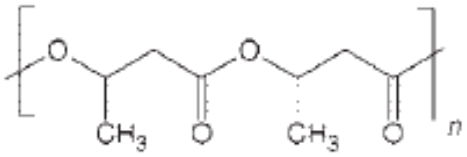

Figure 2.9. Chemical structure of PHB.[119]

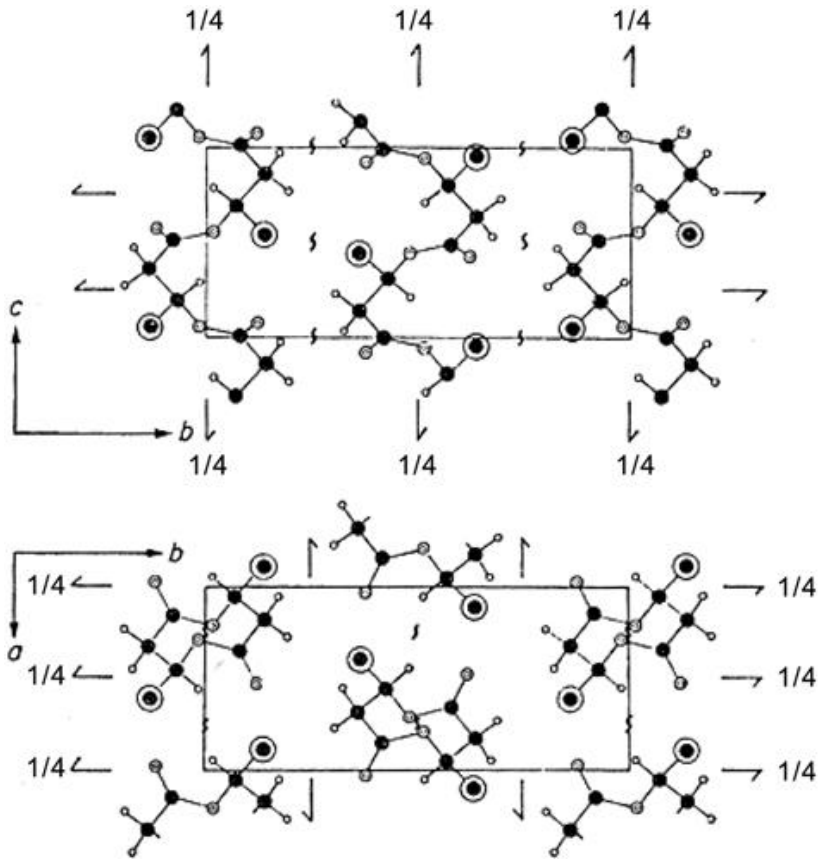

Figure 2.10. Crystalline structure of PHB with O(black), H(unfilled) and CH_3(circle with dot) [120]

2.5.1 Mechanical Properties of PHB

Some of the mechanical properties and the melting temperature of PHB are similar to PP (see Table 2.1),[121] making PHB a potential alternative to PP; however, the elongation to failure of PHB is much lower than that of PP. Therefore, methods of improving the elongation to failure and toughness of PHB are important in the development of a PHB-based material. Methods that have been successful in improving the elongation to failure of PHB include stretching of PHB films,[76,122] blending other polymers with PHB,[60,118,123] and the addition of fillers such as CNCs.[63,118]

Table 2.1. Material Properties of PHB and PP. [124]

Properties	PHB	PP
Melting Temperature (°C)	175	176
Glass Transition Temperature (°C)	15	-10
Density (g/cm^3)	1.25	0.905
Flexural Modulus (GPa)	4	1.7
Tensile Strength (MPa)	40	38
Extension at Break (%)	6	400

2.5.2 Crystallization Behavior of PHB

The crystallization behavior of PHB is well studied and has been described as "an ideal material for nucleation studies"[125] due to the low concentration of impurities (>200 ppm), low nucleation density, and relatively slow crystallization kinetics.[119,125,126] Several methods of nucleation have been observed in PHB: homogenous nucleation, self-

seeding, enhanced self-seeding, and heterogeneous nucleation by impurities.[125] When PHB is homogenously crystallized from the melt, chains of PHB fold into lamellae of 5-10 nm depending on the degree of undercooling[83] and then organize into spherulites. For self-seeding nucleation, when PHB is heated to less than 15 °C above the melting, there is an increase in the nucleation density at low undercoolings (higher temperatures). This results in smaller spherulites. For enhanced self-nucleation, when PHB is heated to less than 1 °C above the melting temperature, spherulites will reappear upon cooling rather than grow from nucleation sites. The self-seeding and enhanced self-seeding nucleation behavior of PHB contributes to the thermal memory often observed in PHB.[127,128] For heterogeneous nucleation of PHB by impurities, the impurities will not have a nucleating effect on the PHB when added in the melt; only after PHB crystallizes around the impurity will the impurity act as a nucleation site.

Since PHB is slow to crystallize, several different nucleating agents have been used in hopes of increasing the crystallization rate. Orotic acid,[119] talc,[129] saccharin,[125] and boron nitrate [129,130] are successful nucleating agents. Jacquel *et al*. suggested that orotic acid, talc, and saccharin were successful nucleating agents because they augment chemical interactions via epitaxial nucleation.[125,131] Barham *el al*. and Jacquel *et al*. suggested that successful nucleation agents had good lattice matching with the (100) plane of the PHB crystal.[125,131]

From the literature, PHB has a RAF that mobilizes at ~70 ˚C,[79] and the RAF plays a role in the cold crystallization during heating of amorphous PHB[85] and for embrittlement of PHB when stored at room temperature.[132]

2.6 **Overview**

In this chapter, the concept of a nanocomposite was introduced, and the interactions responsible for the enhanced properties of nanocomposites were identified and discussed in greater detail. Then, the complex nature of a semicrystalline polymers

and the nucleating effect of nanoparticles were examined. The concepts of a mesophases and the RAF were discussed. In addition to discussing these different concepts, the role of the Flash DSC to characterize mesophase formation as well as different reorganization behavior was reviewed. Using these concepts discussed in this chapter, the design space that is available for PHB with CNC addition will be examined. In particular, how adding CNC into PHB alters the crystallization behavior of PHB will be studied.

CHAPTER 3

EFFECT OF PROCESSING ON MORPHOLOGY

3.1 Introduction

The semicrystalline structure of a polymer is dependent on the thermal history and processing. Therefore, studies have attempted to control the semicrystalline structure of PHB through different thermal treatments, thus preventing the reorganization of PHB when stored at ambient conditions.[132–134] This reorganization of PHB at ambient condition leads to continued crystallization during storage, which usually results in embrittlement of the PHB based material.[132–134] Thermal treatments such as annealing at 70 ˚C have increased the elongation at break of an aged sample to values similar to that of an un-aged sample.[134] Studies have used a self-seeding mechanism[135,136] and the addition of nucleating agents[119,125] as methods for controlling the size of the spherulites formed during the melt processing which may also change the reorganization behavior of PHB. In this chapter, the effect of processing on the semicrystalline structure of PHB will be studied and the ability of CNCs to modify the crystallization behavior of PHB at different steps in a processing operation is evaluated.

The method of processing the nanocomposite can influence not only how the nanofiller is distributed within the matrix but also the component interactions that develop in the system. Solvent processing methods have been shown to promote CNC interactions with one another, leading to the formation of a hydrogen bonded CNC network as the solvent evaporates.[55] When CNC composites are processed by a different method such as melt mixing, the hydrogen bonded network does not always form because polymer chains adsorb onto the surface of the nanofiller, preventing the filler-filler interaction.[55] In this research, four different processing protocols are used to understand their effect(s) on the on the structure of the nanocomposite. Two solvent-casting methods

(SC), one anti-solvent processing method (AS), and one anti-solvent compression molding (ASCM) method are the different methods that will be used. The anti-solvent processing technique used in this research is based upon the solvent extraction method commonly used to extract PHB from bacterial cells, where a non-solvent is used to precipitate PHB molecule.[113,131,137] This anti-solvent processing technique is commonly used to encapsulate pharmaceutical drugs with drug delivery proteins[138] as well as a novel method of encapsulating nanoparticles within particles.[139–142]

3.2 **Experimental**

3.2.1 Materials

The components of the nanocomposite systems studied in this work were obtained from outside sources. The CNCs were provided by the USDA Forest Service, Forest Products Laboratory (Madison, WI). The CNCs were received in aqueous suspension with a solids loading of 6.5 wt.% . The matrix polymer, PHB, was of natural origin and purchased from Sigma-Aldrich. The as-received PHB was an off-white powder, and the weight average molecular weight of the polymer was 426,000 g/mol. Prior to use, the PHB polymer was purified by using a solvent extraction method described in the literature [138,143] where the PHB powder was dissolved into warm chloroform (55 ˚C), and the warm chloroform/PHB solution was then precipitated in cold methanol (10 ˚C). The powder was dried in a vacuum oven for 48 hours at room temperature.

3.2.2 Processing Methods

Four different processing strategies were used to produce the CNC/PHB composites. They are shown schematically in Figure 3.1.

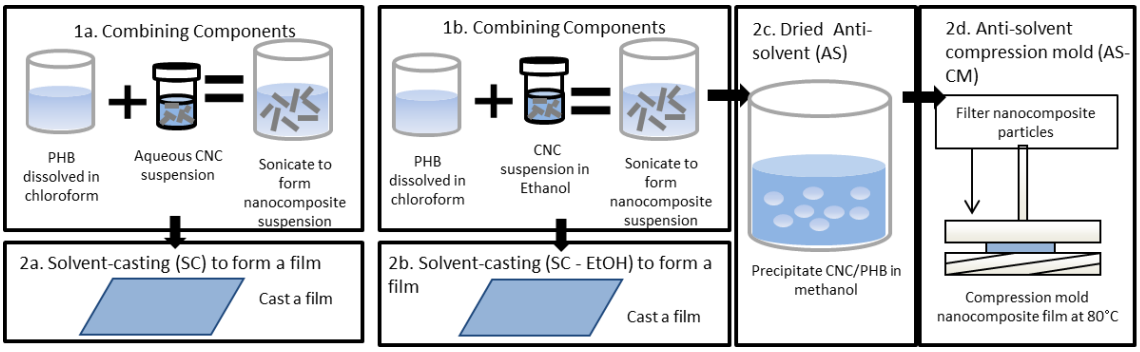

Figure 3.1. Schematic of the four different processing methods used.

The two solvent casting methods used differed in the solvent used to dilute the as-received CNC suspension. When water was used to dilute the CNC suspension, the method was denoted as SC-H_2O, and this method is shown as steps 1a and 2a. In this method, the as-received CNC suspension was diluted with water to a solids loading of 1.0 wt. % CNC. This diluted CNC suspension was mixed with a PHB/chloroform solution at 10 wt. % PHB. The CNC/PHB suspension was sonicated using a cup horn sonicator at 87 mW in a water bath at 55˚C at 45 minutes and then cast into a film by pouring the suspension into a PTFE evaporating dish. The solvent was allowed to evaporate in a fume hood at room temperature for 48 hours. For samples produced by the other solvent casting method, denoted SC-EtOH and shown as steps 1b and 2b, the as-received CNC suspension was diluted with ethanol to a concentration 1.0 wt. % instead of water. Then the composite samples were processed similarly to those made by the SC-H_2O method described above.

For the anti-solvent precipitation method (AS), the processing method began with the solution preparation and sonication steps of the SC-EtOH method. Then, the CNC/PHB solution was poured into 500 mL of cold methanol (10 ˚C) and stirred at 750 rpm for 120 minutes. A precipitate formed when the CNC/PHB solution was added to the methanol, and this precipitate was filtered and then dried in a vacuum oven at room temperature for 24 hours to form the sample.

For the anti-solvent compression molding method (ASCM), the anti-solvent precipitate was processed further. The anti-solvent precipitate was placed in a mold and then compressed at 2 metric tons and held at 180 ˚C for 2 minutes before being water cooled to room temperature.

3.2.3 Differential Scanning Calorimetry (DSC)

3.2.3.1 Thermal sweep

The thermal transitions of the neat PHB and CNC/PHB composites were obtained using a TA Q200 differential scanning calorimeter (DSC). The mass of the DSC samples tested was approximately 10 mg. Neat and composite materials produced by each process were tested by this method. Results obtained from three separate samples for each material were averaged to obtain the data presented.

The melting temperature (T_m), crystallization temperature (T_c) and % crystallinity of the samples were obtained from thermal sweep scans. In these thermal sweep experiments, the samples were heated from room temperature to 193 °C at a rate of 10 °C/min. Because of the thermal memory of PHB[125] and the thermal degradation of PHB at temperatures above 170 °C,[137] the maximum temperature and hold time used were chosen so that the sample fully melted and polymer degradation was minimized.[144] Therefore, the samples were held at 193 °C for 3 minutes, cooled to -40 °C at a rate of 10 °C/min, held at -40 °C for 3 minutes, and the heat/cool cycle was repeated.

The % crystallinity of each sample was calculated using the equation below:

$$X_c(\%) = \frac{\Delta H_m (m_c / m_p)}{\Delta H_0} \times 100 \quad (1)$$

Where ΔH_m is the experimentally-obtained enthalpy of melting, and ΔH_0 is the theoretical enthalpy of melting for a 100% crystalline PHB sample which is 146 J/g.[125] m_c is the nanocomposite weight and m_p is the weight of PHB in the nanocomposite.

3.2.3.2 Isothermal Crystallization

Isothermal crystallization experiments were performed by heating samples from 25 °C to 193 °C at a rate of 10 °C/min. The samples were held at 193 °C for 3 minutes and then cooled to the desired isothermal crystallization temperature at a rate of 100 °C/min. The samples were then held at the desired isothermal crystallization temperature for 20-60 minutes, and then the sample was cooled to -40 °C at a rate of 10 °C /min. The samples was held at -40 °C for 3 minutes and heated at a rate of 10 °C /min to 193 °C.

3.2.4 Optical Microscopy

Additional isothermal crystallization experiments were performed on the SC-EtOH, SC-H_2O and ASCM samples at 110 °C using an Olympus B51X microscope and a Linkam LTS420 hot stage attachment. In these isothermal experiments, the samples were heated to 193 °C at a rate of 30 °C/min and then held at 193 °C for 3 minutes before cooling to 110 °C at a rate of 30 °C/min. The samples were held at 110 °C for 15 minutes. Images were taken at 30 s intervals upon cooling and during the isothermal hold time. These images were used to obtain the average spherulite size.

3.2.5 FT-IR

Fourier transform infrared (FT-IR) spectroscopy measurements were performed with a Bruker Hyperion with ATR 20X attachment. The spectra were recorded at room temperature in the range of 4000 to 400 cm^{-1} using 32scans and a resolution of 4 cm^{-1} in transmission mode.

3.3 **Results and Discussion**

3.3.1 Effect of adding CNCs

Figure 3.2 shows the crystallization peak upon cooling and the melting peak behavior for the SC-EtOH processed samples with different CNC loadings. In Figure 3.2a, the differences in the crystallization behavior during cooling can be clearly seen for the SC-EtOH samples. The crystallization peak of the sample with 0.5 wt.% CNC and 1.0 wt. % CNC both occurred at a higher temperature than the neat PHB sample. Also, the magnitude of the crystallization peaks for the samples with CNCs was significantly greater than the magnitude of the crystallization peak of the neat PHB sample, and the width of the crystallization peak for the samples with the CNCs was less than the width of the crystallization peak of the neat PHB samples. The increase in the magnitude of the peak suggested than the nucleation rate was greater for the samples with CNC than that of the neat PHB, and the narrower crystallization peak in the composite samples suggested that the crystallite size distribution of the samples with CNCs was smaller than the size distribution of the neat PHB samples.[145] In Figure 3.2.b, the second heating cycle data for the SC-EtOH samples are shown. The neat PHB sample exhibited melting-recrystallization-remelting (MRR) behavior, but MRR was not observed in the samples with CNCs. This MRR behavior has been observed in neat PHB,[145,146] HAp/PHB nanocomposites, [147] CNC/PHV composites, [109] and PET.[148] The presence of MRR behavior in the neat PHB sample could be attributed to the larger supercooling (T_m-T_c) of neat PHB compared to the CNC/PHB samples or the CNCs acting as nucleating agents. A larger supercooling results in the formation of less perfect crystals or thinner lamellae, which have a lower melting point. During heating at relatively slow rates, the thin lamellae can melt and recrystallize into thicker lamellae, which have a higher melting point. Additionally, the nucleating effect provided by the CNCs could promote the

formation of more stable crystals which would also produce a single melting peak at a temperature similar to the remelting peak of the neat PHB.

Figure 3.4 shows how the peak value of T_c and the % crystallinity changed with CNC loading for the four different processing methods. From the literature, neat PHB has a crystallization peak occurring at approximately 81 °C for a cooling rate of 10 °C/min,[149] which was consistent with the results presented here for all of the processing methods except ASCM. The value of T_c increased as more steps were added to the processing protocol, but the increase in T_c from SC-EtOH to AS was within the error and not considered significant. However, the increase in the value of T_c from the AS to the ASCM processing method was 18 °C. For all processing methods, the addition of 0.5 wt. % of CNC also significantly increased the value of T_c to temperatures ranging from 105-110 °C. The addition of 1.0 wt., % of CNC further increased the T_c for all processing methods, though for the SC-H_2O processing method, a small decrease relative to the 0.5 wt.% sample was observed. These results suggested that CNC acted as a nucleating agent for PHB by reducing the energy needed for crystallization to occur upon cooling. These results were consistent with computational results from molecular dynamic simulations which suggested that for alkanes the adsorption of the polymer chains onto the surface of a nanoparticle can enhance the nucleation process.[32] This increase in the T_c has also been experimentally observed for known nucleating agents of PHB such as boron nitride [129,130,135] and saccharin.[125,135] The magnitude of the increase in the T_c for 0.5 wt. % CNC/PHB was less than that the increase in the T_c seen for a 0.2 wt. % addition of boron nitride, which was a 35 ˚C increase in the T_c upon cooling.[130] The magnitude of the increase in the T_c with 0.5 wt.% CNC addition was comparable to the magnitude of the increase in the T_c with addition of the 1.0 wt % saccharin.[135] It is worth mentioning that processing methods used in the papers discussed vary from the experiments performed here. In a likewise manner, the cooling rates of the experiment performed from the

literature examples are greater than the rate used in this work. Therefore, the differences in the T_c increases for CNCs, boron nitride, and saccharin may be attributed to experimental protocols as well as differences inherent to the nucleating agents.

Additionally, the addition of CNCs to PHB increased the bulk crystallinity of the samples for all processing methods at a loading of 0.5 wt. % CNC; however at a loading of 1.0 wt. % CNC, there was no significant change in % crystallinity for all of the samples. Table 3.4 summarizes some of the differences in the crystallization peak upon cooling for the solvent cast samples. For the SC-EtOH samples, the onset of crystallization increased as CNCs were added. The slope of the exothermic peak has been associated with the nucleation rate upon cooling where increased slope was associated with increased nucleation rate.[91] From the table, the addition of nanoparticles increased the slope upon cooling for both SC processing methods. Additionally, the slope values were greater for the SC-EtOH composite samples than those for the SC-H_2O composite samples. In a likewise manner, the onset temperature and the area of the crystallization peak for the SC-EtOH 0.5 wt. % CNC/PHB sample were greater than that of either of the CNC loaded SC-H_2O samples. These results indicated that the processing method affected the nanoparticles nucleating ability. These results were most likely because of the interactions that occurred between the ethanol and the PHB. Ethanol has been used during the extraction process either as a stabilizer for the PHB/chloroform solution in small amounts (less than 1 % v/v)[150] or as the as the non-solvent for the precipitation of PHB when used in large amounts.[151] Therefore during the solvent casting process, the addition of the CNC/ethanol suspension into the PHB/chloroform solution could have induced precipitation of the PHB around the CNCs. This precipitation of the PHB around the PHB would result in enhanced nucleation such as the nucleation by impurities observed by Barham,[125] where the nucleating effect of the impurity was observed only after melting and recrystallization. A similar result was not seen in the neat PHB samples.

Both neat PHB samples processed by SC methods had approximately the same slope, though different onset temperature values.

Significant MRR behavior was observed in the SC-H_2O samples, as shown in Figure 3.3. This multiple melting peak behavior was different than the melting peak behavior observed for the SC-EtOH samples (Figure 3.2.b). For the SC-H_2O samples, the addition of CNCs increased the magnitude of the lower temperature melting peak, whereas for the SC-EtOH sample only a single melting peak was observed for the CNC/PHB samples. The difference in the melting behaviors could be due to the differences in the component interactions during processing. This MRR behavior has been observed in PHB [108,147] blends including PHB blended with cellulose acetate butyrate (CAB).[123] Intramolecular hydrogen bonds between the C=O group of PHB and the O-H group of CAB create physical cross links between PHB and CAB, which reduce the polymer chain mobility and intermolecular hydrogen bonding needed to form the crystalline form of PHB.[60,118,152]

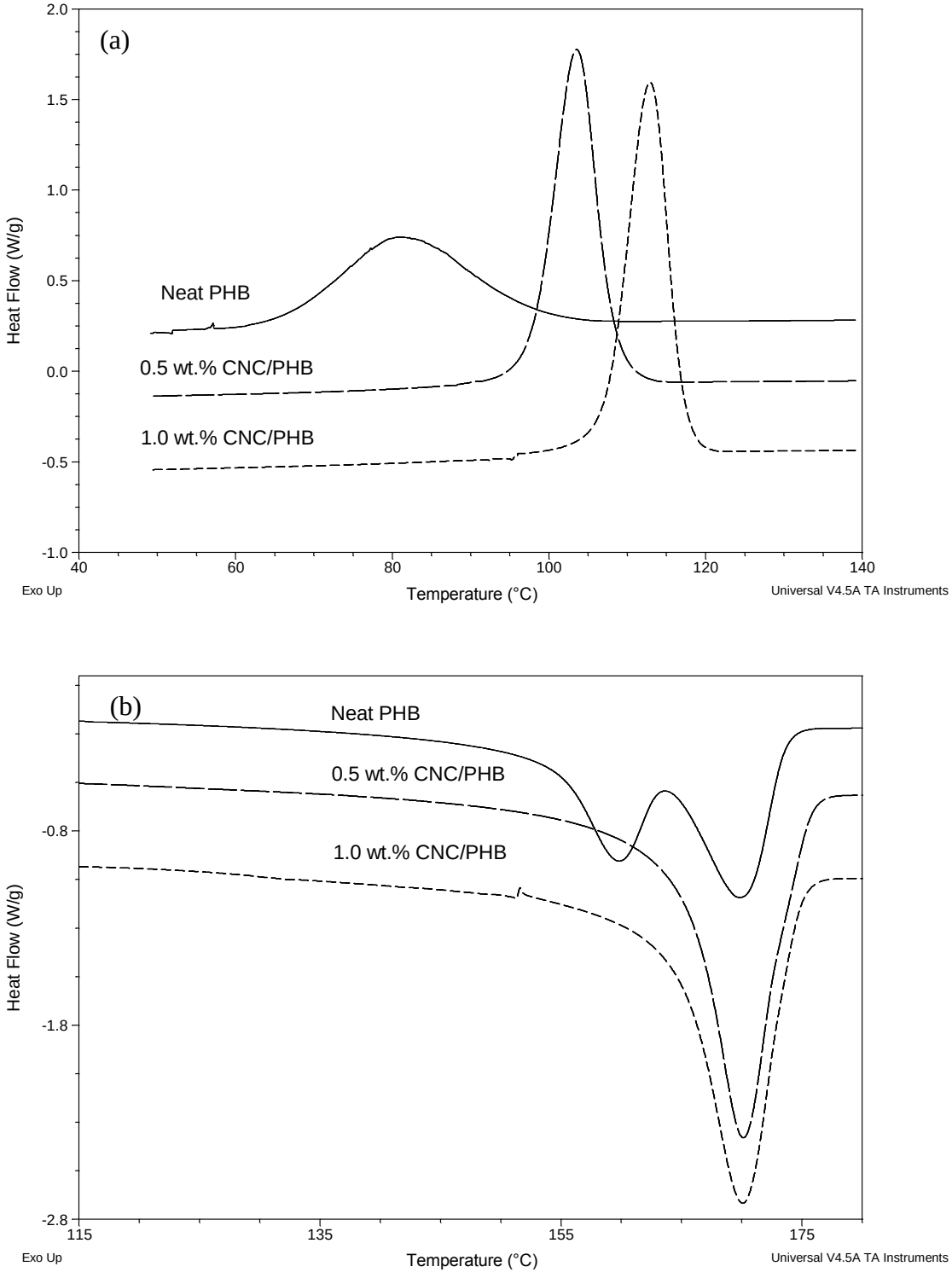

Figure 3.2.a) Crystallization peak upon cooling for the SC-EtOH samples with different CNC loadings. b) Melting peak behavior of SC-EtOH samples with different CNC loadings.

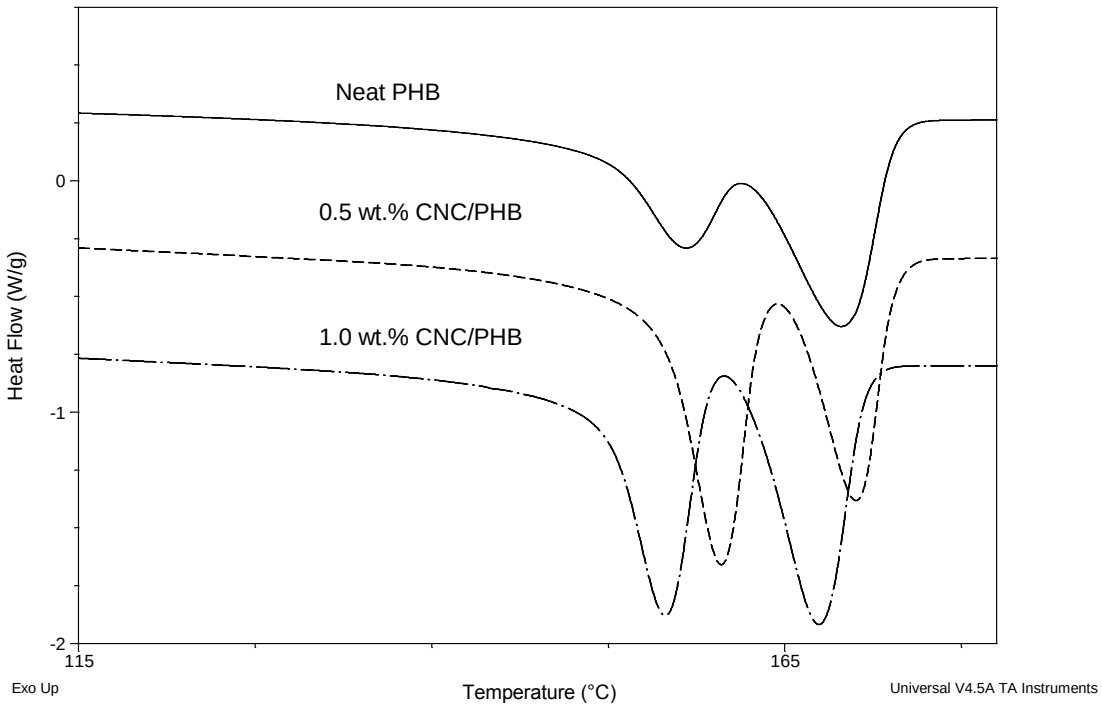

Figure 3.3. Second heating DSC curves for SC-H_2O samples with different CNC loadings.

Table 3.1. Summary of the parameters of the crystallization peak upon cooling for the solvent cast samples processed with ethanol and water.

	SC-EtOH					**SC-H_2O**			
	Onset (°C)	Width (°C)	Area (J/g)	Slope W/(g·°C)		Onset (°C)	Width (°C)	Area (J/g)	Slope W/(g·°C)
Neat PHB	98.0 ±0.6	21.0 ±2.8	58.8 ±2.5	-0.03 ±0.00	**Neat PHB**	87.0 ±6.4	18.9 ±0.8	51.0 ±3.3	-0.03 ±0.01
0.5 wt. % CNC/PHB	108.3 ±0.8	6.1 ±0.5	77.8 ±2.1	-0.44 ±0.01	**0.5 wt. % CNC/PHB**	99.9 ±1.8	8.0 ±3.3	72.6 ±1.0	-0.20 ±0.01
1.0 wt. % CNC/PHB	116.3 ±1.2	6.0 ±0.5	82.0 ±1.3	-0.53 ±0.02	**1.0 wt.% CNC/PHB**	98.1 ±0.9	6.7 ±0.1	67.7 ±0.2	-0.29 ±0.02

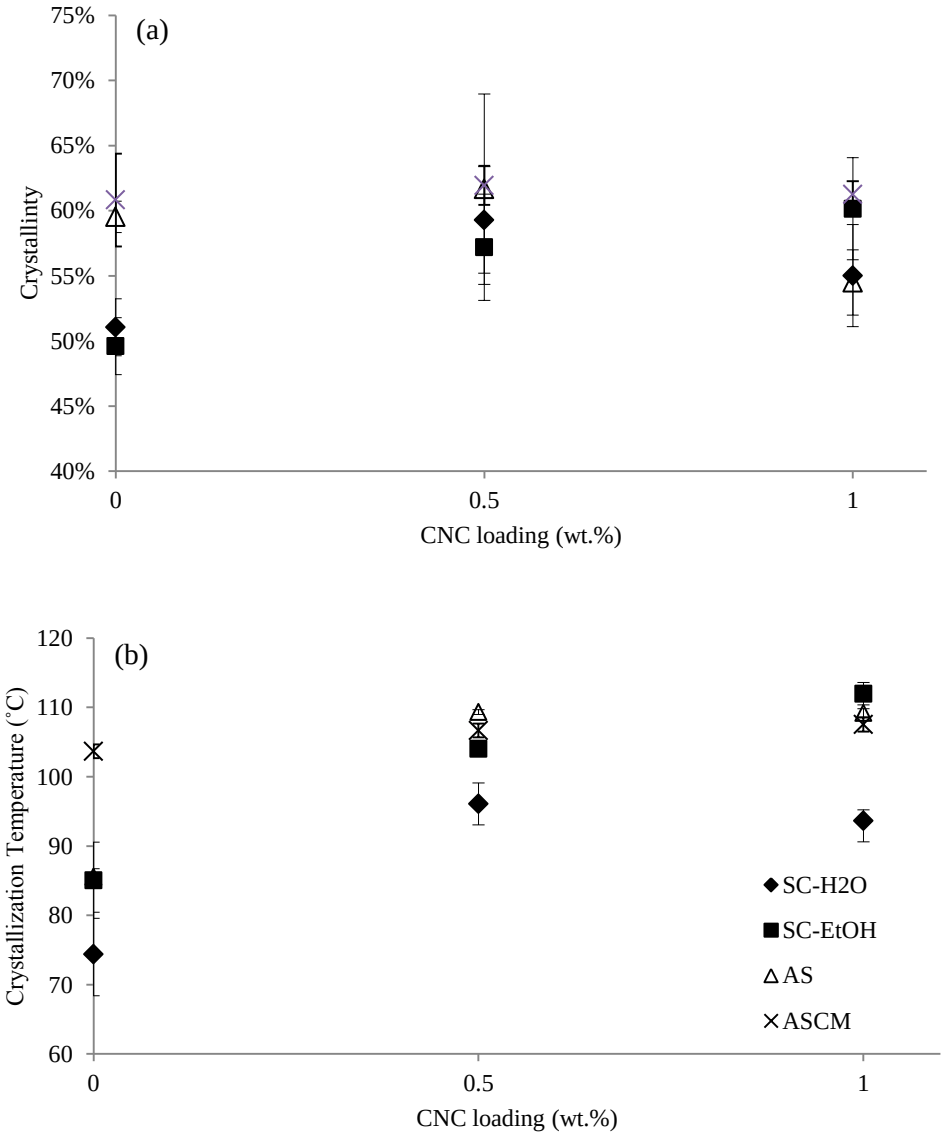

Figure 3.4. Summary of the results obtained from thermal sweep experiments. (a) Crystallinty plotted as a function of CNC loading. (b) Crystallization temperature plotted as a function of CNC loading.

3.3.2 Effect of processing on thermal behavior

The effect of processing method on the bulk crystallinity and thermal transitions can be observed most easily in the neat PHB samples (see Figure 3.4). There was a significant difference in the crystallinity between the SC samples and the AS samples. The SC method produced a film whose crystal structure developed when the solvent was evaporated at a slow rate whereas the AS method produced particles, whose morphology was controlled by the precipitation conditions.[153] From DSC data, the neat solvent cast samples had bulk crystallinity values of 51.2 ± 2.2 and 49.6 ± 1.5 for the SC-EtOH and SC-H_2O samples, respectively. Neat PHB samples produced by solvent casting methods typically have a bulk crystallinity ranging from 40-60% depending on the time left at room temperature to allow for the crystallization.[62,130,154] In contrast, the AS and ASCM neat PHB samples had crystallinity values of 59.5 ± 1.2 and 60.8 ± 3.6, respectively. The differences between the values of T_c of the neat PHB samples processed differently also provided information regarding differences in the crystallization behavior. The neat PHB samples processed by the SC-EtOH method had a T_c value similar to that of samples produced by the AS method. The SC-H_2O sample had the lowest T_c and the ASCM had the greatest T_c. These results could be a result of the polymer-solvent interactions that occurred during processing. For the SC samples, the differences in the component interactions were not only seen in the neat PHB samples but also in the composite samples. These differences in the crystallinity and T_c between the samples processed with water and ethanol could be due their miscibility with chloroform. Since water and chloroform are not miscible whereas chloroform and ethanol are, the interactions between the CNCs and the PHB could be different. In addition, the presence of water has been shown to change the crystallization behavior of PHB. Water can form hydrogen bonds with the carbonyl group of the backbone of PHB,[155] interfering with the hydrogen bonding that occurs between the C=O and CH_3 groups during crystallization from the

melt.[156,157] Therefore, the immobilization of the carbonyl backbone of PHB could be an explanation for why the T_c of the SC-H_2O sample was significantly lower than that of any other processing method. For the SC-H_2O samples, the interaction between the CNCs suspended in water and the PHB would be minimal due to the incompatibility between water and chloroform. For the ASCM neat PHB, the higher T_c could be due to processing at higher temperatures. The exposure to higher temperature could produce more stable nuclei and enhance the nucleation behavior upon cooling, very similar to the self-seeding behavior and thermal memory of PHB described in the literature. The self-seeding behavior appeared when a sample was heated to less than 15 °C above its melting temperature.[125] For the ASCM sample, the end of melting occurred at approximately 180 °C, only 13 °C less than the highest temperature used in these DSC experiments.

3.3.3 Isothermal Crystallization

In order to quantify the changes in the kinetics of crystallization, different models can be fit to the experimental data. The power law model, Avrami equation, and n-d diffusion based models are some of the kinetic models used to describe solid state kinetics.[158] Since the Avrami equation is a well-used model used to describe the isothermal crystallization kinetics of polymer crystallization and shows good agreement with experimental results in the literature,[159] the Avrami equation will be used to characterize the kinetics of isothermal crystallization in this work. Studies of PHB-based nanocomposites have reported an increase in the rate constant while the Avrami constant remained constant with the addition of nanofillers in PHB,[62,147,160] which suggested that the mechanism of crystallization did not change with the addition of nanofiller but rather that the nucleation density was increased.[160] This crystallization behavior was similar to the self-seeding phenomenon which has been observed in PHB.[125,135]

The linearized formed of the Avrami equation used to calculated the Avrami constant n and the kinetic constant k_t is shown below

$$\ln\{-\ln[1-\alpha]\} = \ln k_t + n \ln t \quad \textbf{(1)}$$

Where α is the extent of transformation. Figure 3.5 describes how the heat flow vs. time data are used to calculate α and *n* and k_t values for a sample. The *n* values provide information regarding the type of nucleation and also the dimensionality of the crystal growth, and the k_t values provide information regarding the kinetics of crystal growth and nucleation. In Figure 3.5.a, the heat flow is plotted as a function of time such that the exothermic peak associated with crystallization at the isothermal temperature is seen. Often times, the proper baseline must be established before the heat flow as a function of time data can be used in the calculation of the fraction transformed. There are many different methods of choosing a baseline, and if a baseline is chosen incorrectly, substantial errors can be generated.[161] In this work, a linear baseline was used by fitting a line between the point at the local minima of the heat flow signal at the start of the isothermal hold and a point at the local minima at the end of the isothermal hold. In order to obtain the fraction transformed as a function of time (shown in Figure 3.5.b), the following equation was used:

$$\alpha(t) = \frac{\Delta H(t)}{\Delta H_{total}} \quad \textbf{(2)}$$

Where the extent of transformation at time t ($\alpha(t)$) is equal to the change in the enthalpy from beginning of crystallization to time t ($\Delta H(t)$) divided by the total change in enthalpy for the crystallization peak. In Figure 3.5.c, the linear portion of the extent of transformation as a function of time (α = 5%-40%) was fit to the linearized form of the Avrami equation (Equation 1) since the equation described the crystallization kinetics until spherulite impingement. In Table 3.2, the results of Avrami analysis are shown for the neat PHB, 0.5 wt. % CNC/PHB and 1.0 wt. % CNC/PHB samples from the four

different processing methods. All of these data were collected at an isothermal crystallization temperature of 120 °C. A modified JMA analysis of the isothermal crystallization experiments performed for all processing methods at an isothermal crystallization temperature of 120 °C is shown in the Appendix as Table A.3 . For this modified JMA analysis, $\alpha(t)$ is replaced with the extent of crystallization($\Phi(t)$). This substitution is used in order to account for the fact that extent of transformation does not directly correspond to the amount of crystallization that occurs. In this Table 3.2, data for the neat PHB processed by the SC-H_2O method were not included since at this temperature the crystallization peak was difficult to distinguish from the baseline. In a likewise manner, the crystallization peak of the AS was also difficult to isolate from the baseline, and the crystallization half time was 30.7 minutes, with an induction time of approximately 15.9 minutes. This long induction time altered the calculation of k_t for this sample, and most likely led to the increased value of *n*. The values of *n* for the neat PHB processed by the SC-EtOH and ASCM methods were within the range of the values reported in the literature, which ranged from 2.5-2.8 for solvent cast neat PHB crystallized isothermally at 120 °C.[62,130] The values of *n* remained within this range of 2.5-2.8 for most of the samples studied here. The similarity in the results for *n* suggested that neither the dimension of crystal growth nor the nucleation mechanism changed greatly with processing (except the AS) or with nanoparticle addition (except the 1 wt. % CNC/PHB processed by SC-H_2O).

The k_t *values* for all of the samples were increased with the addition of 0.5 wt. % CNCs, and the *k* values continued to increase as the CNC loading was increased from 0.5 wt. % to 1.0 wt. % for all of the processing methods except for SC-EtOH. These results indicated that in general the addition of nanoparticles increased the rate of primary crystallization. This increase in the crystallization rate could be due to the nucleating effect of CNCs as suggested by the thermal scan experiments. An increase in the number

of nucleating sites would increase the overall rate of crystallization without changing the dimension of crystal growth.

Table 3.3 shows how the n, k_t, and $t^{0.5}$ of the samples processed by the SC-EtOH methods changed as a function of isothermal crystallization temperature. From this table, the n values generally increased as the isothermal crystallization temperature increased. This increase in the n values with increasing isothermal crystallization temperature has been observed in the literature.[162] These results suggested that the dimensionality of crystal growth was reduced as the isothermal crystallization temperature was reduced. Conversely, the k_t value decreased as the isothermal crystallization temperature increased. These results were expected because in this temperature range, the kinetics of crystallization for PHB was within the nucleation-limited regime. Therefore as the temperature was increased, the kinetics of crystallization were expected to slow down as stable nuclei were more difficult to form at higher temperatures. This trend was also seen by the increase in the value of $t^{0.5}$ as the isothermal crystallization temperature was increased. Similar behavior was observed in the samples produced by the SC-H_2O method, and these data are shown in the Appendix as Table A.2.

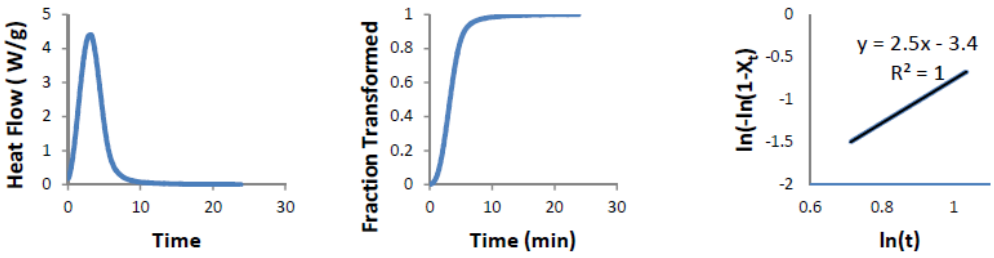

Figure 3.5. Schematic of how isothermal crystallization data are used to calculate the fraction transformed.

Table 3.2. Avrami analysis of the isothermal crystallization experiments at 120 ˚C.

		SC-EtOH	SC-H_2O	AS	ASCM
Neat PHB	n	2.6		3.4	2.7
	k	0.0044		0.0000	0.013
	$t^{0.5}$ (min)	7.4		30.7	4.4
0.5 wt. % CNC/PHB	N	2.5	2.6	2.8	2.8
	k	0.0101	0.0015	0.0696	0.0200
	$t^{0.5}$ (min)	5.4	10.8	2.3	3.6
1.0 wt. % CNC/PHB	n	2.7	2.3	2.7	2.7
	K	0.0074	0.0063	0.0887	0.0312
	$t^{0.5}$ (min)	5.3	7.7	2.2	3.2

Table 3.3. Avrami analysis of samples produced by the SC-EtOH method.

Isothermal Crystallization temperature (˚C)		**110**	**115**	**120**	**125**
Neat PHB	n	2.0	2.1	2.6	
	k	0.248	0.063	0.004	
	$t^{0.5}$ (min)	1.7	3.1	7.4	
0.5 wt. % CNC/PHB	n	1.8	2.2	2.5	2.4
	k	0.425	0.214	0.010	0.006
	$t^{0.5}$ (min)	1.3	1.7	5.4	7.0
1.0 wt. % CNC/PHB	n	2.3	2.1	2.7	2.7
	k	0.155	0.098	0.007	0.000
	$t^{0.5}$ (min)	1.9	2.6	5.3	14.4

3.3.4 Activation Energy calculations

To calculate the effective activation energy, the average k_t values were obtained from three measurements at each isothermal crystallization temperature ranging from 110 to 120 °C for the SC-EtOH samples. The classical temperature dependence of k_t on the isothermal crystallization temperature is described in the equation below

$$k_{ti} = k_{t0} \exp\left[\frac{-E_a}{RT_C}\right] \quad (3)$$

where k_{to} is a temperature independent preexponentional factor, R is the ideal gas constant, and T_c is the isothermal crystallization temperature. Using the linearized form of equation 3, a linear regression of the *lnk* values plotted as a function of inverse isothermal crystallization temperature ($1/T_c$) can be used to calculation the activation energy for a sample (shown in Figure 3.6). The activation energy values (E_a) were calculated for the SC-EtOH samples. The calculated activation energy for neat PHB was -102.9 kJ/mol. The activation energies calculated for 0.5 wt.% CNC/PHB and the 1.0 wt.% CNC/PHB were -230.8 kJ/mol and -317.9 kJ/mol, respectively. These results were consistent with what would be expected if the nanoparticles acted as nucleating agents; as more nanofiller was added, the energy needed for crystallization to occur was reduced. These results were also close to the values obtained from the literature, which were approximately -135 kJ/mol for the neat solvent cast PHB.[62] The activation energies of the SC-H_2O sample, AS and ASCM samples were not calculated due to large deviations in both the n and *lnk* values.

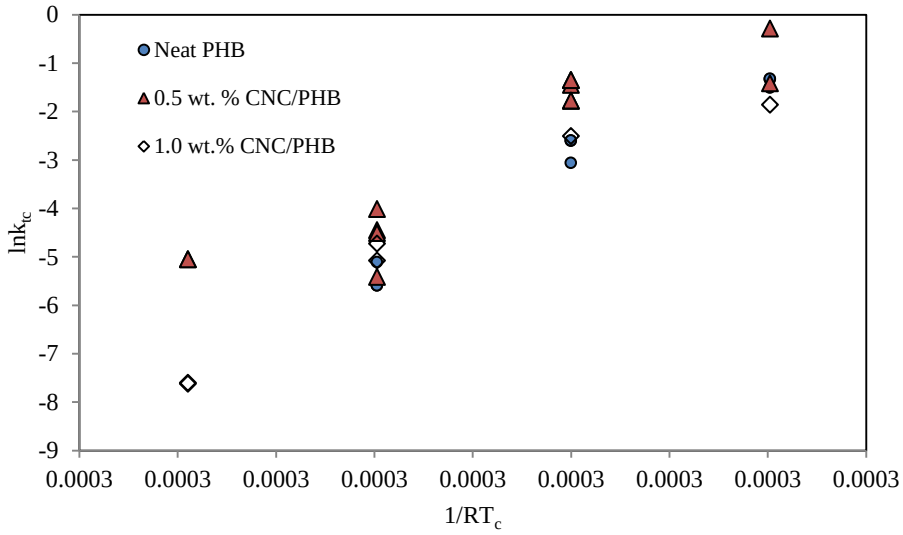

Figure 3.6. Plot of the $\ln_k t$ plotted as a function of the isothermal crystallization temperature.

3.3.5 Optical Microscopy

Imaging with optical microscopy was used to show differences in the morphology of the ASCM and SC-EtOH samples. Surface images were taken to show differences in the as-processed morphology, and hot stage microscopy experiments were performed to observe differences in the crystallization behavior and crystalline morphology of the samples after processing.

3.3.5.1 Surface Images

Optical micrographs of the SC-EtOH samples and the ASCM samples were taken under polarized light. The surface images of the ASCM are shown in Figure 3.7. The images for the SC-EtOH are included in Appendix A as Figure A.1. From these images, differences in the surface morphology between SC-EtOH samples and the ASCM samples were seen. For the SC-EtOH samples, the surface roughness of the surface prevented the spherulites from being observed in the optical micrographs. However, spherulites were observed on the surface of all of the ASCM samples. These results were due to the compression molding step of the ASCM processed samples. These samples had a smoother surface than those produced by casting, leading to a clearer visualization of the crystal structure. Based on the thermal sweep DSC data, the lack of spherulites observed in the SC-EtOH samples did not indicate that the samples were amorphous.

Differences between the neat PHB and CNC loaded samples produced by the ASCM method were observed (see Figure 3.7.). The size of the spherulites in the neat PHB samples were larger those in the CNC loaded samples. Also as the CNC loading was increased from 0.5 wt. % to 1.0 wt. %, the spherulites within the sample appeared smaller and more uniform, consistent with the results from previous experiments in this Chapter suggesting that the CNCs promote nucleation.

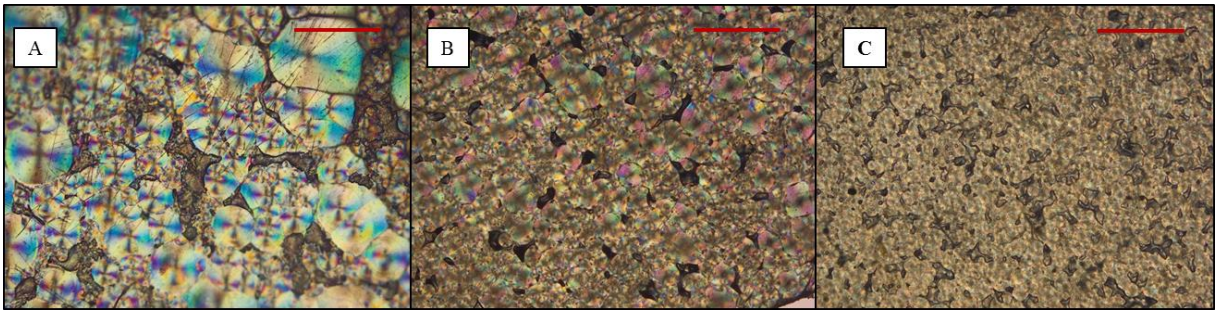

Figure 3.7. Optical micrographs of the ASCM samples: neat PHB (DA), 0.5 wt.% CNC/PHB (B), and 1.0 wt.% CNC/PHB (C) Scale bar=100µm.

3.3.5.2 Hot stage Microscopy

The difference in the morphology of the SC-EtOH samples is shown in Figure 3.8. For the SC-EtOH samples, the average spherulite radius for the neat PHB sample was 174.8 ± 30.6 µm while the 0.5 wt. % CNC/PHB sample had an average spherulite size of 62.4 ± 16.3µm, and the 1.0 wt. % CNC/PHB had an average spherulite size of 49.9 ± 19.1 µm. A one-tailed heteroscedastic t-test was performed to compare the population of the observed spherulite radii of the neat PHB sample to the population of observed spherulite radii of the 0.5 wt. % CNC/PHB sample. The null hypothesis for the one -tailed t-test was that observed spherulite radii from the different samples were sampled from the same population of spherulites. The likelihood of the observed spherulites sizes of the neat PHB and the 0.5 wt. % CNC/PHB sample falling within the same population was much less than 1%; therefore, these results indicated that the observed spherulite size population of the neat PHB was distinctly different from the observed spherulite size of the 0.5 wt. % CNC/PHB. In a likewise manner, a one-tailed t-test was performed to compare the spherulite population of the 1.0 wt. % CNC/PHB sample with the spherulite population of the 0.5 wt. % CNC/PHB sample. There was 99.9 % probability that the spherulite population of the 1.0 wt. % CNC/PHB was distinctly

different for that of the 0.5 wt. % CNC/PHB sample. These results further indicated that as more CNCs (suspended in ethanol) were added into the PHB, the CNCs had a nucleating effect on the PHB because of the smaller spherulite size with increased CNC loading. Also these results suggested that the dispersion of the CNCs was relatively good because as the CNC loading was increased, there was a statistically significant difference in the spherulite size.

The SC-H_2O samples exhibited a similar trend with CNC loading. The average spherulite size of the neat PHB sample was 160.6 ± 11.4μm. The average spherulite size observed for the 0.5 wt. % CNC/PHB sample was 74.0 ± 20.2μm, and the average spherulite size observed for the 1.0 wt. % CNC/PHB sample was 64.6 ± 24.5μm. A one-tailed t-test was performed to compare the population of the observed spherulite radii of the neat PHB sample with the observed spherulite radii of the 0.5 wt. % CNC/PHB sample. The results from the one-tailed t-test indicated that the population of spherulites within the neat PHB sample was distinctly different from the population of the spherulites within the 0.5 wt. % CNC/PHB sample. These results suggested that adding CNCs suspended in water into PHB decreased the size of the spherulites formed during isothermal crystallization. This decrease in the size the spherulites can be attributed to the increase in the nucleation density at 110 ˚C. In a likewise manner, when a one-tailed t-test was performed to determine if the observed spherulite radii of the 1.0 wt. % CNC/PHB sample were distinctly different from the observed spherulite radii of the 0.5 wt. % CNC/PHB, the results from the one-tailed t-test indicated that the spherulites in the 1.0 wt. % CNC/PHB sample and the 0.5 wt. % CNC/PHB sample fell within the same population. No significant difference in the size of the spherulites of the 1.0 wt. % CNC/PHB sample and the size of spherulites of the 0.5 wt. % CNC/PHB sample was observed. These results were consistent with results from the thermal scan DSC

experiments, and these results suggested that the level of dispersion of the CNCs within the SC-H_2O was less homogeneous than the samples produced by the SC-EtOH.

The spherulite sizes within the ASCM samples also decreased with CNC loading. The average spherulite size was 184.8 ± 7.4µm, 63.1 ± 12.3µm and 50.8 ± 13.9µm for the neat PHB sample, the 0.5 wt. % CNC/PHB sample, and the 1.0 wt. % CNC/PHB sample, respectively. A one-tailed t-test was performed to compare the observed spherulite sizes of the neat PHB sample with the observed spherulite sizes of the 0.5 wt. % CNC/PHB sample. From the t-test, the probability that the spherulites of neat PHB and 0.5 wt. % CNC/PHB fell within the same size population was much less than 1%. The results indicated that the spherulite population of the neat PHB sample was distinctly different from the spherulite population of the 0.5 wt. % CNC/PHB sample. A one-tailed t-test was performed to determine if the spherulite population of the 1.0 wt. % CNC/PHB sample was different from the spherulite population of the 0.5 wt. % CNC/PHB sample. The results from the t-test suggested that the spherulite population of the 1.0 wt. % CNC/PHB was distinctly different from the spherulite population of the 0.5 wt. % CNC/PHB. These results indicated that increasing the loading of CNCs for 0.5 wt. % to 1.0 wt. % decreased the spherulite sizes of ASCM, suggesting that dispersion was not severely degraded as more CNCs were added with this processing method.

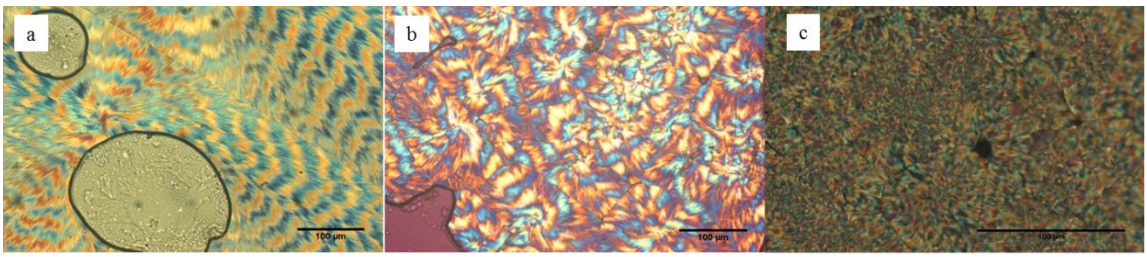

Figure 3.8. Optical microscopy images of the SC-EtOH samples with scale bar of 100µm: Neat PHB (a), 0.5 wt. % CNC/PHB (b), and 1.0 wt. % CNC/PHB (c).

3.3.5.3 Rate of crystallization

Using the data from the isothermal crystallization experiments, the spherulite radius was plotted as a function of isothermal hold time for the neat PHB sample. These results are shown in Figure 3.9. From this figure, differences in the growth rate of the neat PHB samples can be seen, and Figure 3.10 shows the difference in the nucleation density of ASCM samples. The images were captured at 40 s for neat PHB sample and at 5 s for the 0.5 wt. % CNC/PHB and 1.0 wt. % CNC/PHB samples. Table 3.1 contains the slope, intercept, and R^2 values from the linear regression performed on the spherulite radius as a function of time data for the neat PHB and 1.0 wt. % CNC samples for the ASCM, SC-EtOH, and SC-H_2O processing methods. From the linear regression, the values calculated for the slope can be used as the growth rates. Therefore for the neat PHB samples, the growth rate of the SC-EtOH was the greatest, and the growth rate of the SC-H_2O was the slowest. The growth rate of the ASCM neat PHB sample was between the values obtained for the SC-EtOH and the SC-H_2O samples. These results indicated that processing had an effect on the growth rate of the spherulites. From the literature, the presence of water has reduced the rate of spherulite growth of PHB,[163] and it has been suggested that water plays an active role in keeping PHB amorphous within bacterial granules.[164] Therefore it was expected that the growth rate of the SC-H_2O would be the slowest growth rate of all three processing methods. There were slight differences in the values of the slope and intercept between the neat and 1.0 wt. % CNC/PHB samples, and it is worth nothing that for the samples with nanoparticles, the cooling rate was not fast enough to completely inhibit crystallization during cooling to the isothermal temperature. Therefore some of the differences in the calculation of the slope and intercept were attributed to this. When comparing the growth rate of the neat PHB sample to the 1.0 wt. % CNC/PHB sample, the growth rate of the SC-EtOH processed samples remained relatively constant. The growth rate of ASCM processed samples decreased

with CNCs addition whereas growth rate of the SC-H_2O processed PHB increased with CNC addition. For the SC-H_2O sample, both nanoparticles and water were added into the PHB solution, therefore the increase in the crystallization rate could be due to the addition of the CNCs, which inhibits the plasticizing effect of the water. For the ASCM sample, there was a significant decrease in the rate of crystallization with nanoparticle addition. This decrease in the rate of crystallization could be due to the difference in the molecular mobility that occurs with the AS precipitation step. Because the AS processing of the CNC loaded samples was similar to many nanoencapsulation techniques, much more of the polymer was associated with the encapsulation of the CNCs that the molecular mobility of the polymers was reduced, thus decreasing the rate of crystallization. There is only a 0.03μ/s difference in the rate of crystallization for the SC-EtOH neat PHB and 1.0 wt. % CNC/PHB sample which was not a significant change as compared to the other processing methods.

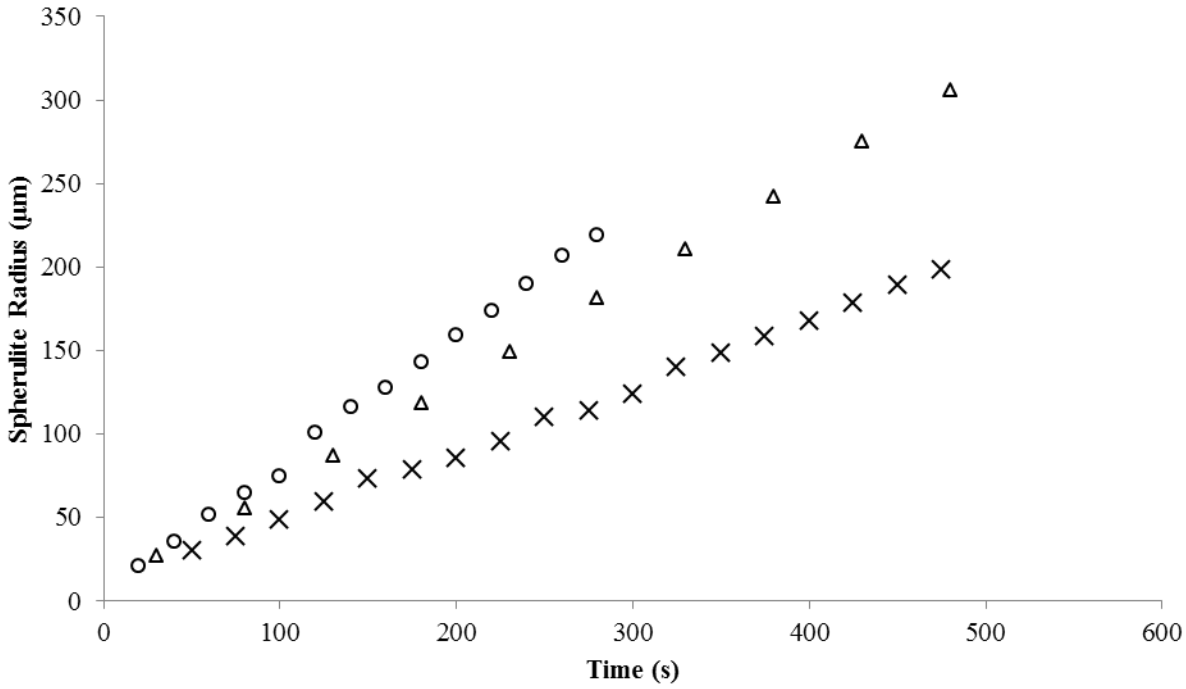

Figure 3.9. Spherulite radius as a function of isothermal crystallization time for the neat PHB processed via SC-EtOH (circle), SC-H_2O (x) and ASCM (triangle).

Table 3.4. Linear regression of the spherulite radius as a function of time for ASCM. SC-H_2O, and SC-EtOH samples.

		Slope(µm/s)	R^2
ASCM	Neat	0.62	99.99%
	1.0 wt.% CNC/PHB	0.36	98.55%
SC-H_2O	Neat PHB	0.40	99.74%
	1.0 wt.% CNC/PHB	0.52	97.86%
SC-EtOH	Neat PHB	0.77	99.85%
	1.0 wt.% CNC/PHB	0.74	96.33%

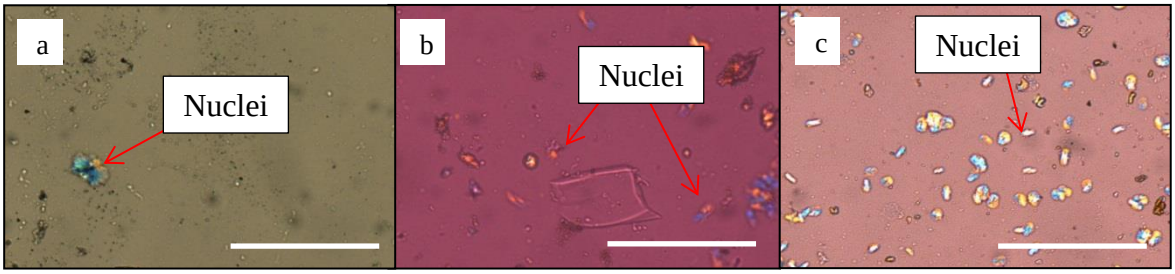

Figure 3.10. Differences in number of nucleation events occurring at 5s for ASCM neat PHB (a), 0.5 wt. % CNC/PHB (b) and 1.0 wt. % CNC/PHB(c). Scale bar is 100µm.

3.4 **FT-IR**

In order to compare the differences in the spectra, the spectra for the SC-EtOH, SC-H_2O, and ASCM samples were normalized to the peak at 1722 cm^{-1}. The full FT-IR spectra of the SC-EtOH, SC-H_2O and ASCM samples are shown in the Appendix as Figures A.3-A.5. There were differences between the neat PHB samples in fundamental regions such as the C=O stretching mode, which is the region from 1780-1680 cm^{-1},[120,165] shown in Figure 3.13 for the SC-EtOH, SC-H_2O, and ASCM samples. Typically a peak is seen at 1722 cm^{-1} that is associated with the ν(C=O) for the crystalline phase of PHB[120,156,166,167] and a peak at 1743cm^{-1} that is associated with the ν(C=O) of the amorphous phase.[120,156,166,167] For comparison, a FT-IR spectrum for a thin, solvent-cast neat PHB sample obtained from the literature is shown in Figure 3.12 with peak fitting performed to show to contribution of the individual curves to the overall spectra. The peak shape of the SC-H_2O and SC-EtOH samples appeared similar to the spectra shown in Figure 3.12, however the features in the spectrum for the ASCM sample appeared to have shifted. It is worth mentioning that in the all of the samples, there was a small peak that appeared at 1686 cm^{-1} which Zhang et. al. have attributed to a crystal defect caused by the interactions between an OH end group with a C=O group.[156]

In Figure 3.13, the differences in the absorbance spectra for the neat PHB, 0.5 wt. % CNC/PHB, and 1.0 wt. % CNC/PHB samples in the C=O region are shown. From this

figure, the curves for all of the SC samples appeared similar, indicating that the chemical structural of the C=O bonds within the SC samples were similar. For the ASCM samples, the intensity in at wavenumbers below 1720 cm^{-1} increased with increased CNC loading. From the literature, this region corresponds to hydrogen bonded C=O groups. [168] Therefore these results indicated that within the ASCM samples, as CNCs were added into the system, the amount of hydrogen bonded C=O groups increased.

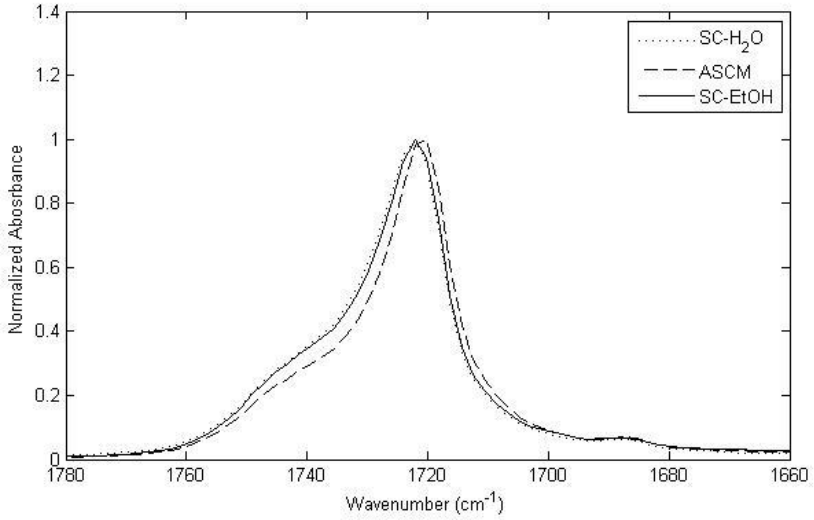

Figure 3.11. Normalized Spectra for the neat samples from 1660-1780 cm^{-1}.

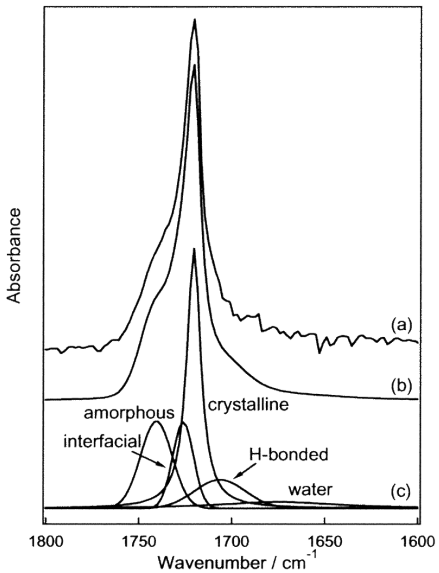

Figure 3.12. Curve-fitting of the carbonyl stretching vibration band of IR spectra of PHB film.[168]

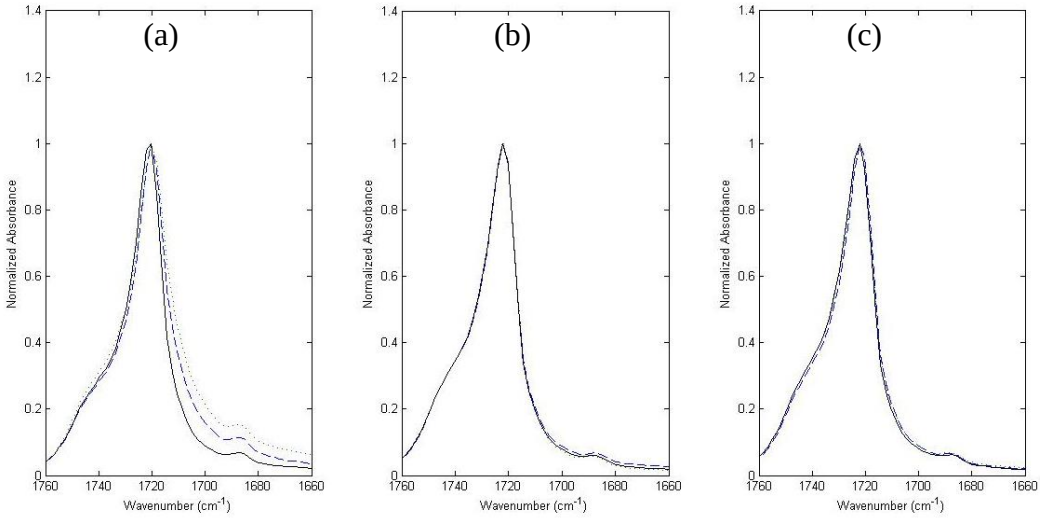

Figure 3.13. Absorbance spectra for the ASCM (a), SC-EtOH samples (b), and SC-H_2O samples (c) in the wavenumber range of 1760-1660cm^{-1} for neat PHB (solid), 0.5 wt. % CNC/PHB (dash), and 1.0 wt. % CNC/PHB (dot).

In addition to the C=O stretching bonds of PHB, the C-H stretching region (3050 -2850 cm^{-1}) was another area within the FTIR spectra used to describe the chemical structure of the crystalline and amorphous components of the PHB based materials. The spectra for the neat PHB processed by the SC-EtOH, SC-H_2O, and ASCM methods are shown in Figure 3.14. Peaks at 3007, 2997, 2987, 2976, 2966, 2935, 2927, and 2875 cm^{-1} were observed in all of the SC samples. The peaks at 3007, 2976, 2966, 2935, and 2927 cm^{-1} were bands associated with the semicrystalline structure that developed during crystallization of the PHB.[116,156] The peaks at 2976 and 2966 cm^{-1} and the peaks at 2935 and 2927 cm^{-1} were from crystal field splitting which can be caused by intermolecular interaction due to the formation of a helix structure.[169] From the figure, the intensity of the peak at 2935 cm^{-1} of the ASCM sample was significantly greater than the SC samples, and the peak at 2927cm^{-1} was only resolved in the ASCM sample. Therefore, these results suggested that more of the helix structure was present in the ASCM sample compared with the SC samples. This result was consistent with the result obtained from the thermal scans discussed earlier in this chapter. The peak at 2876 cm^{-1} was observed in all of the spectra, however the peak was shifted to higher values for the SC samples. From melt crystallization studies on PHB, a C-H stretching band shifted from 2878 cm^{-1} in the amorphous melt to 2873 cm^{-1} at room temperature,[115,156] and this peak was associated with the conformational transition of PHB from disordered to ordered associated with the crystallization of the amorphous component .[115,156] Therefore these results suggested that there was more amorphous content in the neat SC samples when compared with the neat ASCM samples. This result was consistent with the results obtained from DSC. The peak at 3007 cm^{-1} corresponded with the intermolecular hydrogen bonding ($CH_3\cdots O=C$) occurring in the PHB crystals,[156] and these intermolecular hydrogen bonds have been shown to stabilize the lamellar structure of the PHB and affect the thermal behavior, crystallinity and stability of the crystallites.[167]

Amorphous peaks of PHB were at 2997 cm^{-1} and 2986 cm^{-1}. The peak at 2986 cm^{-1} became more pronounced in the SC samples than in the ASCM samples. This increase the amorphous peak observed was indicative of packing density reduction which occurs in the melting phase,[170] which was consistent with the results from the DSC experiments. In Figure 3.15 the differences between the neat PHB and the CNC/PHB loaded samples are shown. For the ASCM sample, as CNC are added, the intensity at 2976 cm^{-1} increased. This result suggested that there was an increased amount of the helix structure present, increasing CNC loading. A similar behavior was observed in the SC-EtOH sample. These results were consistent with the results obtained from DSC that show that when CNCs are added, the crystallinity increased. At a loading of 0.5 wt. % CNC, the peak at 2935 cm^{-1} was decreased in the ASCM sample whereas at a loading of 1.0 wt. % CNC, the peak at 2935 cm^{-1} was significantly increased. As stated previously, this peak was associated with intermolecular or intramolecular interactions involved in the formation of the helix structure, For the SC-EtOH sample, the addition of CNC increased the absorbance at 2935 cm^{-1}. These results suggested that the addition of CNCs during the SC processing increased the amount of interactions involved in forming the helix structure.

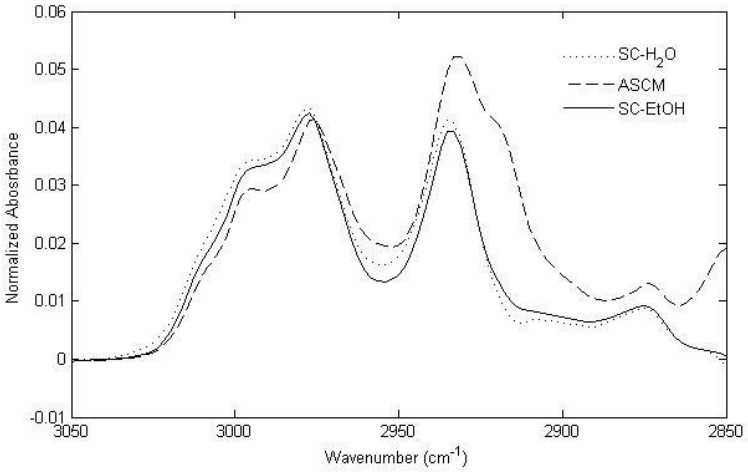

Figure 3.14. IR spectra for the neat PHB samples from 3050-2850 cm^{-1}.

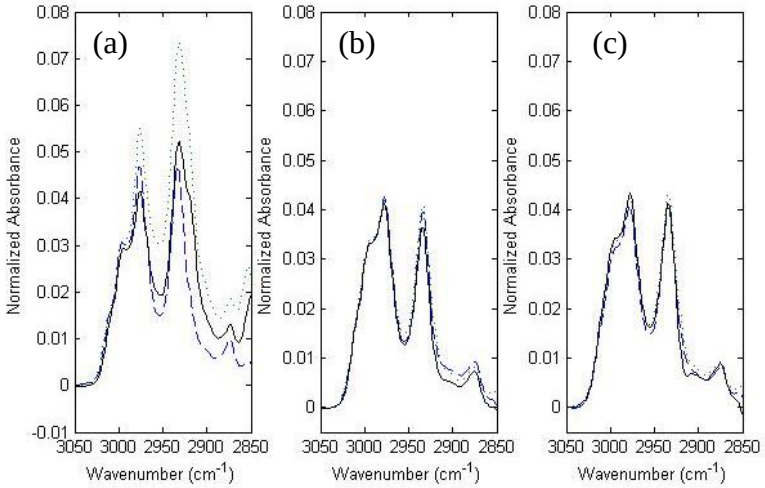

Figure 3.15. FT-IR spectra in the 3050-2850 cm^{-1} region for neat PHB (solid), 0.5 wt.% CNC/PHB (dash) and 1.0 wt. % CNC/PHB (dot) for ASCM(a) SC-EtOH (b) , SC-H2O (c) samples.

The FT-IR spectra of the samples in the range 3000-3600 cm^{-1}, which corresponded to the ν(OH) vibration of several hydroxyl groups present in the PHB, is shown in Figure 3.16 for neat PHB and in Figure 3.17 for the CNC/PHB samples. A peak was observed at 3437 cm^{-1} for all samples, and the peak corresponded to the ν(OH···O) vibration of hydrogen bonding between the hydroxyl group of PHB with the OH group of the adjacent molecule.[171] In Figure 3.16, both the SC-EtOH and the ASCM neat PHB

samples had a broad peak occurring between 3500 and 3100cm^{-1}. This broad peak was not observed in the SC-H2O sample. From the literature, the broad peak occurring between 3100 cm^{-1} to 3500 cm^{-1} has been associated with the intra-molecular hydrogen bonding occurring.[167,172] Therefore these results suggested that the presence of water inhibited the intramolecular hydrogen bonding that occurring within SC-H_2O sample. These intramolecular hydrogen bonds played a role in the crystallization of PHB.[60,118] These results also supported the results from the DSC and hot stage experiments which have shown that the addition of water reduces the rate of crystallization. In Figure 3.17, the spectra of the CNC/PHB are shown. For the ASCM samples, the broad peak was reduced with the addition of CNC, indicating that the addition of CNC reduced the amount of intramolecular hydrogen bonding that occurs, and the peaks shifted to slightly lower wavenumbers. From the literature, when cellulose and PHB interact, some of the intramolecular hydrogen bonds of PHB were weakened and strong hydrogen bonds occurred between the OH groups of the cellulose and PHB.[171] This result was expected because during the AS process, the PHB precipitates but when CNCs are added, interactions between the CNC and PHB could hinder the intramolecular hydrogen bonding that occurs in PHB. A different trend was observed for the SC-EtOH samples. For the 0.5 wt. % CNC/PHB sample, the broad peak associated with intramolecular hydrogen bonding was increased whereas for the 1.0 wt. % CNC/PHB sample the broad peak associated with intramolecular hydrogen bonding was smaller than the neat PHB sample. These results suggested that for the SC-EtOH sample, the amount of CNC–PHB interactions and the effect of these CNC-PHB interactions on the amount of intramolecular hydrogen bonding of PHB were dependent on the CNC loading. When a small amount of CNCs were added, the amount of intramolecular hydrogen bonding was increased but as the loading of CNCs increased the amount of intramolecular hydrogen bonding decreased. This behavior at 0.5 wt. % CNCs was consistent with the trend

observed in the SC-H_2O samples, whereas at 1.0 wt. % CNCs, the amount of intramolecular hydrogen bonding decreased like the ASCM samples. These results suggested that for the SC-EtOH samples, the loading of the CNCs influenced how much intramolecular bonding that occurred. This result could be due to the fact that in the SC-EtOH processing the as-received CNC suspension was was diluted with ethanol. For the SC-EtOH neat PHB sample, only ethanol was added during processing, whereas for the SC-EtOH CNC/PHB samples, the CNC suspension was added. Therefore the both ethanol and water influence how the structure of the CNC loaded SC-EtOH samples develop. For the SC-H_2O sample, the intensity of the broad peak at 3100cm^{-1} to 3400cm^{-1} increased as the CNCs loading increased, thus indicating that the amount of intramolecular hydrogen bonding increased with CNC loading. These results suggested that the addition of CNCs suspended in water increased the amount of intramolecular hydrogen bonding. Since the amount of intramolecular bonding was an indication of the rate of crystal growth, this result was consistent with the results obtained from hot stage microscopy which showed that the addition of CNC significantly increased the growth rate of the spherulites for the SC-H_2O samples.

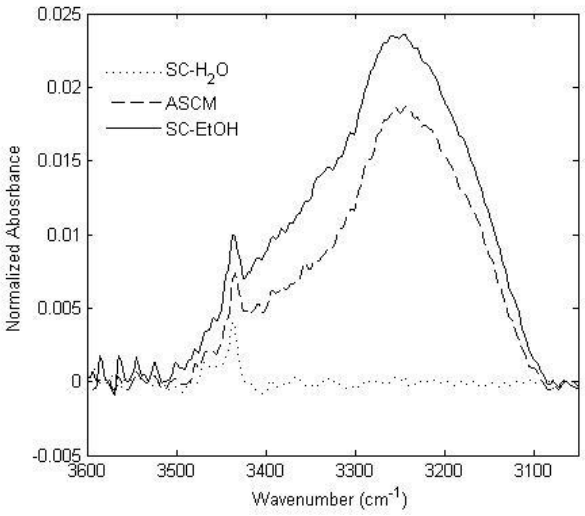

Figure 3.16. Spectra of neat PHB from 3600-3050cm^{-1}.

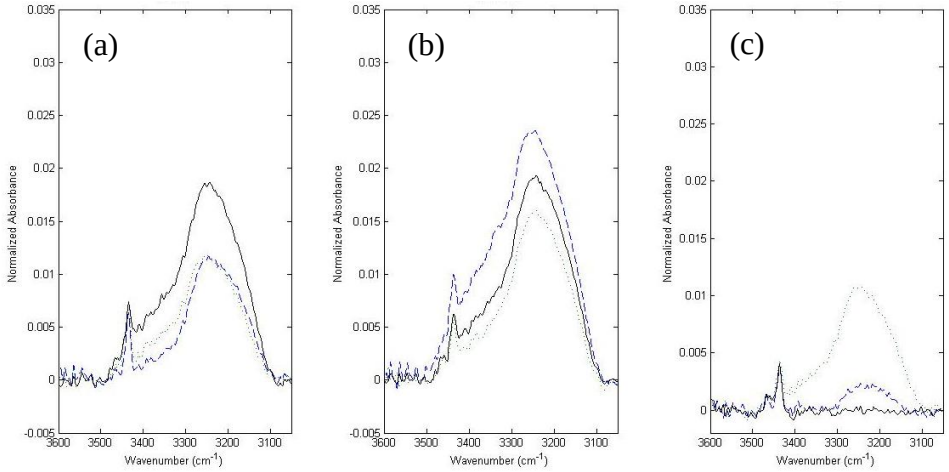

Figure 3.17. FT-IR spectra in the 3050- 3600 cm^{-1} region for neat PHB (solid), 0,5 wt. % CNC/PHB (dash) and 1.0 wt.% (dot) for (a)ASCM, (b)SC-EtOH and (c) SC-H_2O

3.5 **Conclusions**

In this chapter, differences in the morphology of CNC/PHB nanocomposites processed in four different ways were characterized using DSC, hot stage microscopy and FT-IR spectroscopy. For all processing methods, the addition of CNCs increased the T_c during cooling and increased the isothermal crystallization kinetics. The T_c peak of the CNC loaded samples exhibited both an increase in the temperature at which the T_c occurred as well as an increase in the slope of the crystallization peak. This behavior was consistent with the behavior of a nucleating agent and has been observed in PHB when nucleating agents such as sterocomplexed polylactide[173] and kenaf fibers.[149] Therefore, the results suggested that the addition of CNCs into PHB act as a nucleating agent regardless of processing method.

For the SC-based methods, using a water-based CNC suspension resulted in slower crystallization kinetics and MRR behavior when compared with the ethanol-based CNC suspension. The role of CNC-water interactions on the MRR behavior of PHB was

similar to the results obtained from solvent cast CNC/PHBV composites.[109] The difference in the morphology between these two methods was attributed to the role of water suppressing the intramolecular hydrogen bonding in PHB. The result was supported by a presence of a smaller peak associated with intramolecular hydrogen bonding present in the FT-IR spectra of SC-H_2O samples, which were significantly larger in the FT-IR spectra of either SC-EtOH or ASCM samples. Therefore these results suggest that the solvent used in dilution of the CNCs during the processing impacted the kinetics of crystallization.

In the DSC-based isothermal crystallization experiments, the AS-based methods of processing increased the kinetics of crystallization of the CNC loaded samples during isothermal crystallization at 120˚ C; however the rate of spherulite growth for the SC-EtOH sample (observed using hot stage microscopy) was greater than the spherulite growth rate of the ASCM samples. The addition of nanoparticles resulted in a significant reduction in the spherulite size for SC-EtOH, SC-H_2O and ASCM processing methods. However there was a statistically significant size reduction due to the increase in nanoparticle loading for the SC- EtOH and ASCM samples, which suggested that significant additional agglomeration did not occur in these samples as CNC concentration was increased from 0.5 to 1.0 wt.%. This reduction in average spherulite size was not observed in the SC-H_2O sample, which indicated that a lesser degree of dispersion was attained in these samples. From FT-IR, differences in OH region of the neat PHB processed in the different methods were seen. These results suggested that processing methods influenced how the semicrystalline structure of the neat PHB samples formed. In a likewise manner, different trends were observed in the CNC/PHB samples. As CNCs were added during the ASCM processing, the peak associated with intramolecular hydrogen bonding was decreased, suggesting that as CNCs were added the amount of intramolecular hydrogen bonding associated with PHB decreased. A different trend was

observed in the SC-H_2O samples, as CNCs were added, the amount of intramolecular hydrogen bonding increased with increased CNC loading. For the SC-EtOH samples at 0.5 wt. % CNC/PHB, the amount of intramolecular hydrogen bonding increased relative to the neat PHB sample, but at 1.0 wt. % the amount of intramolecular hydrogen bonding was decreased. These results provided evidence regarding the differences in the chemical structure as a result of processing method and provided evidence regarding the role of the solvent in the development of the semicrystalline structure.

CHAPTER 4

FLASH DSC

4.1 Introduction

As discussed in Chapter 2, the nanophases present within a semicrystalline polymer play an important role in its properties and how its structure evolves. When a nanoparticle is added into a semicrystalline polymer matrix, new nanophases can be formed due to the interactions between the polymer and the nanoparticle. Several studies have shown that the presence of a nanofiller has allowed for the formation of crystalline phases of the polymer that do not typically form under normal processing conditions. For example, the addition of MMT to PA6 promoted the formation of the γ phase , and the authors attributed this to the interactions between the PA6 and the MMT.[174,175] The γ phase of the PA6 was only observed in the interphase region, and the α phase of PA6 existed away from the PA6- MMT interphase.[175] Therefore, it is important that the nature of the matrix-filler interaction be examined. By manipulating the cooling and isothermal crystallization temperature, a better understanding of how nanoparticle addition affects the mechanisms associated with nucleation as well as the kinetics of crystallization can be obtained. [176]

The objective of experiments described in this chapter was to characterize the crystallization behavior of PHB with and without nanofillers using FDSC. The faster heating rates suppress reorganization upon heating, allowing the melting behavior produced by the cooling protocol to be observed. Also at slower heating rates, the reorganization behavior of the polymer crystallized at low temperatures can be studied.[95,97] As an example, the effect of heating rate on PET's ability to recrystallize can be seen in Figure 4.1 using data obtained from FDSC. At the slowest heating rate (160 ˚C/s), two distinct melting peaks were be observed. However at higher heating rates

(1100 ˚C/s and 2700 ˚C/s), only one crystallization peak was observed. These results suggested that the kinetics of recrystallization can be studied by FDSC when the cooling rate was held constant and the heating rates were varied.[148,177]

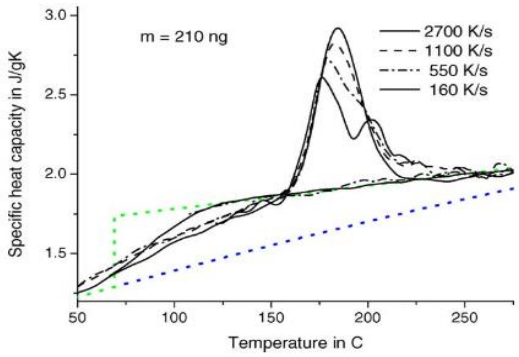

Figure 4.1.Heat capacity of PET at different heating rates, measured from fast cooling from crystallization with dotted lines corresponding to crystalline and amorphous PET. [177]

Faster cooling rates allow for the production of amorphous samples by suppressing crystallization,[75] as well as the formation of different crystal phases and/or mesophases.[95,99] Also, the faster cooling rates available allow for the study of isothermal crystallization at lower temperatures than those accessible with conventional DSC.[146]

In this chapter, the results of a series of experiments performed using Flash DSC are presented for the ASCM and SC-EtOH samples. These experiments were designed to observe differences in the nonisothermal and isothermal crystallization behavior of PHB. The effect of adding nanoparticles was also studied using the same nonisothermal and isothermal crystallization experiments. From these experiments, relationships between processing and crystal structure in neat PHB and CNC/PHB nanocomposites were obtained.

4.2 Experimental materials and methods

4.2.1 Flash DSC Measurements

A Mettler Toledo Flash DSC and MultiSTAR UFS 1 sensor chips made by Xensor Integration were used in this work. The Flash DSC uses microelectromechanical system (MEMS) based sensors to heat samples at a rates of 0.5 ˚C/s to 40,000 ˚C/s and cool samples at rates up to -0.1 ˚C/s and -4,000 ˚C/s.[178] The sensor chip contains the calorimeter and consists of a silicon nitride/oxide dielectric membrane surrounded by a silicon frame and a larger ceramic support frame. 16 thermopiles are used to measure the temperature of the sample relative to the ceramic plate and located around the sample target area.[179] There are two types of resistive heaters on the chip; one heater is used to control the temperature during the experiments, and a compensation heater is used for the dynamic power compensation during the experiments.[93,179] Typical samples sizes are between 10 ng and 1 µm.[93]

Variable heating-constant cooling (VH-CC), constant heating-variable cooling (CH-VC), Isothermal crystallization-variable heating (IC-VC) and isothermal crystallization experiments were performed on the PHB samples. For each experiment, pre and post experiment heat and cool cycles were performed, and the thermal transition behaviors obtained were compared to check for thermal degradation during the experiment. Prior to the experiments, each chip sensor was subjected to three conditioning cycles to exercise the membrane and a temperature correction protocol. Samples of 30-50 µm thickness were prepared by microscope aided cutting. The samples were placed directly onto the target area of the chip sensor which had been heated to 160 ˚C, so that the samples would adhere onto the chip sensor. Dry argon was used as a purge gas at a rate of 22 mL min^{-1} during all of the Flash DSC experiments, including the

sensor conditioning and temperature correction experiments. The experiments performed are described below.

4.2.2 Variable heating-constant cooling (VH-CC)

In the VH-CC experiments, the effect of the heating rate on the reorganization behavior of PHB was studied. In the VH-CC experiments, the sample was heated and cooled from -40 ˚C to 195 ˚C with a 0.1 s isothermal step at 195 ˚C and -40 ˚C. The heating rates used in this experiment were 5 ˚C/s, 10 ˚C/s, 50 ˚C/min, 100 ˚C/s, 150˚C/s, 200 ˚C/s, and 300 ˚C/s. A cooling rate of 1 ˚C/s (60 ˚C/min) was used in the VH-CC experiments.

4.2.3 Variable cooling-constant heating (VC-CH)

In the VC-CH experiments, the effect of the cooling rate on the crystallization behavior of PHB was studied. In the VC-CH experiments, the sample was heated and cooled from -40 ˚C to 195 ˚C with a 0.1s isothermal step at 195 ˚C and -40 ˚C. Cooling rates of 0.5 ˚C/s, 1 ˚C/s, 1.5 ˚C/s, 5 ˚C/s, 8 ˚C/s, 10 ˚C/s, and 12 ˚C/s were used, and a heating rate of 300 ˚C/s was used.

4.2.4 Isothermal crystallization experiments

For the isothermal crystallization experiments, different isothermal crystallization times and temperatures were used in order to obtain information regarding the crystallization behavior over a wide range of times and temperatures.

4.2.4.1 Isothermal crystallization-variable heating (IC-VH) at 90 ˚C

In the IC-VH experiment performed at 90 ˚C, the minimum heating rate at which the reorganization of the polymer was suppressed was determined. In these experiments, the sample was heated from 25 ˚C to 195 ˚C at 100 ˚C/s and held for 0.5 seconds at 195

˚C. Then, the sample was instantantously cooled to 90 ˚C and held at 90 ˚C for 100s. Next, the sample was instantantously cooled to -40 ºC and held at -40 ºC for 0.5 seconds. Finally, the sample was the heated to 195 ˚C from -40 ˚C at 300 ˚C/s.

4.2.4.2 Isothermal crystallization at 25˚C-135˚C

For this experiment, the sample was heated from 25 ˚C to 195 ˚C at a heating rate of 300˚C/s then held for 0.5 s at 195 ˚C. The sample was instantantously cooled to a isothermal crystallization temperature between 25 ˚C and 130 ˚C and held at the crystallization temperature for a predetermined time period (10s, 20s, 60s, 500s). The sample was then instantantously cooled to -40 ˚C and held at -40 ˚C for 0.5 seconds. The sample was the heated to 195 ˚C from -40 ˚C at 300 ˚C/s.

4.2.5 Calculation of sample mass

The Flash DSC measures the differential heat flow between the sample and the reference calorimeters, and the data obtained is in milliwatts. In order to compare one sensor measurement to another, the heat flow curves were normalized to heating rate and sample size. Since the sample mass cannot be directly measured for the Flash DSC, the sample mass is often calculated using the measured absolute heat capacities of the samples at temperatures above the melting point with specific heat capacity data obtained from the ATHAS database.[93,180] The absolute heat capacity of PHB was not available in ATHAS database, and thermal degradation of PHB can occur at temperatures above 170 ˚C.[137] Therefore, the sample mass was calculated from the glass transition step of a completely amorphous sample and normalized to the difference between the solid and liquid values for heat capacity at the temperature of the glass transition. The heat capacity equations used for the calculation of the sample mass of PHB were obtained from the

literature. The equations for the heat capacity of the solid PHB ($c_{p,solid}$) and the heat capacity of liquid PHB ($c_{p,liquid}$) are shown in the equations below:[87]

$$c_{p,liquid(T)} = 1.1 Jg^{-1}K^{-1} + 0.00208 Jg^{-1}K^{-2} \times T$$
$$c_{p,solid(T)} = 0.22 Jg^{-1}K^{-1} + 0.0035 Jg^{-1}K^{-2} \times T$$

For the experiments described here, the calculated sample mass for the ASCM neat PHB sample was 3413.4 ± 21.3 ng, and the calculated sample masses for the SC-EtOH neat PHB sample was 856.6 ± 4.6 ng. The calculated sample mass of the SC-EtOH 0.5 wt. % CNC/PHB sample was 124.14 ± 5.2ng and the calculated sample mass of the SC-EtOH 1.0 wt. % CNC/PHB sample was 821.4 ± 8.2ng. The calculated sample mass on the chip sensor of the ASCM 0.5 wt. % CNC/PHB sample was 2161.4 ± 29.5ng, and the calculated sample mass on the chip sensor of the ASCM 1.0 wt. % CNC/PHB sample was 1552.6 ± 21.5ng.

4.2.6 Melting peak calculations

Because melting-recrystallization-remelting (MRR) behavior has been observed in PHB, the peak value of the melting point is not always an accurate description of the melting process of PHB. The melting onset temperature (T_{on}) is independent of thermal lag and recrystallization of the polymer;[181] therefore, T_{on} was used to described the melting behavior of PHB. The method used to calculate T_{on} is described in the literature[146,181] and shown in Figure 4.2. To determine $T_{on,}$ a linear baseline was extrapolated from the heat capacity curve before melting and the linear fit to the steepest portion of the melting peak was also constructed, the point at which these two lines intersected was T_{on}.[146,181]

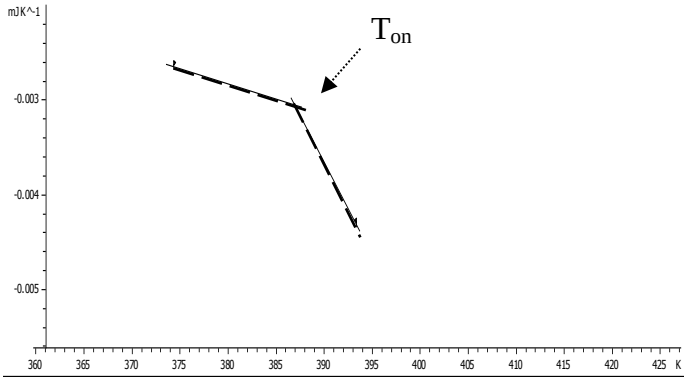

Figure 4.2. Schematic of the determination of the melting onset.

4.2.7 Percent crystallinity calculations

Using the sample mass, the percentage of crystallinity within the sample was calculated using the equation below:

$$X_c(\%) = \frac{\Delta H_m}{\Delta H_0 (1 - X_{CNC})} \times 100 \quad (1)$$

where ΔH_m is the experimentally-obtained enthalpy of melting, and ΔH_0 is the theoretical enthalpy of melting for a 100% crystalline PHB sample which is 146 J/g.[125]

4.3 Results from VH-CC experiments

4.3.1 SC-EtOH samples

Significant differences were observed between the composite samples and the neat PHB sample. The melting curves for the samples are shown in Figure 4.3. Differences in the cold crystallization behavior and melting behavior were observed. In the neat PHB sample, there were multiple melting peaks observed at heating rates of 5

˚C/s, 10 ˚C/s, 50 ˚C/s, whereas a single melting peak was observed in the 0.5 wt.% CNC/PHB and 1.0 wt. % CNC/PHB samples at the same heating rates.

At heating rates of 5 ˚C/s and 10 ˚C/s, a cold crystallization peak was observed in the all of the SC-EtOH PHB samples. At a heating rate of 5 ˚C/s, the peak of cold crystallization for the neat sample occurred at approximately 91˚C with an onset around 77 ˚C, whereas for the 0.5 wt. % CNC/PHB the peak of cold crystallization occurred around 75 ˚C with the onset occurring at approximately 55 ˚C and for the 1.0 wt.% CNC/PHB sample, the peak of cold crystallization occurred at ~ 80˚C with onset occurring around 70 °C. The calculated enthalpy from the cold crystallization peaks were 65.7 J/g, 53.5 J/g and 46.3 J/g for neat PHB, 0.5 wt.% CNC/PHB and 1.0 wt.% CNC/PHB samples, respectively.

Table 4.1summarizes the T_{on}, T_m, enthalpy of melting, and crystallinity data for the neat PHB, 0.5 wt. % CNC/PHB and 1.0 wt. % CNC/PHB samples prepared by the SC-EtOH processing method. The addition of the nanoparticles increased the crystallinity of PHB from less than 20% for the neat PHB sample to ~40%for the 0.5 wt. % CNC/PHB and ~50% for the 1.0 wt. % CNC/PHB. There was an increase in T_{on} as nanoparticles were added to PHB. The increase in the T_{on} was greatest in the 1.0 wt. % CNC/PHB sample, whereas the difference in T_{on} between the neat PHB and the 0.5 wt. % CNC/PHB samples was negligible even thought there was a significant difference in T_m. These differences in T_m were due to differences in the melting peak. From Figure 4.3, the melting peak in the 0.5 wt. % CNC/PHB sample at a heating rate of 50 ˚C/s occurred at a lower temperature and was narrower than melting peak of the neat PHB.

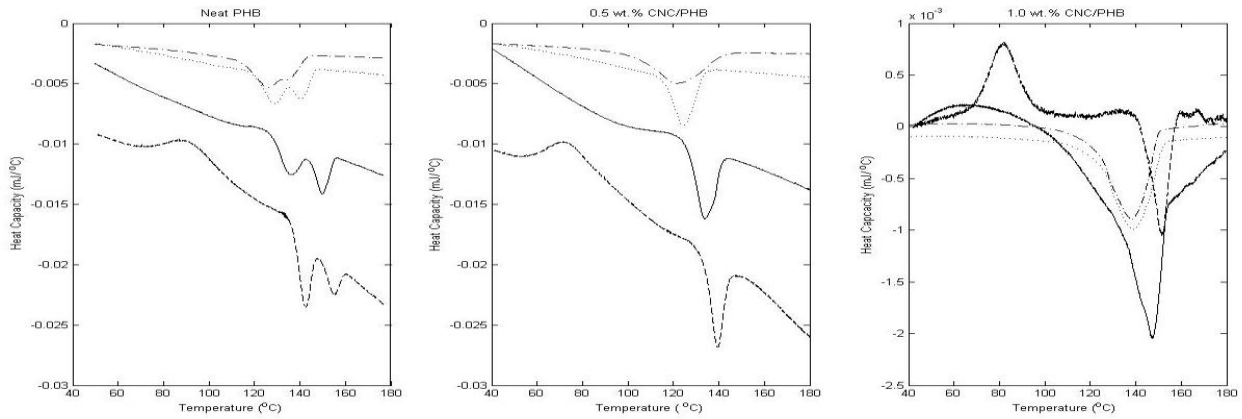

Figure 4.3. Comparison of the melting curves from heating rates of 5 ˚C/s (dash), 10 ˚C/s (line), 50 ˚C/s (dot), and 200 ˚C/s (dash dot) for Neat PHB, 0.5 wt. % CNC/PHB and 1.0 wt. % CNC/PHB.

Table 4.1. Summary of the T_{on}, T_m, enthalpy and crystallinity for the VH-CC experiments for SC-EtOH samples.

Heating Rate (°C/s)		**5**	**10**	**50**	**100**	**150**	**200**	**300**
Neat PHB	T_{on} (˚C)	138.0	131.4	111.0	110.2	109.6	107.0	107.0
	T_m (˚C)	143.4	139.7	126.4	124.4	123.1	127.6	127.1
		155.9	152.2	138.1	135.9	133.2		
	Enthalpy (J/g)			23.4	21.9	19.6	19.3	19.1
	Crystallinity			16.0%	15.0%	13.4%	13.2%	13.1%
0.5 wt.% CNC/PHB	T_{on}(˚C)	133.9	126.9	115.6	111.9	110.9	108.1	107.3
	T_m(˚C)	139.4	133.7	124.4	122.9	121.6	122.0	120.8
	Enthalpy (J/g)			51.0	47.5	54.8	56.3	56.8
	Crystallinity			34.5%	32.5%	37.6%	38.6%	38.9%
1.0 wt.% CNC/PHB	T_{on} (˚C)	140.6	135.1	124.9	125.4	125.0	125.5	124.5
	T_m(˚C)	151.2	147.4	138.6	137.8	138.3	139.3	139.5
	Enthalpy (J/g)			77.9	80.6	78.8	78.6	77.1
	Crystallinity			53.4%	55.2%	54.0%	53.8%	52.8%

4.3.2 ASCM Samples

The melting peaks obtained from the VH-CC experiments are shown in Figure 4.4 for neat PHB, 0.5 wt. % CNC/PHB, and 1.0 wt. % CNC/PHB samples. The shapes of the melting peaks for the neat PHB sample (Figure 4.3) were similar to the melting peaks that were observed in the samples with CNCs. In the melting curves of the ASCM samples at a heating rate of 5 ºC/s, cold crystallization occurred upon heating. The temperature at the peak of the cold crystallization peak provided information regarding how adding nanoparticle altered the recrystallization behavior. The cold crystallization peak of the ASCM neat PHB sample was 87.5 ºC with an onset of ~76.1 ˚C. The cold crystallization of the ASCM 0.5 wt. % CNC/PHB was 69.9 ºC with an onset temperature of 56.7 ˚C, and the cold crystallization peaks for the 1.0 wt. % CNC/PHB sample was 82.1 ºC with an onset temperature of 68.4˚C. The enthalpy calculated from the cold crystallization peaks were 44.8 J/g, 41.9 J/g and 40.5 J/g for the neat PHB, 0.5 wt. % CNC/PHB, 1.0 wt. % CNC/PHB, respectively. At a heating rate of 10 ºC/s, a cold crystallization peak was observed in the neat PHB sample, but no distinguishable cold crystallization behavior was observed in the heat capacity curves of the 0.5 wt. % CNC/PHB sample and 1.0 wt. % CNC/PHB.

The values obtained from the heat capacity curves for the T_{on}, T_m, enthalpy of melting, and crystallinity for the ASCM samples are shown in Table 4.2. No MMR behavior was observed for these samples, unlike the SC-EtOH samples. As the heating rate was increased from 5 ˚C/s to 150 ˚C/s, T_{on} and T_m decreased for all ASCM samples. As the heating rate was increased to 200 ˚C/s, T_{on} of the neat PHB and 0.5 wt. % CNC/PHB samples remained constant, whereas T_{on} of the 1.0 wt. % CNC/PHB continued to decrease. As the heating rate was further increased to 300˚ C/s, T_{on} of 1.0 wt. % CNC/PHB became constant with heating rate. For T_m, behavior similar to that of T_{on} was observed. T_m of the ASCM samples decreased as the heating rate was increased from 5

˚C/s to 200 ˚C/s. As the heating rate was further increased from 200 ˚C/s to 300 ˚C/s, T_m of the neat PHB, 0.5 wt. % CNC/PHB, and 1.0wt. % CNC/PHB increased. The crystallinity values of the neat PHB were the smallest of all 3 samples, with ~24% crystallinity, whereas the CNC loaded samples had significantly higher amount of crystallinity. The 1.0 wt. % CNC/PHB sample had the greatest amount of crystallinity at 70%, and the 0.5 wt. % CNC/PHB sample was 67% crystalline.

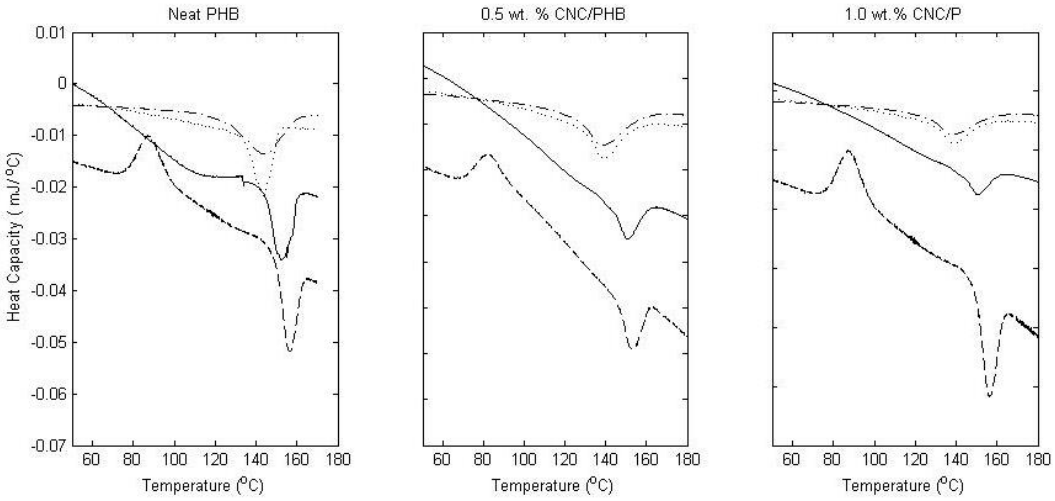

Figure 4.4. Melting curves obtained from VH-CC experiments performed at -1 °C/s cooling on the ASCM samples. Data obtained at heating rates of 5 ˚C/s (dash), 10 ˚C/s (solid), 500 ˚C/s (dot), and 200 ˚C/a (dot-dash) are plotted.

Table 4.2. Summary of the T_{on}, T_m, enthalpy and crystallinity for the VH-CC experiments for the ASCM samples.

Heating Rate (°C/s)		5	10	50	100	150	200	300
Neat PHB	T_{on}(˚C)	149.9	144.9	143.8	130.9	129.5	128.9	128.9
	T_m(˚C)	156.4	152.7	143.9	140.9	140.7	140.2	144.6
	Enthalpy (J/g)			35.5	35.2	35.4	35.7	36.4
	Crystallinity			24.4%	24.1%	24.3%	24.4%	24.9%
0.5 wt. % CNC/PHB	T_{on}(˚C)	142.6	129.5	117.4	112.6	111.0	109.3	110.2
	T_m(˚C)	155.1	136.5	125.9	124.0	124.3	123.3	123.4
	Enthalpy (J/g)			101.0	98.1	98.1	97.8	103.8
	Crystallinity			69.2%	67.2%	67.2%	67.0%	71.1%
1.0 wt.% CNC/PHB	T_{on}(˚C)	142.3	140.9	130.2	127.7	126.4	124.8	124.5
	T_m(˚C)	153.2	150.8	139.7	139.2	137.4	136.9	138.2
	Enthalpy (J/g)			102.9	106.2	103.9	102.8	104.5
	Crystallinity			70.4%	72.8%	71.2%	70.4%	71.6%

4.3.2.1 Discussion of VH-CC results

In the VH-CC experiments the effect of heating rate on the recrystallization behavior and structure formation that occurred upon heating was examined. The effect of heating rate on the recrystallization behavior has been observed in many different types of polymer systems such as PA 6[180] and PET.[148] Even though PHB crystallizes relatively slowly, PHB still exhibits MRR behavior upon heating but no lamellar thickening occurs while in the solid state.[182–184] Therefore, information about the original crystals can be obtained by preventing the reorganization. This reorganization behavior can be prevented by using high crystallization temperatures and high heating rates.[97] Previous studies have shown that for PHB crystallized at isothermal temperatures greater than 115 ˚C, a heating rate of 1 ˚C/s was sufficient to prevent the reorganization.[185]

The presence of a cold crystallization peak upon heating indicated that crystallization was not completed at a cooling rate of 1 ˚C/s (60 ˚C/min). At heating rates

of 5 ˚C/s cold crystallization peaks were observed in all of the samples, and at a heating rate of 10 ˚C/s both neat samples exhibited a cold crystallization peak also. These results indicated that a heating rate of 10 ˚C/s was not sufficient to prevent the reorganization behavior of PHB. This result was consistent with what was expected because a rate of 1 ˚C/s was need to suppress the reorganization behavior of a PHB sample crystallized at 115 ˚C for 30 minutes:[185] Therefore, a faster rate would be necessary to prevent the reorganization upon heating of a partially crystallized sample. The enthalpy of cold crystallization was calculated for all samples at a heating rate of 5 ˚C/s. For each processing method, the 1.0 wt. % CNC/PHB sample had the smallest calculated enthalpy for the cold crystallization peak, and the neat PHB sample exhibited the largest. These results were expected because previous studies have shown that the addition of nanoparticles into PHB inhibited reorganization upon heating.[147] In a likewise manner, the SC-EtOH sample exhibited multiple melting peaks upon heating. The magnitude of the higher temperature endotherm decreased as the heating rate was increased. This behavior was not observed in the SC-EtOH samples that contained CNCs. These results suggested that MRR occurred in the neat PHB sample but not in the samples where CNCs were added.

As the heating rate increased, T_{on} and T_m decreased. However, the heating rate at which T_{on} became constant varied between the different samples, but for all samples, T_{on} at 5 ˚C/s and 10 ˚C/s were significantly higher than T_{on} at the higher heating rates. As stated previously, cold crystallization was observed in the heating curves at heating rates of 5 ˚C/s and 10 ˚C/s for both the ASCM and SC-EtOH neat PHB samples; therefore, the reorganization/recrystallization upon heating caused the onset to shift to higher temperatures. This increase in the value of T_m at slower heating rates has been associated with the polymer undergoing reorganization during heating.[148] As the heating rate is increased, if the reorganization is inhibited, the T_{on} and T_m should remain

relatively constant. For the SC-EtOH samples, the T_{on} and T_m became constant at heating rates around 200 ˚C/s, and the T_m did not increase significantly as the heating rate increased to 300˚C/s. For the ASCM samples, the T_{on} and T_m became constant at heating rates of 100 ˚C/s for the neat PHB and 0.5 wt. % CNC/PHB samples. For the 1.0 wt. % CNC/PHB sample, the T_{on} and T_m became constant as the heating rate was increased from 200 ˚C/s to 300 ˚C/s

In the VH-CC experiments, it is expected that at heating rates sufficiently fast to prevent reorganization, the enthalpy of melting and the % crystallinity should remain relatively constant. However if the sample is large, thermal gradients can occur within the sample during fast heating or cooling. This effect is referred to as thermal lag, and often times manifests itself as smearing of the melting peaks, thus an artificial increase in the value of T_m.[179,181,185] Thermal lag can also result in artificially higher values of enthalpy and crystallinity due to the smearing of the peaks. This smearing of the peak can contribute to a significant increase in the T_m at high heating rate such as seen in Table 4.2 for the ASCM neat PHB sample. This 4 ˚C increase in the T_m can be attributed to this peak broadening that occurs. For the SC-EtOH neat PHB sample, the crystallinity remained constant around 13 % at heating rates between 150 ˚C/s to 300 ˚C/s. In a likewise manner, the enthalpy remained constant at approximately 19 J. These results indicated that a heating rate of 50 ˚C/s should be sufficient to prevent reorganization for the neat PHB sample, and at a heating rate of 300 ˚C/s, thermal lag was not occurring. For the SC-EtOH 0.5 wt. % CNC/PHB sample, the enthalpy and the crystallinity decreased as the heating rate was increased from 50 ˚C/s to 150˚ C/s. At heating rates between 150 ˚C/s to 300 ˚C/s the enthalpy and the crystallinity were relatively constant. Similar behavior was also observed for the SC-EtOH 1.0 wt. % CNC/PHB sample. These results indicated that for the SC-EtOH 0.5 wt. % CNC sample and the SC-EtOH 1.0 wt. % CNC/PHB samples, heating rates of at least 150 ˚C/s were needed to prevent

reorganization, and thermal lag was not occurring at heating rates between 150-300 ˚C/s. For the ASCM sample, a slightly different trend was observed. The calculated enthalpy and crystallinity remained relatively constant upon heating at rates between 50 ˚C/s to 200 ˚C/s but increased as the heating rate was increased to 300 ˚C/s, there was a 4 ˚C increase in the T_m of the neat PHB sample. This result indicated that at a heating rate of 300 ˚C/s, thermal gradients were present within the ASCM neat PHB sample. Therefore, crystallinity and enthalpy values calculated from melting peaks observed at heating rate of 300 ˚C/s for the ASCM samples would contain artifacts from the thermal gradients in the samples. In a similar manner, the calculated enthalpy of the ASCM 0.5 wt.% CNC/PHB sample and the ASCM 1.0 wt. % CNC/PHB sample have increased by 2-3 J/g indicating that smearing of the peak occur at these heating rates. Therefore in the next series of experiments, if a heating rate of 300 ˚C/s was used, the results from the ASCM samples will not be discussed.

Also, in order to compare the effect of CNC addition for the two different samples, the data obtained at a heating rate of 200 °C/s will be used for both samples. The overall crystallinity of the ASCM sample was greater than the crystallinity of the SC-EtOH sample. These results were expected and consistent with the results obtained in Chapter 3. For the ASCM and SC-EtOH samples, the addition of CNCs significantly increased the amount of crystallinity developed upon cooling. These results were expected because according to previous literature, CNCs acted as a strong nucleating agent for PHBV during nonisothermal crystallization, and the crystallization during cooling was the fastest for the sample with the greatest amount of CNCs.[91]

4.4 **Results from VC-CH experiments**

4.4.1 SC-EtOH samples

Figure 4.5 shows the melting curves of neat PHB, 0.5 wt. % CNC/PHB, and 1.0 wt. % CNC/PHB after cooling at several different rates ranging from 0.5 ˚C/s to 20 ˚C/s. From this figure, the effect of cooling on the development of crystallinity can be seen; the melting peak of the neat PHB sample did not shift toward higher temperatures as the cooling rate was decreased from 1 ˚C/s to 0.5 ˚C/s as seen for the samples with CNC added. At a cooling rate of 1.5 ˚C/s, differences in the melting peak of the neat PHB, 0.5 wt. % CNC/PHB sample and the 1.0 wt. % CNC/PHB sample were seen. There were small melting peaks for the neat and 0.5 wt. % CNC/PHB sample, whereas the melting peak of the 1.0 wt. % CNC/PHB was larger. These results indicated that the most crystallinity was developed in the 1.0 wt. % CNC/PHB sample at a cooling rate of 1.5 ˚C/s. These results were consistent with the experiment performed using conventional DSC and supported the hypothesis that CNCs acted as nucleating agents for PHB. As the cooling rate was increased from 1.5 ˚C/s to 5 ˚C/s, the melting peaks for neat PHB and 0.5 wt. % CNC/PHB became indistinguishable from the baseline, suggesting that no crystallinity developed. However for the 1.0 wt. % CNC/PHB at cooling rates of 8 ˚C/s, melting peaks were still observed. These results suggested that crystallization was still developing in the 1.0 wt. % CNC/PHB sample cooled at a rate of 8 ˚C/s.

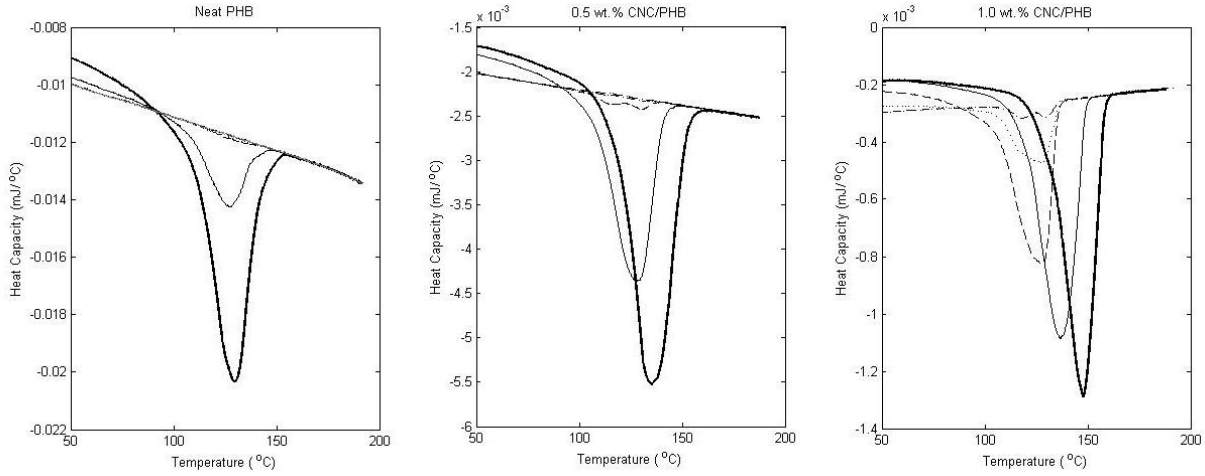

Figure 4.5. Comparison of melting peaks of SC-EtOH Neat PHB, 0.5 wt.% CNC/PHB, and 1.0 wt.% CNC/PHB at 0.5 ˚C/s (bold), 1 ˚C/s (line) , 3 ˚C/s (dash), 5 ˚C/s (dot), and 8 ˚C/s (dot-dash).

Table 4.3 shows the values for the T_g, T_{on}, T_m, enthalpy and crystallinity obtained from VC-CH experiments performed on the SC-EtOH samples. As the cooling rate was increased, the T_g shifted to lower temperatures. Another trend that was observed as the cooling rate was increased was the decrease in T_{on} and $T_{m.}$. This behavior was consistent with what was expected because less stable crystallites form at faster cooling rates, therefore the melting temperatures of these less stable crystallites were expected to be lower than the melting temperatures of larger, more perfect spherulites.

The most crystallinity developed in the 0.5 wt. % CNC/PHB at the slowest cooling rate of 0.5˚C/s (30 ˚C/min), whereas the neat sample had the least amount of crystallinity. The reason for this increased crystallinity of the 0.5 wt. % CNC/PHB sample could be attributed to the kinetics of crystallization, and the differences can be seen in the shape of the melting peak (see Figure 4.5). The melting peak of the 0.5 wt. % CNC/PHB sample at 0.5 ˚C/s was much broader than the 1.0 wt. % CNC/PHB sample, and T_{on} and T_m of the 1.0 wt. % CNC/PHB sample occurred at a higher temperature than the 0.5wt. % CNC/PHB sample. The narrower melting peak of the 1.0 wt. % CNC/PHB

suggested that size distribution of the lamellae within the 1.0 wt. % CNC/PHB sample was smaller than that of the 0.5 wt. % CNC/PHB sample, and the higher T_{on} and T_m of the 1.0 wt. % CNC/PHB sample suggested that crystallites formed in the 1.0 wt. % CNC/PHB required more energy to melt than the crystallites formed in the 0.5 wt. % CNC/PHB sample.

At cooling rates greater than 1 ˚C/s, the crystallinity of the 1.0 wt. % CNC/PHB sample was greater than that of the 0.5 wt. % CNC/PHB. These results were consistent with the results from the VH-CC experiments, in which the 1.0 wt. % CNC/PHB sample developed the most crystallinity upon cooling.

Table 4.3. Summary of the T_g, T_{on}, T_m, enthaply, and crystallinity as a function of cooling rate for SC-EtOH neat PHB, 0.5 wt.% CNC/PHB, and 1.0 wt% CNC/PHB.

Cooling Rate		**0.5**	**1**	**1.5**	**5**	**8**
Neat	T_g(˚C)	26.9	24.3	21.7	14.4	
	T_{on}(˚C)	110.3	108.1	100.9		
	T_m(˚C)	130.4	126.7	128.1		
	Enthalpy (J/g)	42.4	26.8	1.0	0.2	
	Crystallinity	29.0%	18.3%	0.7%	0.2%	
0.5 wt.% CNC/PHB	T_g(˚C)	26.3	23.8	22.2	21.9	
	T_{on}(˚C)	115.4	123.1	103.0	103.3	
	T_m(˚C)	135.2	128.5	115.0	110.3	
				130.5	130.8	
	Enthalpy (J/g)	98.1	64.5	3.6	0.4	
	Crystallinity	67.2%	44.2%	2.4%	0.3%	
1.0 wt.% CNC/PHB	T_g(˚C)	21.9	23.4	20.6	18.8	19.0
	T_{on}(˚C)	128.7	118.5	107.0	107.7	107.5
	T_m(˚C)	148.0	136.8	127.6	128.6	118.0
						129.2
	Enthalpy (J/g)	86.2	76.0	71.4	20.6	6.0
	Crystallinity	59.0%	52.1%	48.9%	14.1%	4.1%

4.4.1.1 Discussion of the VH-CC results

In the VC-CH experiments, the effect of cooling rate on the development of the crystallinity with and without nanoparticles was examined. The experiments are designed to be similar to a series of non-isothermal crystallization experiments performed in succession. Typically in nonisothermal crystallization experiments, analysis of the crystallization peak upon cooling is used describe the kinetics of nonisothermal crystallization at various heating rates. Since PHB is not a fast crystallizer, the crystallization upon cooling was not distinguishable. Therefore, the nature of the melting peaks upon heating were used to describe the crystallization developed during cooling. From the VH-CC experiments, a heating rate of 150 ˚C/s was needed to suppress reorganization upon heating. Therefore at a heating rate of 300 ˚C/s, only the melting behavior of the nonreorganized structure should be examined upon heating. From literature results, a cooling rate of 200 ˚C/min (3.33 ˚C/s) is needed to completely suppress the crystallization of PHB,[85,186] producing a completely amorphous sample. Therefore at cooling rates greater than ~3.3 ˚C/s, it is expected that very little crystallinity developed.

As the cooling rate was increased, a shift in the T_g to lower temperatures was observed. This shift in T_g to lower temperatures was an indication that the molecular mobility of the amorphous phase was increased[130,187,188] as the cooling rate was increased. This result was consistent with what was expected. As the cooling rate was increased, there was less crystallinity, and vitrification of the RAF occurred during isothermal crystallization rather than during cooling.[87] Therefore, the mobility of the amorphous component should be great at higher cooling rates. For all samples, there was a decrease in T_{on} and T_m as the cooling rate was increased. This decrease in the T_{on} and T_m as the cooling rate was increased indicated that size and stability of the crystalline component was decreased as the cooling rate was decreased. For the SC–EtOH samples, adding

CNCs into the matrix increased T_{on} and T_m while T_g either remained the similar to that of the neat PHB sample or was lower. These results suggested that CNC/PHB samples produced crystallites that were more stable than the neat PHB

As CNCs were added, there was an increase in the crystallinity. These results were consistent with the results obtained from the VH-CC results and the conventional DSC results described in Chapter 3. The CNCs acted as nucleating agents, which caused nucleation upon cooling to occur at higher temperatures. Therefore, the sample with a greater amount of CNCs had a faster crystallization rate, and with higher CNC loading, it was expected that more crystallinity developed upon cooling. At the higher cooling rates, more crystallinity was developed in the CNC/PHB samples, with the most amount of crystallinity developed in the 1.0 wt. % CNC/PHB sample.

4.5 **Isothermal crystallization experiments**

4.5.1 IC-VH at 90 ˚C

Figure 4.6 shows melting peaks after the isothermal crystallization for the SC-EtOH neat PHB at different heating rates. Unlike the CC-VH experiments, no cold crystallization peaks were observed in the IC-VH experiments. Table 4.4 gives the values of T_m, T_{on}, enthalpy, and crystallinity values obtained for the IC-VH experiments. At heating rates greater than 100 ˚C/s the value of T_{on} for the ASCM sample began to increase; however for the SC sample, T_{on} remained relatively constant.

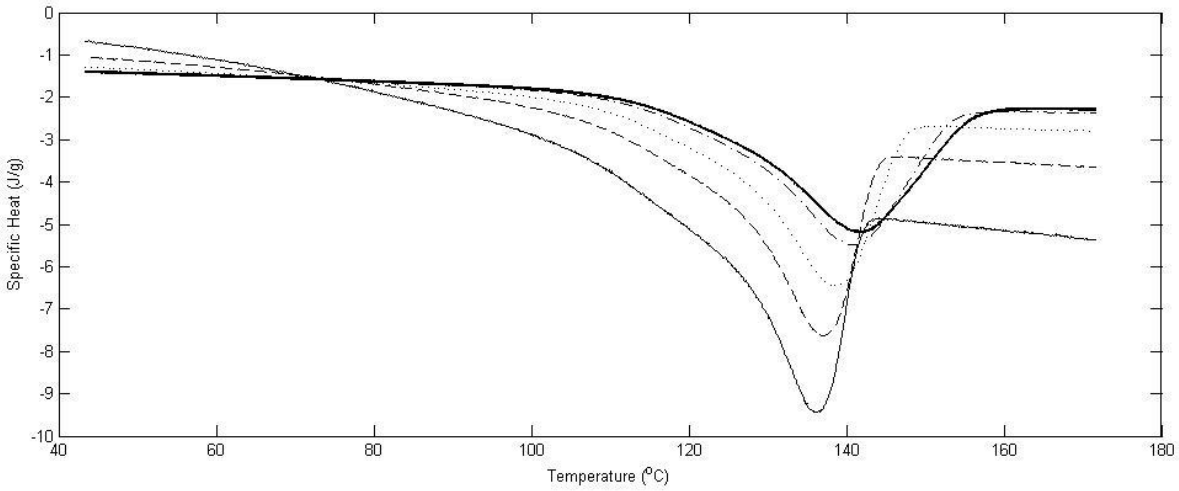

Figure 4.6. Melting curves from the IC-VH experiment for the SC-EtOH neat PHB sample at heating rate of 50 ˚C/s (solid), 100 ˚C/s (dash) 200 ˚C/s (dot) 400 ˚C/s (dot-dash), 500 ˚C/s (bold).

Table 4.4. Summary of the T_m, T_{on}, Enthalpy, and Crystallinity of the ASCM and SC-EtOH neat PHB samples

Heating Rate (˚C/s)		**5**	**10**	**50**	**100**	**200**	**400**	**500**
ASCM	T_m (˚C)	137.7	138.8	135.3	141.2	141.1	146.2	153.9
	T_{on}(˚C)	103.5	102.1	107.2	107.2	115.7	115.2	120.5
	Enthalpy (J/g)	75.8	66.7	63.2	63.5	63	60.5	58.6
	Crystallinity	51.9%	45.7%	43.3%	43.5%	43.2%	41.5%	40.1%
SC-EtOH	T_m(˚C)	142.5	139	136.1	136.7	136.2	137.2	140.4
	T_{on}(˚C)	136.2	134.6	127.6	129.9	130.3	130.5	130.5
	Enthalpy (J/g)	46.8	42.2	57.5	64.8	67.9	58.1	57.6
	Crystallinity	32.0%	28.9%	39.3%	44.4%	46.5%	39.8%	39.5%

4.5.1.1 Discussion of the IC-VH results

The objective of the IC-VH experiments was to determine if superheating would occur in the samples at long isothermal hold times due to the high heating rate. Superheating refers to the increase in the onset melting temperature with increasing heating rate.[181] Superheating depends the crystallization conditions, specifically the time

and temperature at which the sample was crystallized, and the effect of superheating increases as the annealing (or isothermal crystallization) time increases.[181] Superheating occurs at fast heating rates because melting is a kinetic process and the enhanced stability of samples that have be isothermal crystallized at high temperatures for long times. Therefore in these IC-VH experiments, a long hold time at a crystallization temperature of 90 ˚C was used since this temperature corresponds to the maximum growth rate of PHB.[189,190] T_{on} can be influenced by superheating whereas T_m can be influenced by both superheating and the thermal lag.[181,185] Typically thermal lag manifests itself as a broadening of the peaks due to the thermal gradients that develop within the sample, which would cause a shift in T_m to higher temperatures Therefore, systematic shifts in T_{on} were used to determine if superheating was occurring and changes in T_m were used to determine if there was thermal lag within the system at particular heating rates.

At heating rates greater than 200 ˚C/s for the ASCM sample, the value of T_m began to increase. This increase in T_m was an indication that peak broadening was occurring at these rates, suggesting that if experiments were performed at heating rate greater than these, thermal gradients would exist within the samples. The effect of this thermal lag was consistent with the results obtained from the analysis of the thermal lag of the chip sensor. A thermal lag of a few degrees (˚C) was observed at heating rates on the order of 1000 ˚C/s, for samples that had a mass of a few μg.[179]

An increase in T_{on} was observed when the heating rate was increased from 50 ˚C/s to 100 ˚C/s and then an increase in both T_{on} and T_m when the heating rate was further increased from 200 ˚C/s to 400 ˚C/s. This result then indicated that at these heating rates the kinetics of melting were slower than the heating rate which meant that superheating was occurring within the ASCM sample.

At heating rates above that needed to suppress reorganization and up to 500 ˚C/s, T_{on} remained relatively constant as the heating rate was increased. These results indicated

that superheating was not occurring at these rates in the SC-EtOH sample. However when the heating rate was increased from 400 ˚C/s to 500 ˚C/s, there was a 3 ˚C increase in the T_m, which indicates that there was thermal lag within the sample at a heating rate of 500 ˚C/s. Therefore, the maximum heating rate that could be used with the samples would be approximately 50 ˚C/s for the ASCM sample and 400 ˚C/s for the SC-EtOH sample. The differences in the temperature needed to prevent superheating could be due to the difference in sample mass. The ASCM sample has a sample mass that is 4 times as big as the SC-EtOH sample.

4.5.2 Isothermal crystallization experiments

For the isothermal crystallization experiments, each sample was isothermally crystallized for 10s, 20s, 60s and 500s in order to monitor the development of crystallinity with time. Figure 4.7 shows the apparent heat capacity obtained from the heating step after the isothermal hold time. As expected, the area under the melting peak and the value of T_m increased with increasing isothermal crystallization hold time.

With regards to the shape of the heat capacity curves (shown in Figure 4.7), there was a shift in the baseline at temperatures between T_g and the melting point with increased crystallization, accompanied by a decrease in the magnitude of endothermic step at T_g. In Figure 4.8, the melting curves of neat PHB samples processed by the SC-EtOH method that have been partially crystallized at an isothermal temperature of 65 ˚C for times of 10s, 20s, 60s and 500s are shown. From this figure, the reduction of the glass transition step with increasing hold time and the presence of a second T_g associated with the enthalpy relaxation of the RAF was observed in the heat flow curve of the sample that has been isothermally crystallized for 60s.

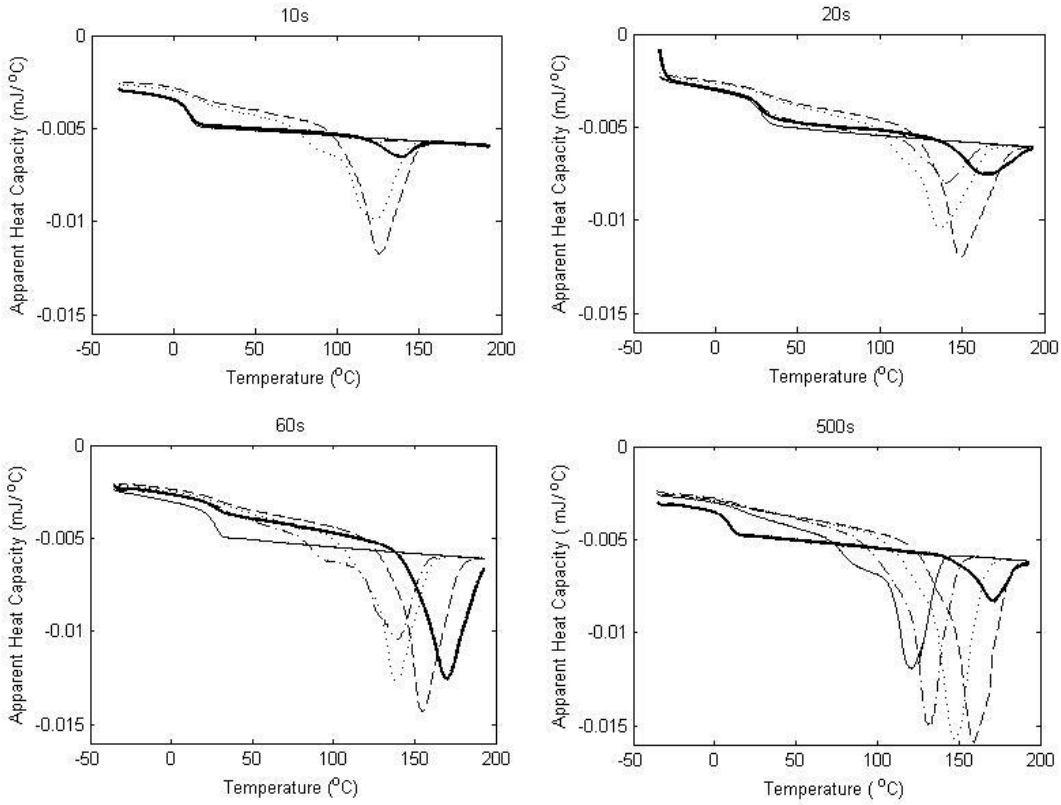

Figure 4.7. Apparent heat capacity curves for SC-EtOH neat PHB held for different isothermal times ranging from 10 to 500 s at 40 ˚C (solid) , 60 ˚C (dot-dash), 80 ˚C (dot) , 100 ˚C (dash), and 120 ˚C (bold).

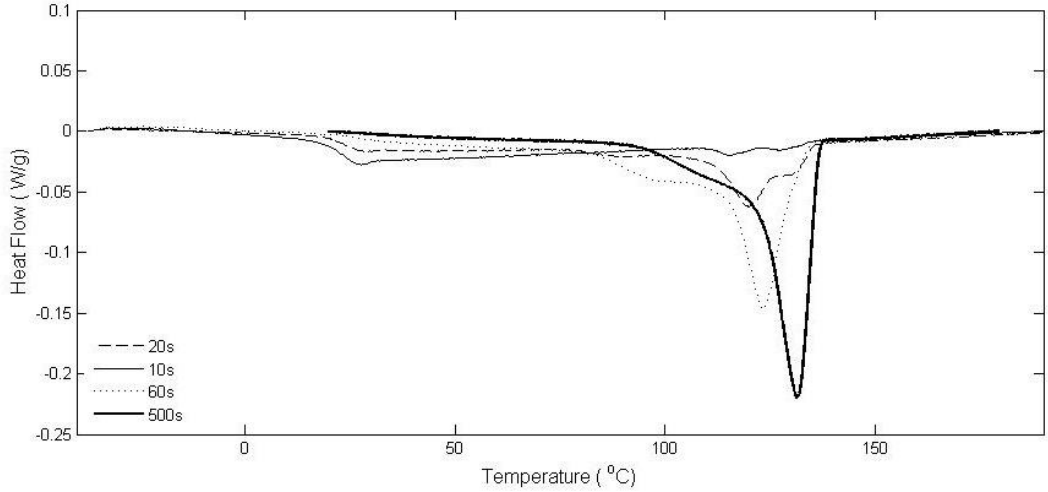

Figure 4.8. FDSC curves of the melting peak for SC-EtOH neat PHB crystallized at 65 °C for 10s (solid), 20s (dash), 60s (dot), and 500s (bold line).

The evolution of the crystallinity attained in the SC-EtOH neat PHB sample as a function of isothermal crystallization temperature at different isothermal hold times is shown in Figure 4.9. At isothermal crystallization temperatures close to T_g and close to T_m, the crystallinity values were lowest. The largest amount of crystallinity developed at temperatures approximately halfway between T_g and T_m, consistent with conventional DSC results.[125,191]

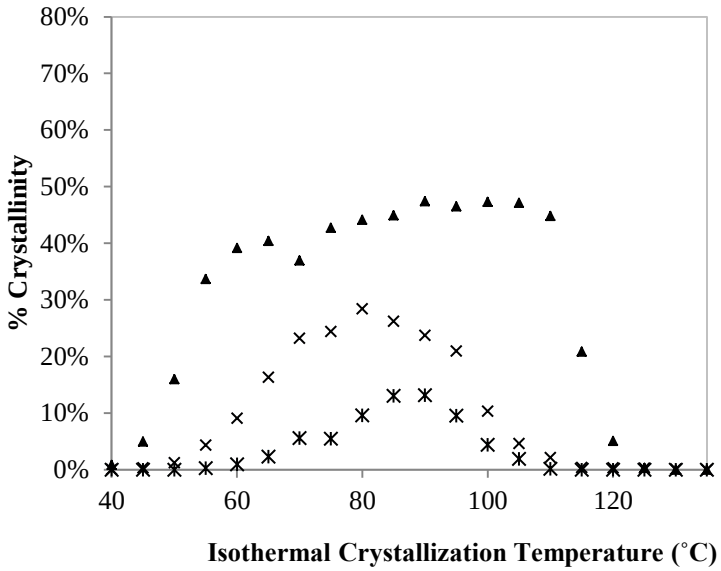

Figure 4.9. Evolution of the crystallinity of SC-EtOH neat PHB held for 10 seconds (star), 20 seconds (x), 60 seconds (triangle) and 500 seconds (diamond) as a function of isothermal crystallization temperature.

4.5.2.1 CNC/PHB SC-EtOH samples

Figure 4.10 shows Flash DSC curves for the 0.5 wt. % CNC/PHB sample for the isothermal crystallization experiments performed at different isothermal hold times. The melting peak behaviors of the SC-EtOH samples with nanoparticles were similar to the melting peak behavior of the SC-EtOH neat PHB sample from the isothermal

experiments. These melting peaks were used to calculate the amount of crystallinity developed during the isothermal step. At an isothermal crystallization temperature of 40 ˚C, no crystallinity developed upon heating at any of the isothermal hold times. As the isothermal crystallization temperature was increased to 80 ˚C, a melting peak was observed. As the isothermal crystallization temperature was further increased to 100 ˚C, the temperature at which T_m occurred increased. As the isothermal hold time was increased, the ΔH of melting increased, and T_m shifted to higher temperatures. Similar behavior was observed for melting curves associated with isothermal crystallization at 100 ˚C and 120 ˚C.

Figure 4.11 and Figure 4.12 shows how the MAF and crystallinity of the 0.5 wt. % CNC/PHB sample and 1.0 wt. % CNC/PHB sample changed at different isothermal hold times. In the figures, the MAF of the samples was plotted as well to show the change in the MAF as a function of the isothermal crystallization temperature. From these figures, the crystallinity of the sample increased as the isothermal crystallization time increased, and the MAF decreased as the isothermal hold time was increased. At the isothermal hold times of 10s and 20s, the crystallinity as a function of isothermal crystallization temperature exhibited a Gaussian peak. As the isothermal hold time was increased from 20s to 60s, the crystallinity as a function of isothermal crystallization temperature curve did not show the Gaussian peak observed in the 10s and 20s data. Instead at isothermal crystallization temperatures between 60 ˚C and 100 ˚C, the crystallinity remained relatively constant. As isothermal crystallization time was further increased to 500s, there was an increase in the crystallinity, and the range where the crystallinity was relatively constant increased to a temperature range of 50 ˚C to 100 ˚C.

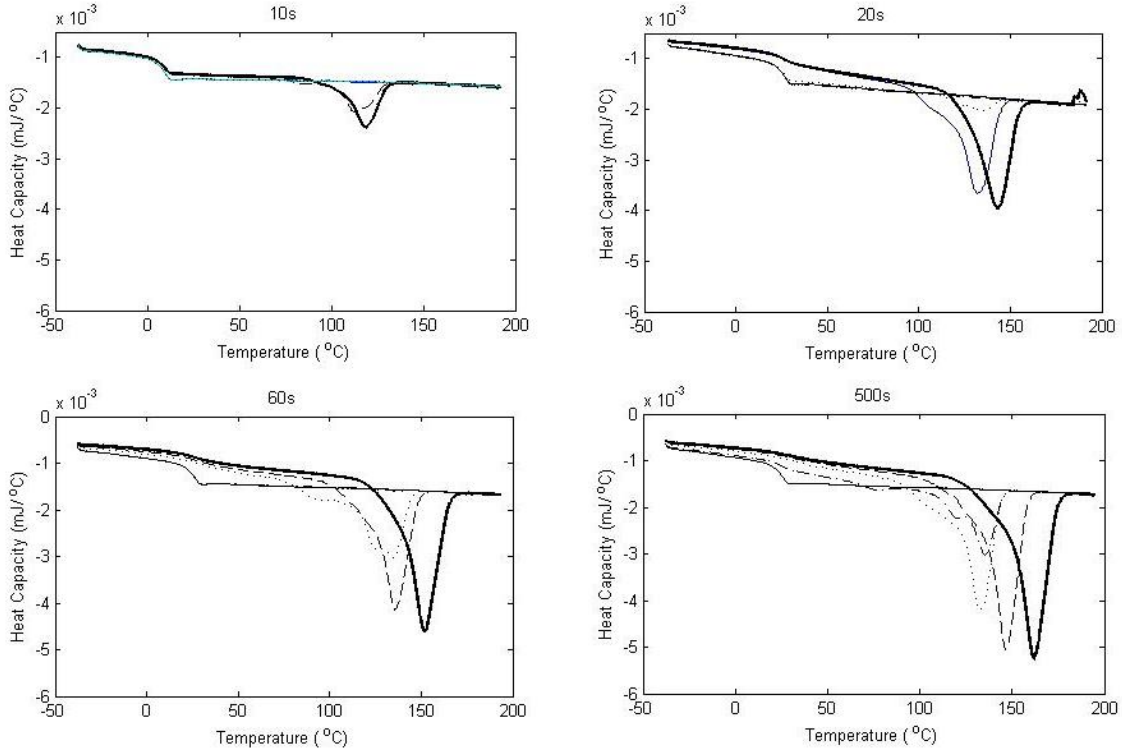

Figure 4.10. Flash DSC curves for SC-EtOH 0.5 wt.% CNC/PHB at isothermal crystallization temperatures of 40˚C (solid), 60˚C (dot-dash), 80˚C (dash), 100˚C (dot), and 120˚C (bold) at hold times between 10 and 500s

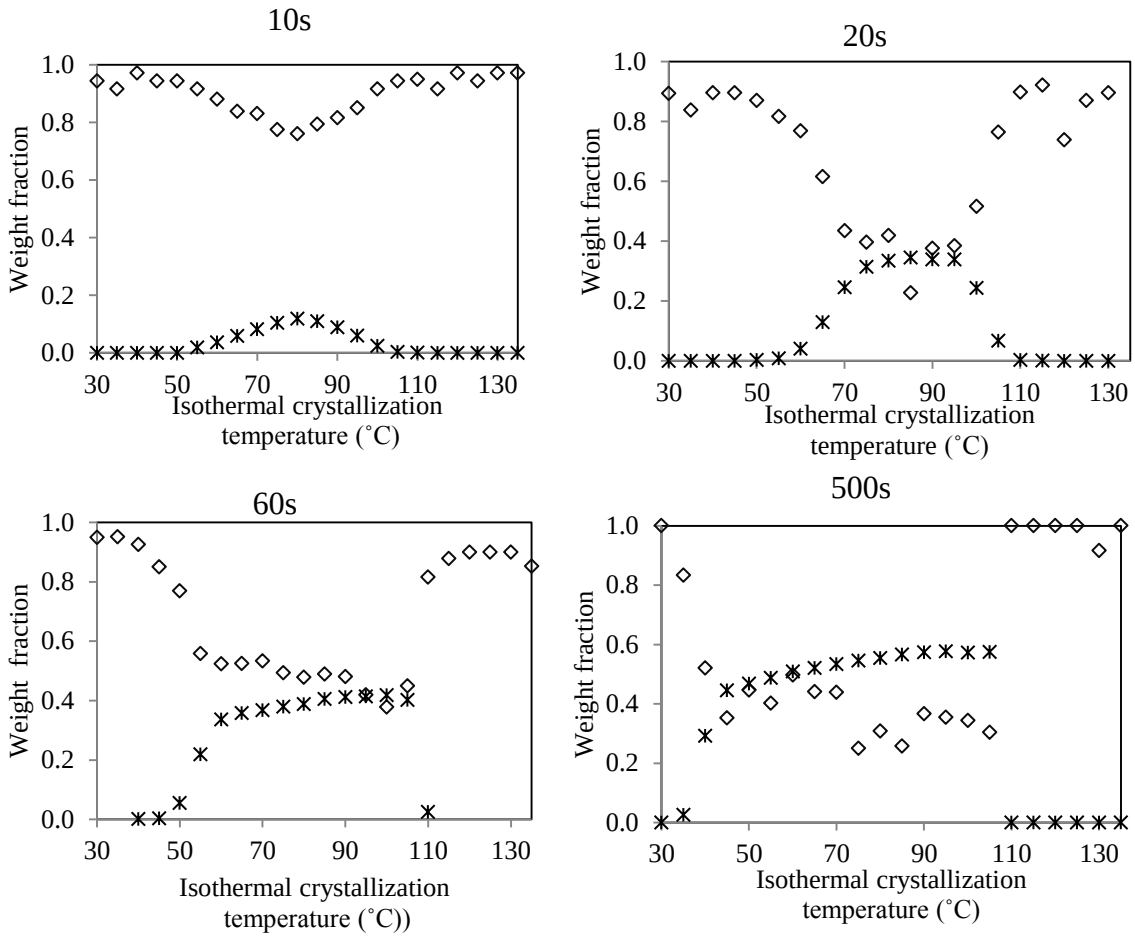

Figure 4.11. Development of the crystallinity (diamonds) and MAF (star) during isothermal crystallization of SC-EtOH 0.5 wt.% CNC/PHB for 10s, 20s , 60s, and 500s .

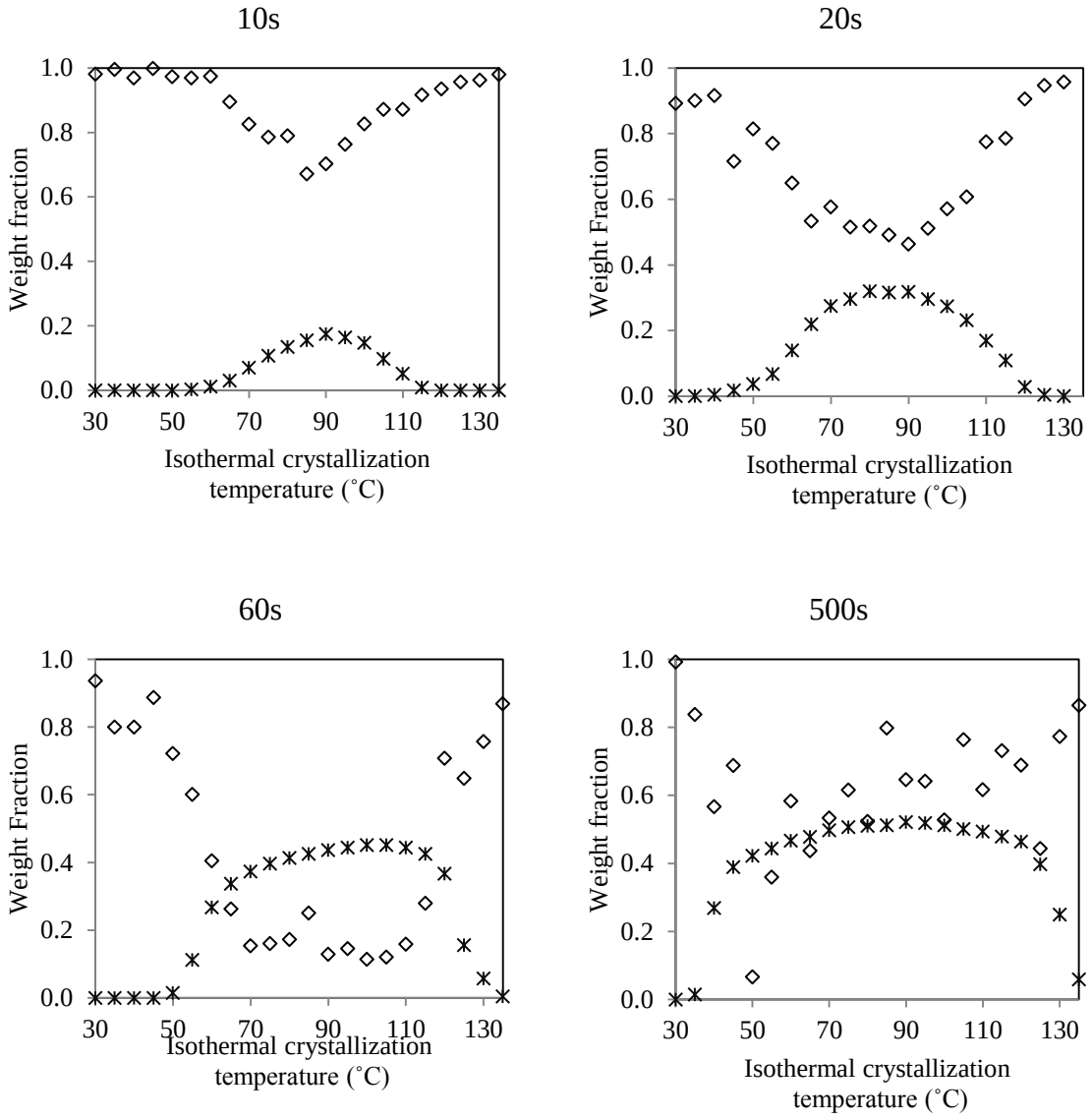

Figure 4.12. Development of crystallinity (diamonds) and MAF (star) during isothermal crystallization of SC- EtOH 1.0 wt. % CNC/PHB for 10s, 20s, 60 s and 500s.

4.5.2.2 Discussion of the results from isothermal crystallization

As the isothermal crystallization hold time increased, a decrease in the magnitude of T_g was seen, and the baseline became flatter. The decrease in the magnitude of T_g was due to the decreased amount of MAF as crystallization proceeded.[68] The shift in the baseline was due to the increased crystalline fraction, producing a shift in the heat capacity above T_g. These results were consistent with what was expected because as the isothermal hold time increased, more crystallinity was expected to develop.

A similar trend is seen in Figure 4.8, which shows the change in the melting curves as the isothermal hold time increases. From this figure, the reduction of the glass transition step with increasing hold time and the presence of a second T_g associated with the enthalpy relaxation of the RAF was observed in the heat flow curve of the sample that has been isothermally crystallized for 60s. This result was consistent with the work of Di Lorenzo et al. where the authors observed an enthaplic relaxation upon heating occurring at a temperature between 70 ˚C and the melting peak for PHB. They attributed this feature to the "enthalpy relaxation of the rigid amorphous structure".[192] It is expected that this enthalpy relaxation of the rigid amorphous structure should be reduced in nanocomposites where the interphase between the matrix and the filler is immobilized.[193] Differences in the RAF between the neat PHB and CNC loaded samples will be discussed in greater detail in the RAF section.

Figure 4.13 is a comparison of the crystallinity developed at an isothermal hold time of 10s and 60s for the neat PHB, 0.5 wt. % CNC/PHB and 1.0 wt. % CNC/PHB samples processed by the SC-EtOH method. At an isothermal hold time of 10s, the initial stages of primary crystallization were occurring where dominant lamellae grow unhindered and were well separated from one another.[194] Therefore, the crystallinity developed can be considered analogous to the crystallization rate. The classical description of the temperature dependence of the rate of crystallization (shown in Figure

4.14) and the mechanisms that limit the rate of crystallization were used to describe the nucleating effect of nanocrystals on the PHB in the SC-EtOH sample. From the previous chapter, the addition of CNCs increased the rate constant *k,* which effectively shifted the temperature dependence of the nucleation rate to higher temperatures, increasing the temperature corresponding to the maximum rate of crystallization and increasing the amount of crystallinity developed. This shift in the nucleation controlled regime as CNCs were added into PHB can be clearly seen in Figure 4.13 for the SC-EtOH samples.

The increase in the nucleation controlled regime can still be seen in the development of crystallinity at an isothermal hold time at 60s, which is shown in Figure 4.13 However, a different trend was observed for the crystallinity developed at temperatures between 60 ˚C and 110 ˚C. Rather than exhibiting a Gaussian curve within this temperature range, the crystallinity increased slightly with time. These results suggested that at 60s impingement of spherulites occurred for the samples isothermally crystallized within this temperature range.

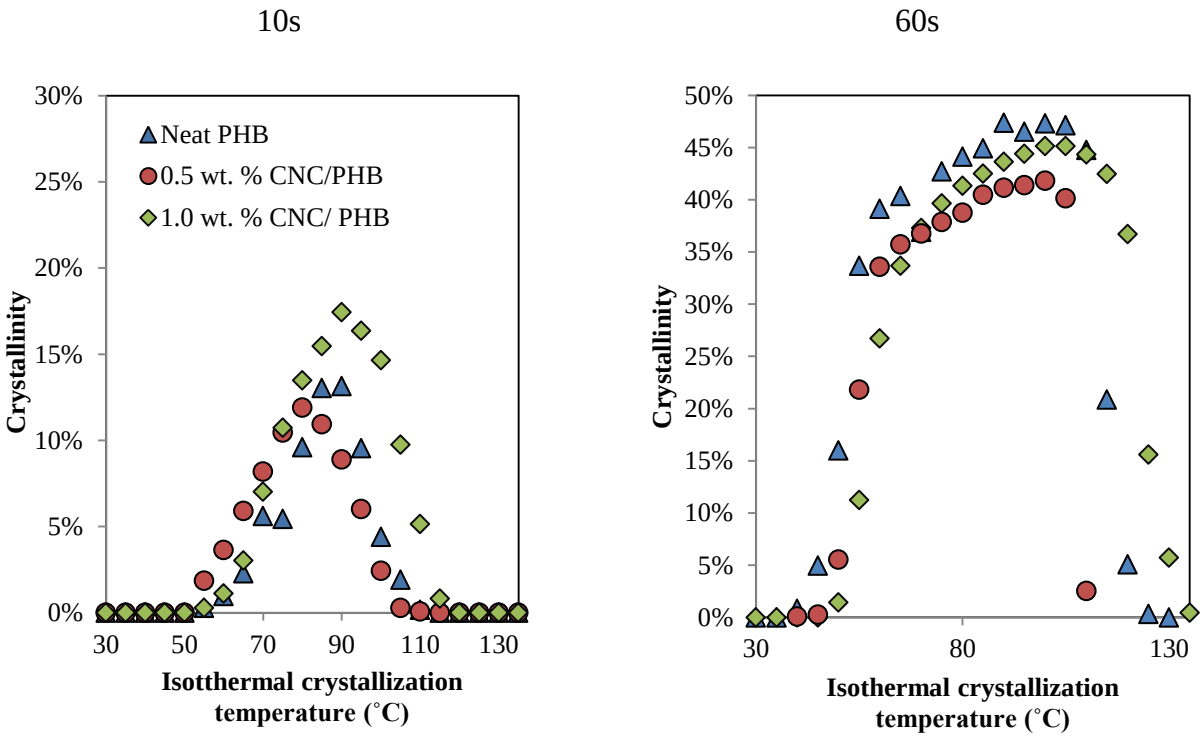

Figure 4.13. Comparison of the crystallinity developed in the SC-EtOH samples after a 10s (left) and 60s (right) isothermal hold.

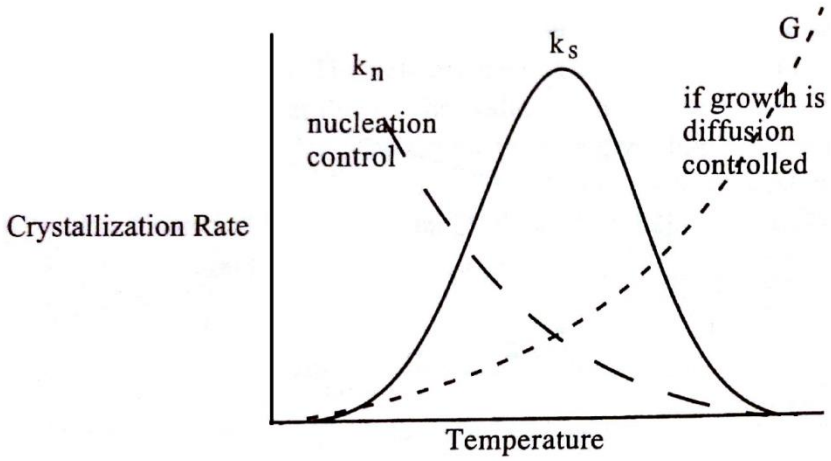

Figure 4.14. Diagram showing the trends in crystallization rate due to the competing nucleation and growth controlled processes

At a longer isothermal hold time of 500s, the neat PHB sample developed the most crystallinity, and the 1.0 wt. % CNC/PHB developed the least amount of crystallinity overall. In certain systems, the interphase region forms as an amorphous region that interferes with crystal growth, which can limit the overall crystallinity of the system.[195,196] Also, the difference in the amount of crystallinity developed could be due to the increased nucleation density of CNC loaded samples. From the results from the isothermal crystallization experiments described in Chapter 3, the size of the spherulites within the CNC/PHB samples was significantly smaller than that of the neat PHB samples. These results indicated that the area where spherulites impinge upon one another would be greater in CNC/PHB samples than in neat PHB samples, contributing to the decrease in the overall crystallinity of the sample due to an altered spherulite growth front. After impingement, the primary lamellae continue to grow, but now are required to form in the free spaces,[197] thus reducing the amount of crystallinity relative to amorphous content in the areas where impingement occurs.

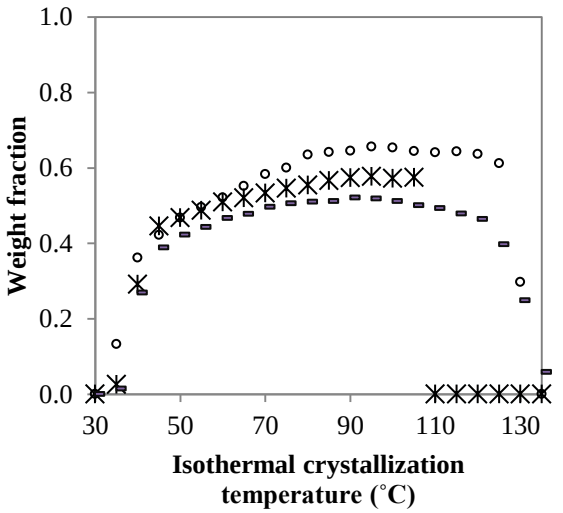

Figure 4.15. Crystallinity of the neat PHB (circles), 0.5 wt. % CNC/PHB (star) and 1.0 wt. % CNC/PHB (dash) at an isothermal hold time of 500 s for SC-EtOH (left).

In all samples, there was an increase T_m as the isothermal crystallization temperature was increased. This behavior was expected from the results of previous isothermal crystallization studies performed on PHB. As isothermal crystallization temperature increases, the thickness of the lamellae should increase, resulting in an increased melting temperature.[191] In Figure 4.16, T_m was plotted as a function of the isothermal crystallization temperature for the different isothermal hold times, and Table 4.5 shows the slope, intercept and R^2 value of the linear regression performed on the T_m as a function isothermal crystallization temperature. At isothermal hold times between 10 and 60s, the slope of T_m vs. the isothermal crystallization temperature increased due to the development of lamellae. As more lamellae developed, the observed T_m increased. However at 500s, the slope decreased. This change in the slope can be attributed to the change in the growth mechanisms that occurred after impingement. Wurm et al. have shown that for semicrystalline polymers that do not undergo lamellar thickening during isothermal crystallization a "stabilization" process occurs during isothermal crystallization.[198] This stabilization effect was observed in PHB, and the authors observed this stabilization effect to occur only after isothermal hold times that correspond with the onset of impingement.[185] The authors also attributed the decrease in the development of crystallinity at long isothermal hold times to the presence of a vitrified amorphous phase coupled with the crystalline regions hindering the further development of the crystalline component.[185]

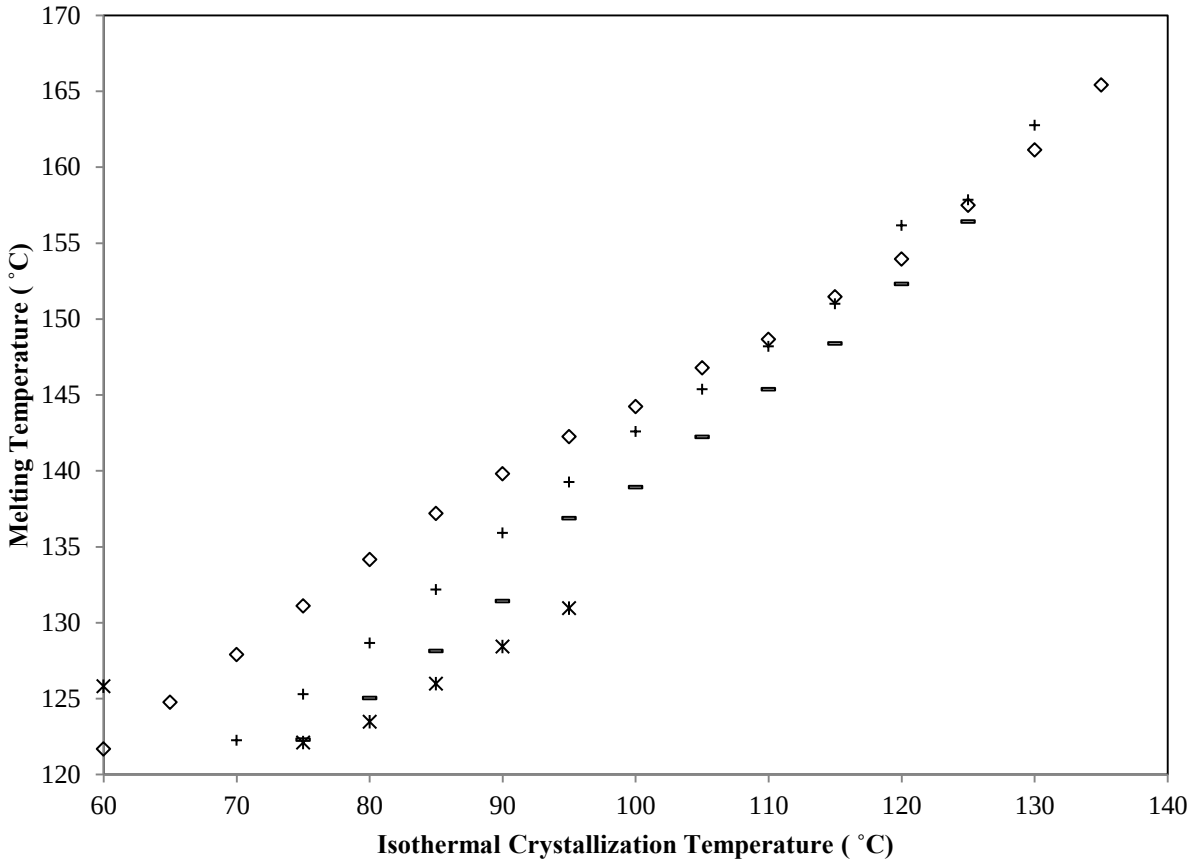

Figure 4.16. Melting temperature plotted as a function of isothermal crystallization temperature for the SC-EtOH 1.0 wt. % CNC/PHB at 10s (star), 20s (dash) 60s (cross) and 500s (diamond).

Table 4.5. Linear regression of the melting temperature as a function of isothermal crystallization temperature

Isothermal hold	Neat PHB			1.0 wt. %CNC/PHB		
	Slope	Intercept	R^2	Slope	Intercept	R^2
10 s	0.43	89.46	99.4%	0.45	87.64	99.2%
20s	0.51	85.48	92.5%	0.56	83.64	99.7%
60 s	0.71	76.15	99.3%	0.68	75.93	99.7%
500s	0.64	91.22	99.2%	0.61	85.15	99.9%

4.5.2.3 Rigid Amorphous Fraction.

For semicrystalline polymer systems, there is a relationship between the RAF and the crystallinity. Figure 4.17 shows the relationship between RAF and crystallinity in different polymer systems as well as the role of the RAF in the development of crystallinity. Also this figure shows the region in which the evolution of the semicrystalline structure that has not yet been studied, which is the range in which incomplete primary crystallization occurs.[188] In this section, a discussion of the role of the RAF in the initial stages of primary crystallization will be discussed for SC-EtOH samples and ASCM samples. Also the formation and evolution of the RAF within PHB with increased isothermal hold time is important because the RAF has been associated with increase in the crystallinity when stored at room temperature,[85,132] and several authors have suggested that RAF plays a role in the embrittlement of PHB.[182,187,199] Annealing treatments have improved the resistance of PHB to embrittlement[134] and authors have attributed the enhancement due to the reduction of RAF during the annealing process. Therefore, it is important to understand how the RAF evolves with increased isothermal hold time because this information could provide insight into methods to prevent the embrittlment of PHB.

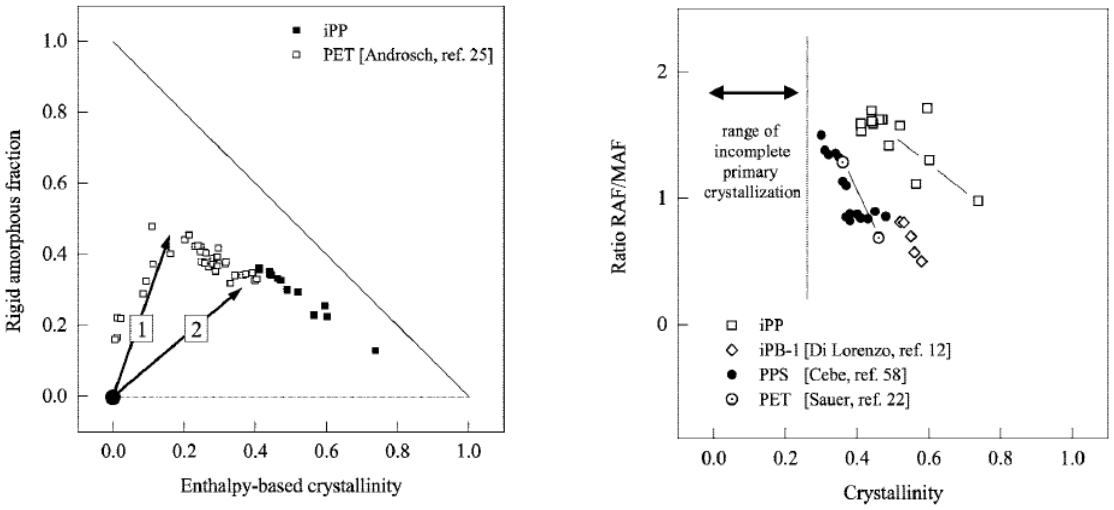

Figure 4.17. RAF as a function of enthalpy based crystallinity (left) and ratio of RAF/MAF as a function of crystallinity.[188]

4.5.2.3.1 Neat PHB

Figure 4.18 describes how the RAF, MAF and crystallinity changes with isothermal crystallization temperature for a sample crystallized at each isothermal temperature for 20 s. The RAF was calculated using the equation below:

$$RAF = 1 - MAF - CF$$

The general technique is described in the application notes for the HyperDSC[200]. The MAF was calculated as the ratio of the observed change in heat capacity at T_g (ΔC_P) and the heat capacity at T_g for a completely amorphous sample ($\Delta C_{P,amorphous}$)

$$MAF = \frac{\Delta C_P}{\Delta C_{P,amorphous}}$$

At isothermal crystallization temperatures close to the glass transition, the amount of MAF was greatest, and the crystallinity was lowest. This result was expected because at temperatures near the glass transition temperature, the diffusion of the polymer chains was the rate limiting step for crystallization to occur. At temperatures near the melting temperature, the crystallinity was also relatively low. This result was also expected because at temperatures near the melting temperature, even though diffusion of the polymer chains was fast, the energy required for nucleation to occur was large.

At isothermal crystallization temperatures below the temperature at which the RAF devitrifies, the enthaplic relaxation associated with the mobilization of the RAF was clearly seen in Figure 4.19. Table 4.6 shows the calculated values obtained for the T_{RAF}, T_{on} and T_m for the ASCM sample. The T_{RAF} of the SC-EtOH sample increased as the isothermal crystallization temperature increased, indicating that the RAF became more thermodynamically stable. These results suggested that at isothermal crystallization temperatures close to the temperature at which devitrification of the RAF occurred, the RAF was coupled with the crystalline phase. This result was further supported by the fact that the melting curves associated with isothermal crystallization temperatures just above the devitrification of the RAF (~70 ˚C), the enthaplic relaxation behavior associated with the RAF and the onset of melting peak became almost indistinguishable from one another.

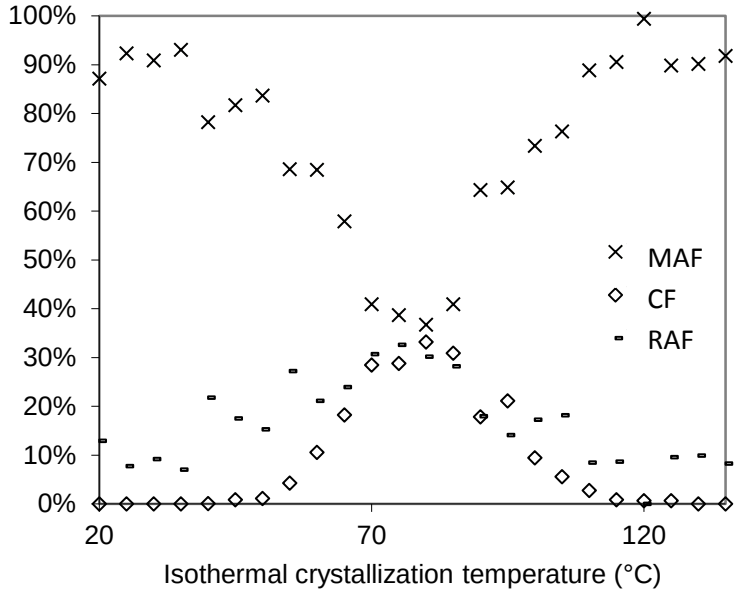

Figure 4.18. Composition of SC-EtOH Neat PHB at different isothermal crystallization temperatures.

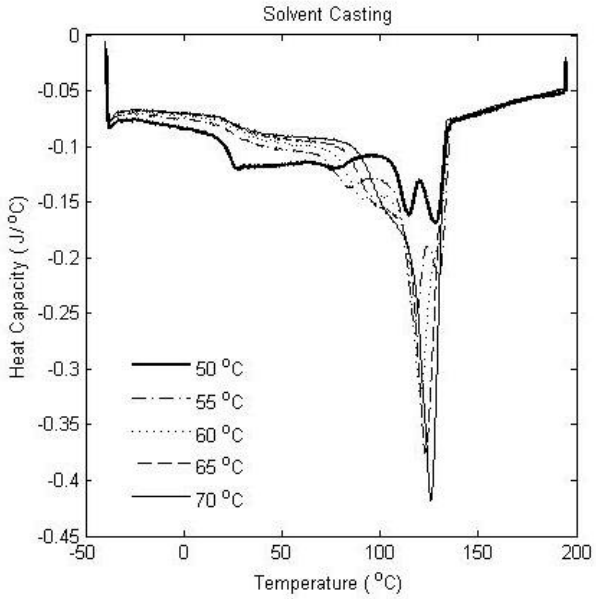

Figure 4.19. Melting peaks after the isothermal crystallization for neat PHB at for an isothermal hold time of 60s.

Table 4.6. Summary of the T_{RAF}, T_{on} and T_m of the ASCM and SC sample isothermally crystallized for 60s at temperatures from 50-70˚ C.

Isothermal Crystallization	SC-EtOH		
	T_{RAF}	T_{on}	T_m

Temperature (˚C)	(˚C)	(˚C)	(˚C)
70	88.5	117.1	125.9
65	82.8	114.6	123.1
60	76.9	111.7	120.6
55	71.6	108.8	117.6
50	66.9	105.9	114.7

The enthaplic relaxation associated with the mobilization of the RAF was observed for the SC-EtOH samples and is shown in Figure 4.20. Table 4.7 shows the calculated values obtained for the T_{RAF}, T_{on} and T_m for the different SC-EtOH samples. As with the neat PHB, the T_{RAF} of all of the SC-EtOH composite samples increased as the isothermal crystallization temperature increased, indicating that as the isothermal crystallization temperature was increased, the RAF became more thermodynamically stable in these samples as well. Also as the nanoparticle loading was increased, the T_{RAF} increased. These results suggested that the presence of nanoparticles increased the temperature at which the mobilization of the RAF occurred. This result could be due to more coupling occurring between the RAF and the crystalline component of PHB or to the interphase of the composite produced by interactions between the nanoparticle and the matrix. However, the interphase that is typically formed when the matrix and nanoparticle interact favorably has a enthaplic relaxation that occurs at temperatures above the melting temperature of the polymer matrix.[193]

To determine the effect of nanoparticle addition on the initial formation of the RAF, Figure 4.21 shows the RAF as a function of isothermal crystallization temperature for the SC-EtOH samples. There are no significant differences in the behavior of RAF formed as a function of isothermal crystallization temperature for the neat PHB, 0.5 wt. % CNC/PHB, and 1.0 wt. % CNC/PHB samples. This result indicated that for the SC-EtOH sample, the addition of CNC did not affect the amount of RAF initially formed.

The evolution of the RAF with isothermal hold time is shown in Figure 4.22 and Figure 4.23 for neat PHB and 1.0 wt. % CNC/PHB respectively. For both the neat PHB system and the 1.0 wt. % CNC system, at isothermal hold times of 10s ,20s, and 60s, the RAF increased. At 500s, the amount of the RAF decreased when compared with the 60s and 20s.

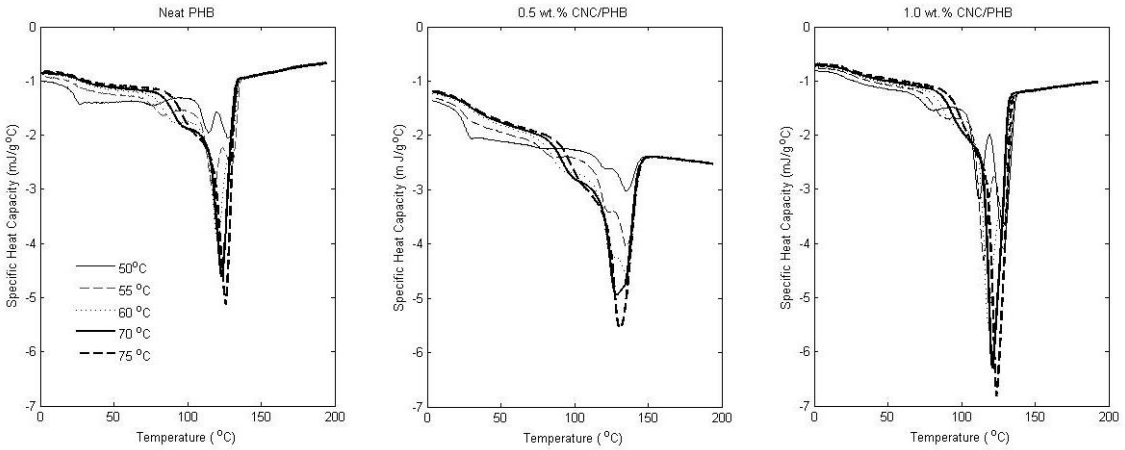

Figure 4.20. Melting peaks after the isothermal crystallization at 50˚C, 55˚C, 60˚C, 65˚C, 70˚C and 75˚C for the solvent cast samples.

Table 4.7. Comparison of the T_{RAF}, T_{on} and T_m for SC-EtOH samples with different nanoparticle loadings at an isothermal hold time of 60 s.

		70 (˚C)	65 (˚C)	60 (˚C)	55 (˚C)	50 (˚C)
Neat PHB	T_{RAF} (˚C)	88.5	82.8	76.9	71.6	66.9
	T_{on} (˚C)	117.1	114.6	111.7	108.8	105.9
	T_m (˚C)	125.9	123.1	120.6	118.5	115.6
				130.3	129.9	128.0
0.5 wt.% CNC/PHB	T_{RAF} (˚C)	89.5	83.6	77.4	72.4	71.9
	T_{on} (˚C)	121.2	118.6	115.6	114.7	112.2
	T_m (˚C)	131.3	129.3	125.7	124.6	121.8
			134.0	135.4	135.3	135.2
1.0 wt.% CNC/PHB	T_{RAF} (˚C)	91.5	86.9	80.9	76.1	68.9
	T_{on} (˚C)	113.8	109.9	107.0	103.2	101.3
	T_m (˚C)	122.7	119.7	116.6	113.3	110.5
				129.2	129.2	128.4

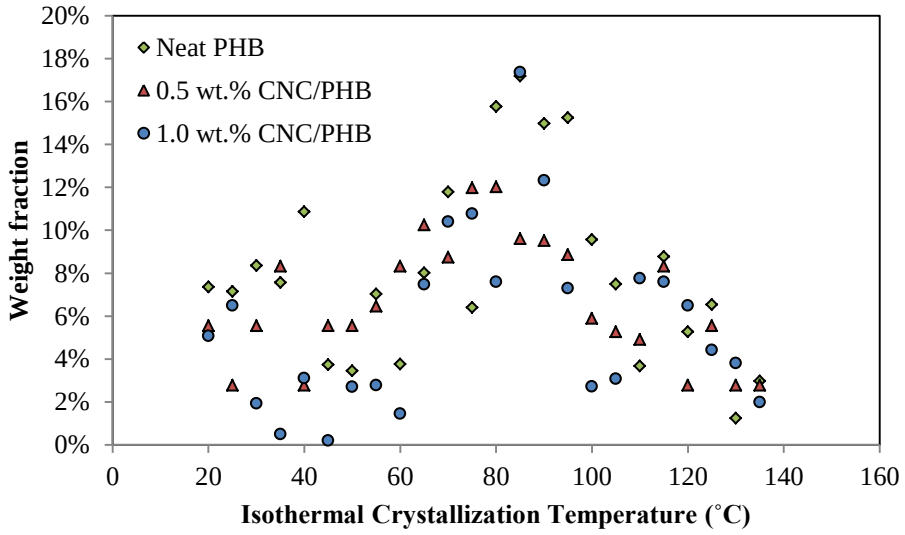

Figure 4.21. RAF as a function of isothermal crystallization temperature at 10s for SC-EtOH samples.

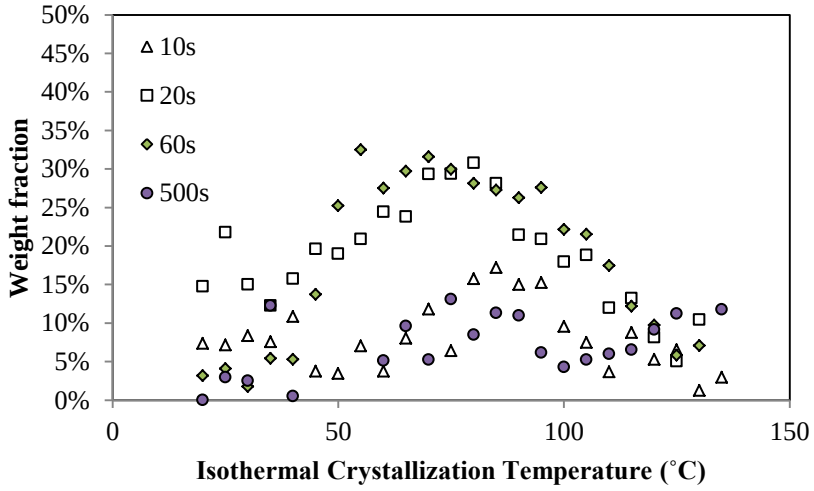

Figure 4.22. Evolution of the SC-EtOH neat PHB RAF with increasing isothermal hold time

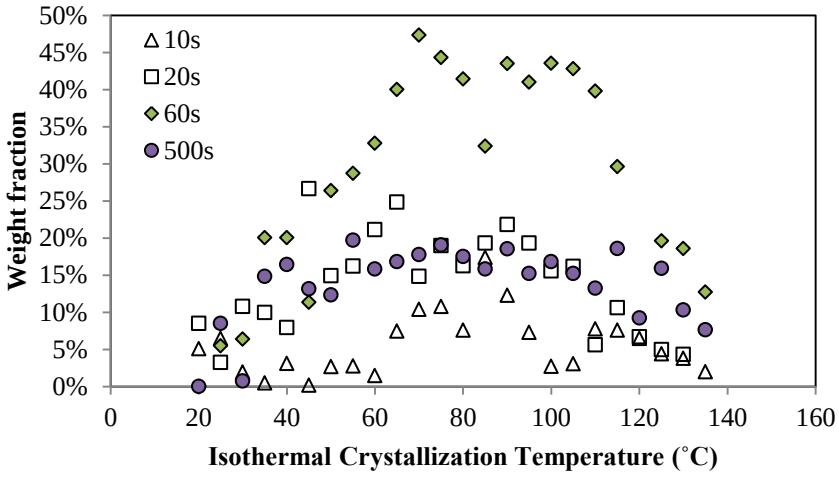

Figure 4.23. Evolution of the RAF of 1.0 wt. % CNC/PHB.

4.5.2.4 Discussion

Since the amount of RAF is associated with the initial stage of crystallinity,[68,87,201] the increase in the RAF at the isothermal hold times of 10s, 20s. and 60s was consistent with the expected result. Previous research has shown the kinetics of vitrification of the RAF parallels crystal growth in PHB.[132,202] Therefore the amount of RAF present at the different isothermal hold times should provide information regarding the amount of crystalline phase that was developing after a particular hold time.

At 10s, the amount of RAF within the neat PHB , 0.5 wt. % CNC/PHB the 1.0 wt. % CNC/PHB samples were similar. These results suggested that the nature of the matrix-filler interaction in the SC-EtOH samples did not alter the kinetics of crystallization and growth of PHB after 10s.

After 10s, differences in the amount of RAF in the neat PHB samples, 0.5 wt. % CNC/PHB samples, and the 1.0 wt. % CNC/PHB sample were seen. In the neat PHB sample, the amount of RAF at an isothermal hold time of 20 and 60s was similar. These results indicated that the amount of crystalline phase that was developing at 20s was

similar to the amount that was developing at 60s, which suggested that at 20s and 60s, the crystallization rate was approximately constant and linear. This result was consistent with the results obtained from the hot stage microscopy which was described in Chapter 3. For the 0.5 wt. % CNC/PHB sample. and the 1.0 wt. % CNC/PHB sample, at 20s the amount of RAF was less than that of the neat PHB. After an isothermal hold time of 60s the amount of RAF in the 0.5 wt. % CNC/PHB sample and 1.0 wt. % CNC/PHB sample was significantly greater than that of neat PHB. These results suggested that the nucleating effect of CNC has an induction time, and that the introduction of CNC would slow down the development of crystallinity at very short isothermal hold times, but then drastically increased the amount of crystallinity developed.

The differences in the amount of RAF present at 20s and 60 between the neat PHB and the CNC loaded samples could also be attributed to differences in the dimensionality and type of crystal growth occurring in the two systems. Since there was no significant difference in the n obtained from the isothermal crystallization experiments performed using conventional DSC, the dimensionality and type of crystal growth in the neat PHB and the 1.0 wt. % CNC/PHB were expected to be similar. There was a decrease in the RAF at 500s in both systems, and this trend was expected because a reduction in the RAF at long isothermal hold times has been observed in other semicrystalline polymer systems as the crystallinity developed more fully. At high crystallinities, the linear relationship between the RAF and crystallinity breaks down and deviation from the linear relationship occurs in polymer system beginning at 40%.[188,203] Therefore the observed decrease in RAF at long isothermal hold times was expected. The decreasing in RAF at long isothermal hold times has been associated with the increase in crystal perfection in the crystalline regions, which decreases the strain transmitted to the amorphous segments and results in decreased RAF.[204] Overall, the amount of RAF in the 1.0 wt. % CNC/PHB system was the greatest at 500s when

compared with the 0.5 wt. % CNC/PHB and neat PHB samples. This increase in the RAF should influence the mechanical behavior of CNC/PHB composite and the aging behavior of the composite because several studies has described the role of the RAF in the evolution of the structure of PHB during storage in ambient conditions.[132,202] An increase in the RAF associated with the crystalline regions of PHB should decrease the tanδ, and increase the rate at which progressive crystallization occurs. However, since the increase in the RAF could be due to the fact that CNC-PHB interactions creating a RAF. This CNC-PHB RAF should be behave differently than the RAF associated with the crystalline region of PHB due to the fact that the CNC-PHB RAF should be more immobile than the RAF of PHB.

4.6 **Conclusions**

Using the Flash DSC, the effect of thermal processing on structural evolution of PHB has been studied for PHB processed in two different ways. Because of the increased sensitivity of the FDSC, the heating rates at which reorganization occurred in the neat PHB system and the heating rates that suppress the reorganization of PHB were obtained. Also, the FDSC has provided information regarding the evolution of melting behavior of PHB at large undercoolings, as well as how the crystallinity develops at short isothermal hold times. These initial findings on PHB provide valuable information regarding the how thermal treatment and processing can affect the development of the structure of a semicrystalline polymer.

In the VH-CC experiments, the effect of non-isothermal crystallization on the reorganization behavior of PHB was studied with and without CNCs for SC-EtOH and ASCM samples. Cold crystallization peaks for PHB have typically been observed at heating rates of ~0.5 ˚C/s from completely quenched PHB samples.[205] Cold reorganization behavior was observed in VH-CC experiments at heating rates of 5 ˚C/s,

when the cooling rate was 1 ˚C/s in all samples, and at 10 ˚C/s, cold crystallization peaks were observed in the ASCM neat PHB samples and the SC-EtOH neat PHB sample. These results suggested that for partially crystallized PHB, heating at rates of 5 ˚C/s (300 ˚C/min) was not sufficiently fast to prevent reorganization for the CNC loaded samples whereas a heating rate greater than 10 ˚C/s was needed to prevent reorganization in the neat PHB samples. The enthalpy calculated from the cold crystallization peaks at 5 ˚C/s indicated that both cold crystallization and MRR was suppressed with the addition of CNCs.

VC-CH experiments were performed on the SC-EtOH samples to determine the effect of CNCs on the development of crystallinity at different cooling rates. More crystallinity was developed in the CNC loaded samples at all cooling rates. At a cooling rate of 0.5 ˚C/s (30 ˚C/min), the most crystallinity was developed in the 0.5wt. % CNC/PHB samples. However at higher cooling rates, the most amount of crystallinity was developed in the 1.0 wt. % CNC/PHB samples. From the literature, a cooling rate of 200 ˚C/min or 3.3 ˚C/s was the cooling rate needed to create a completely amorphous sample.[205] At a cooling rate of 5 ˚C/s, both the 0.5 wt. % CNC/PHB and 1.0 wt. % CNC/PHB developed a significant amount of crystallinity. These results suggested that the addition of CNC significantly increased the amount of crystallinity that was developed at the higher cooling rates, and these results were similar to the results obtained from the nonisothermal experiments performed OMMT/PA6 nanocomposite.[206]

In the IC-VH experiments, the effect of superheating was examined in the ASCM and SC-EtOH samples. The results from the IC-VH experiments indicated that superheating did not occur in the SC-EtOH at heating rates up to 400 ˚C/s, whereas the effects of superheating and thermal lag manifest itself in the measurement of the ASCM sample at heating rates above 50 ˚C/s

From the isothermal experiments, the effect of CNC addition on the crystallization kinetics of SC-EtOH PHB was seen. At 10s, differences in the development of crystallinity can be seen between the CNC loaded samples and the neat PHB samples. Crystallinity developed more quickly at higher temperatures at short isothermal hold times up to 60s for the CNC loaded samples; however at isothermal hold times of 60s the crystallinity of all the SC-EtOH samples were similar. As the isothermal hold time was further increased to 500 s, the neat PHB sample developed the greatest amount of crystallinity and the 1.0 wt. % CNC/PHB sample developed the least amount of crystallinity, This results was most likely due to the increased nucleation density of the 1.0 wt. % CNC/PHB samples create more amorphous content associated with regions where impingement occurs. From the isothermal experiments, the RAF was calculated for all SC-EtOH samples at the different isothermal crystallization temperatures. The changes in the RAF as a function of time providing information regarding the differences in the crystallization behavior between neat PHB and CNC loaded samples. The initial development of the RAF was retarded at 10s and 20s, but then amount of RAF is drastically increased at 60s. In all samples the RAF at 500s was significantly lower than 60s, indicating that the amount of crystalline surface area was decreased as the isothermal hold time was increased. This result was consistent with what is expected because the total surface of the crystalline regions are should be reduced as the isothermal crystallization time is increased.

In this work, the solidification of CNC/PHB nanocomposites has been quantitatively and systematically analyzed as a function of the crystallization conditions in a manner similar to the way that the OMMT/PA6 system was studied.[206] The results from these experiments suggested that the addition of CNCs aided in the development of crystallinity at fast cooling rates, which could influence the structure evolution during conventional polymer processing and forming methods. From the isothermal

experiments, the addition of CNCs increased the temperature at which nucleation controlled growth occurred. These results indicated that as CNCs were added, the number of nucleation events that occurred at higher temperatures would increase. These results also suggested that the shorter annealing times could be used during thermal treatment of PHB with CNC addition due to rate of crystallization.

CHAPTER 5

5.1 Introduction

In the previous chapters, differences in the morphology and crystallization behavior between the sample processed by different methods have been described. In this chapter, differences in the mechanical behavior between the ASCM and SC-EtOH samples are examined. Two types of experiments are used: dynamic mechanical analysis (DMA) and tensile testing. DMA is used to characterize the differences in viscoelastic properties of PHB with different CNC loadings and processed by different methods. Tensile testing will be used to characterize the differences in the tensile strength and strain at failure for the materials.

Differences in the filler-matrix interactions have been observed for CNC-based composites using large deformation testing such as tensile testing.[17,55] Mechanical testing can also be used to characterize different properties of the matrix-filler interactions such as the thickness of the interphase[17,18,207] and the changes in the polymer mobility as a function of nanoparticle loading.[31]

Also in this chapter, the effect of aging at ambient conditions on the tensile strength and strain at failure values of neat PHB and CNC/PHB samples will be studied. When stored at room temperature, aging of PHB occurs through progressive crystallization. This progressive crystallization leads to the embrittlement of PHB which results in a decrease in the strain to failure. One of the objectives of this research was to understand how CNCs impact this aging process.

5.2 **Experimental Procedures**

5.2.1 Dynamic mechanical analysis.

DMA tests were performed using a Mettler Toledo DMA 861^e using tensile deformation. Samples produced by the ASCM and SC-EtOH methods with a nominal thickness of 0.15 mm, width of 3.5 mm and length of 9 mm were used. The measurements were performed in the linear viscoelastic range, established through a series of strain sweep measurements for all of the materials at -55 °C and at 60 °C. The testing was performed using a force amplitude of 0.08 N below T_g and a strain amplitude of 1 μm above T_g. The temperature was varied from -55 to 80 ºC at a heating rate of 2 ºC/min, and the measurements were performed at a frequency of 1 Hz. At least two temperature scan tests were conducted on each material.

The quantities obtained from the DMA experiments were the storage modulus (E') which represented the elastic nature of the sample and loss modulus (E") which represented the viscous nature of the sample. The ratio of these quantities was also calculated as tan(δ) using the expression below:

$$\tan(\delta) = \frac{E''}{E'}$$

Where δ is the phase lag between the stress and strain under sinusoidal loading.

5.2.2 Tensile testing

For the tensile testing, small strip samples with a nominal width of 4.5 mm and nominal length of 15 mm were used with a testing speed of 0.10 mm/min. Tensile testing was performed using a MTS Insight with a 100N load cell. ASCM and SC-EtOH samples were tested. Strain was calculated from the crosshead extension using the distance between the grips as the original sample length. A nominal sample thickness of 0.175 mm was used for the ASCM samples. A smaller sample thickness was needed to

accommodate the films produced by the SC-EtOH method. To facilitate comparison between the two processing methods, ASCM samples with similar film thicknesses were prepared for this testing. Tensile testing was performed on samples stored at room temperature for 1, 5, 15, and 30 days. Tensile strength and strain at break results were reported from these tests. At least 2 tensile tests were performed for each condition.

5.3 **Effect of nanoparticle addition on thermo-mechanical behavior of PHB**

In this section, the results of DMA experiments are presented. These experiments were conducted to understand the how the dynamics and viscoelastic properties of the PHB matrix was affected by the presence of CNCs.

5.3.1 Viscoelastic properties of SC-EtOH samples

The average E' values as a function of temperature are shown in Figure 5.1 for the samples tested for the each CNC loading and Table 5.1 shows E', E" and tan(δ) data at selected temperatures above and below T_g for the SC-EtOH samples. From this figure and the values provided in Table 5.1, the behavior of the storage modulus as a function of temperature of all samples was similar. Therefore, these results suggested that the addition of CNCs did not improve the storage modulus. This result was expected due to the sub-percolation threshold levels of CNCs were added. The differences in the loss modulus of the different CNC/PHB samples and the neat PHB are shown in Figure 5.2. The shape of E" appeared to be similar between the neat PHB and the 0.5 wt. % CNC/PHB, and it is worth noting that there was an increase in the value of E" at temperatures above 20 ˚C seen in the 1.0 wt. % CNC/PHB, However, there was significant error associated with the these data, making it difficult to state that there was a clear difference seen in this material relative to the neat PHB.

The values of T_g for the SC–EtOH samples were obtained by finding the temperature at which the peak value of E" occurred. From this method, the calculated values of T_g are shown in Table 5.2 as $E"_{max}$ for the neat PHB, 0.5 wt. % CNC/PHB and 1.0 wt.% CNC/PHB. A distinct increase in the value of T_g relative to the neat PHB was observed in the 1.0 wt. % CNC/PHB. These results suggested that there were favorable component interactions between PHB and CNCs.

In Figure 5.3, the tan(δ) of the SC-EtOH samples is plotted as a function of temperatures, and the average value for of $\tan(\delta)_{max}$ is shown in Table 5.2. $\tan(\delta)_{max}$ represents the relaxation strength of the amorphous phase and is an indicator of the toughness of PHB.[134] From the values obtained in Table 5.2, the $\tan(\delta)_{max}$ remainED relatively constant with nanoparticle loading. These results indicated that no significant differences in the toughness or ratio of viscous to elastic character were caused by the addition of nanoparticles.

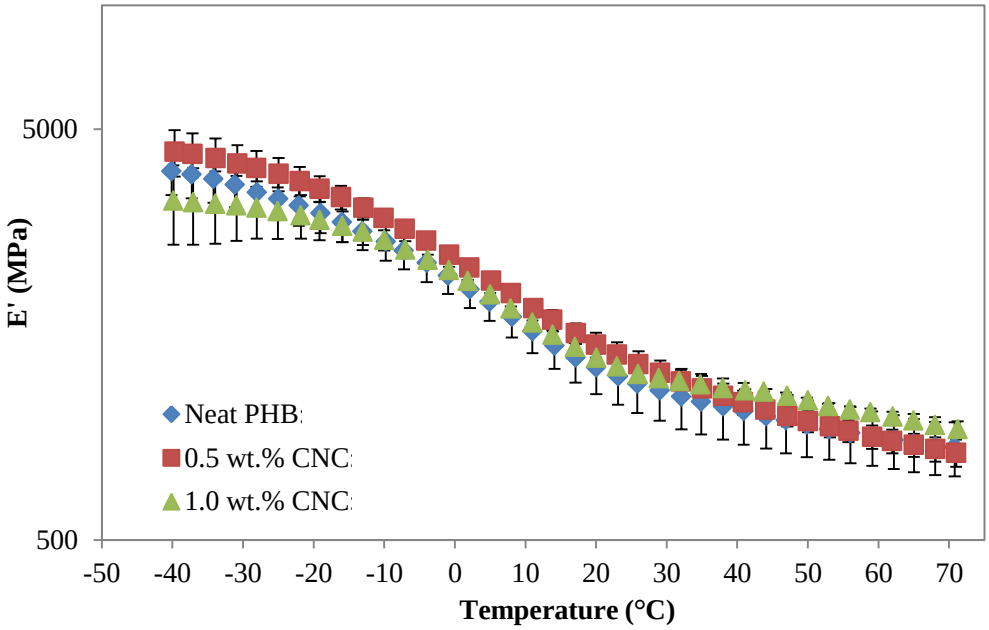

Figure 5.1. Storage modulus as a function of temperature for the SC-EtOH samples.

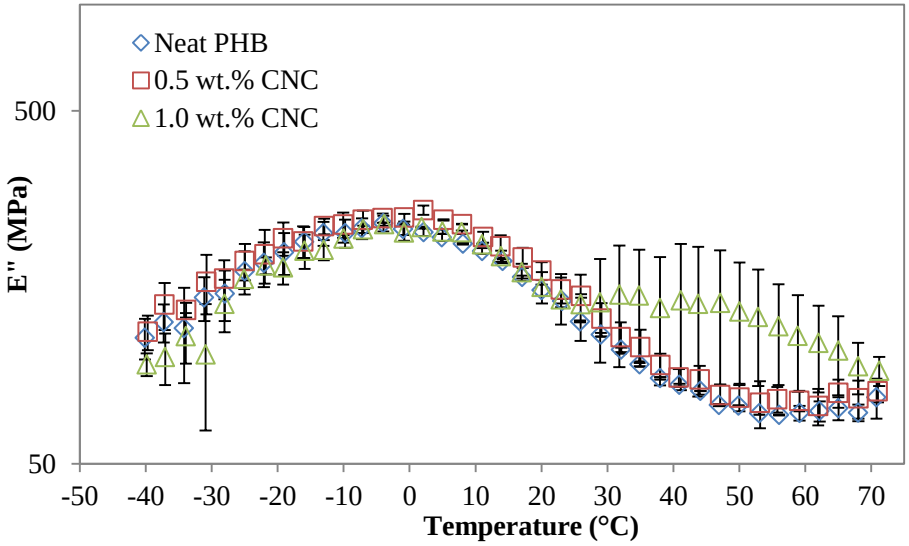

Figure 5.2. Loss modulus as a function of temperature for the SC-EtOH samples.

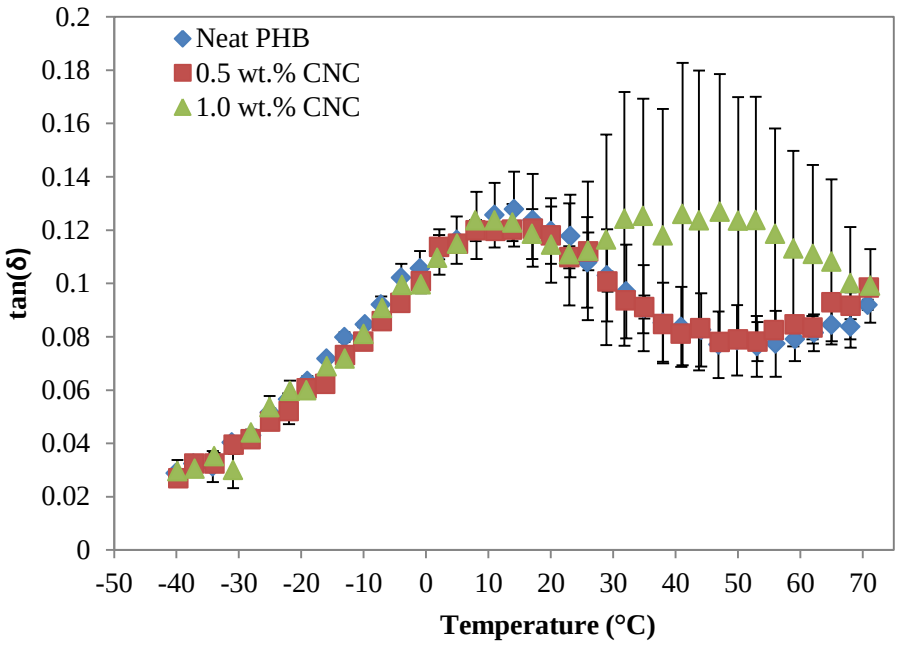

Figure 5.3. Tan(δ) as a function of temperature for the SC-EtOH samples.

Table 5.1. Average values of the storage modulus, loss modulus, and tan(δ) of SC-EtOH samples.

	Temp. (°C)	E' (MPa)		E" (MPa)		tan(δ)	
Neat PHB	-30	3660	±431	148	±21	0.04	±0.001
0.5 wt. % CNC/PHB	-30	4120	±448	164	±31	0.04	±0.003
1.0 wt. % CNC/PHB	-30	3260	±586	102	±40	0.03	±0.006
Neat PHB	50	954	±158	73	±0	0.08	±0.013
0.5 wt. % CNC/PHB	50	973	±58	77	±7	0.08	±0.002
1.0 wt. % CNC/PHB	50	1093	±0	135	±51	0.12	±0.046

Table 5.2. T at E"$_{max}$ and tan(δ)$_{max}$ for the SC-EtOH samples.

	Temp. at E"$_{max}$(°C)		tan(δ)$_{max}$	
Neat PHB	-10	±2	0.13	±0.015
0.5 wt. % CNC/PHB	-5	±6	0.12	±0.001
1.0 wt. % CNC/PHB	-3	±1	0.13	±0.003

5.3.2 Viscoelastic properties of ASCM samples

The average E' values as a function of temperature are shown in Figure 5.4 for the ASCM samples, and in Table 5.3, the average values of E', E" and tan(δ) are shown at temperatures above and below T_g. At temperatures below T_g, the 1.0 wt. % CNC/PHB sample and the neat PHB exhibited similar values for E' whereas for the 0.5 wt.% CNC/PHB sample exhibited the lowest value of E'. Above T_g, the value of E" was overlapping for all of the samples. The average E" values for the ASCM samples as a function of temperature are shown in Figure 5.5. From this figure, the effect of adding CNCs into ASCM can be clearly seen. The E" values of the CNC/PHB samples were smaller than the neat PHB, and this behavior was seen best at temperatures above T_g. Using the E" data, the value of T_g was calculated as the peak of the E" curves, and

the calculated T_g values are shown in Table 5.4 for neat PHB, 0.5 wt. % CNC/PHB, and 1.0 wt. % CNC/PHB. From this table, there was an increase in the value of T_g as nanoparticles were added, however there was no significant difference between the T_g values of the 1.0 wt. % CNC/PHB and 0.5 wt. % CNC/PHB samples. The shift in the T_g to higher temperatures with nanoparticle addition has been observed in semicrystalline polymer nanocomposites using dielectric spectroscopy, and the authors attributed this shift in the T_g to higher temperatures to an immobilized interphase between the matrix and filler.[208] Also, the increase in the T_g could be due to an increased confinement of the amorphous phase, which has been observed in polymer- clay nanocomposite systems.[209–211] In Figure 5.6, the average tan(δ) data are shown as a function of temperature. At temperatures above T_g, the neat PHB sample had the greatest value for tan(δ). This result suggested that dissipation was decreased in the composite samples relative to the neat PHB. This reduction in the tan(δ) peak with nanoparticle addition has been observed in several different systems including poly(vinylidene fluoride)/MMT.[210–212]

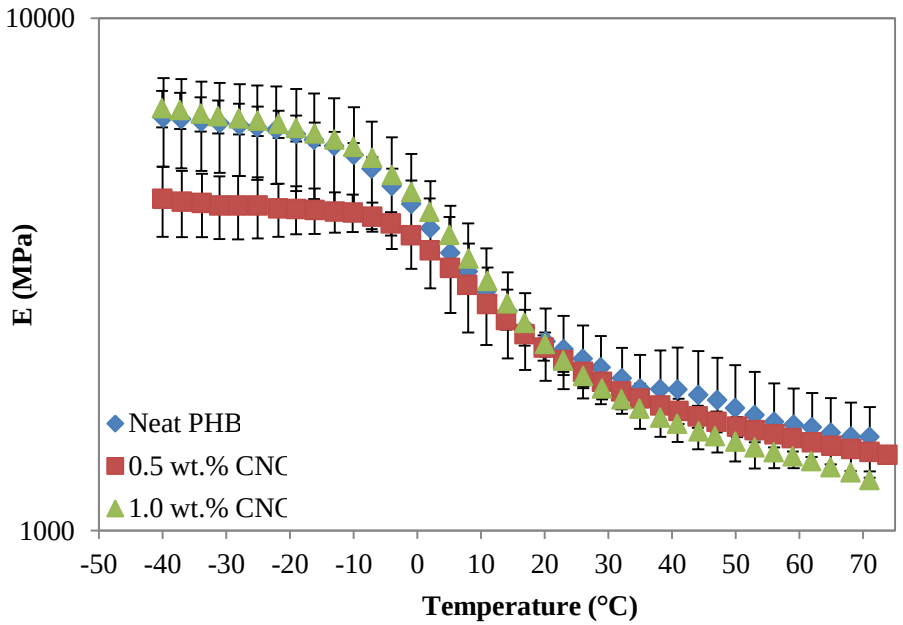

Figure 5.4. Storage modulus as a function of temperature of the ASCM samples.

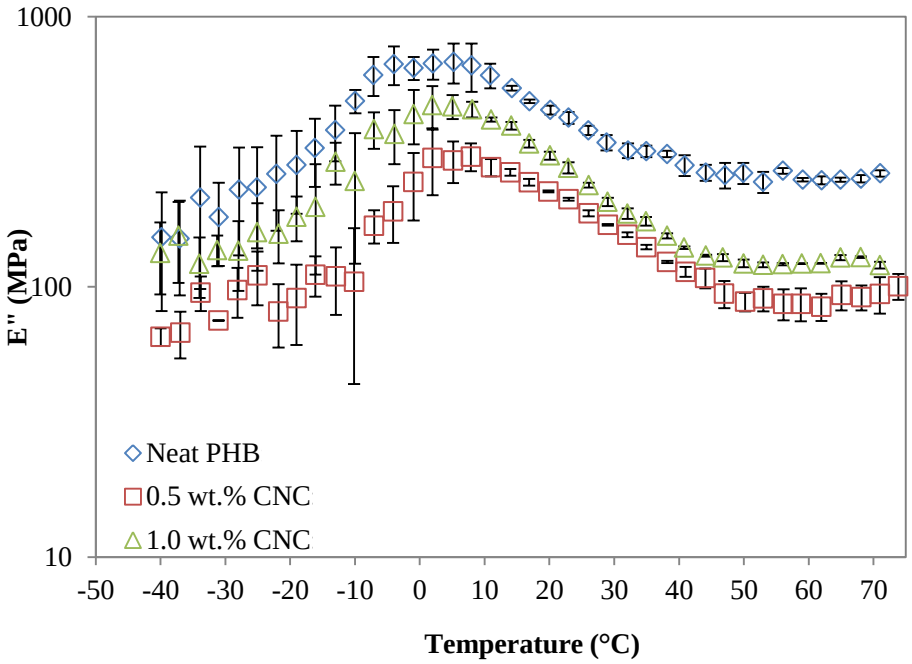

Figure 5.5. Loss modulus as a function of temperature of ASCM samples.

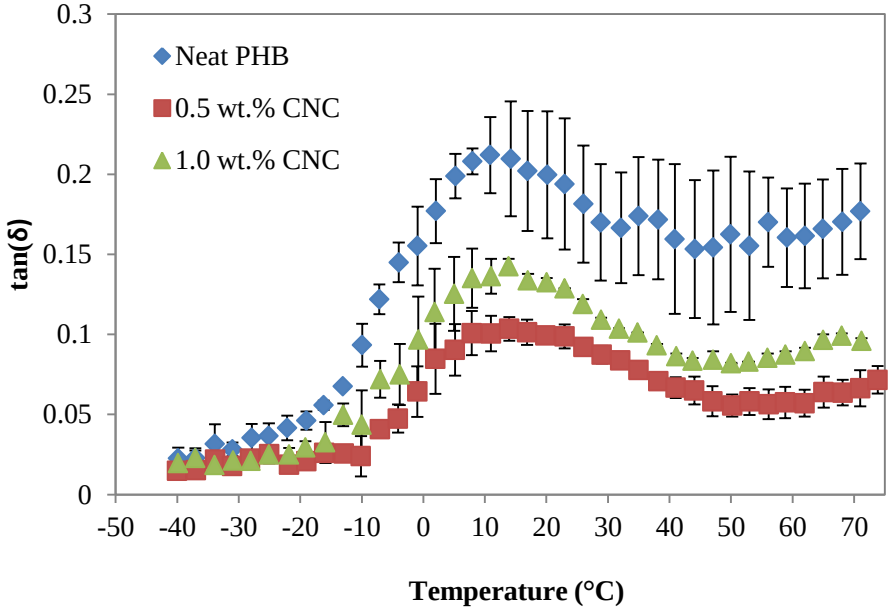

Figure 5.6. Tan delta of neat PHB, 0.5 wt.% CNC/PHB and 1.0 wt. % CNC/PHB.

Table 5.3. Average storage modulus, loss modulus, and tan(δ) values for ASCM samples

	Temp. (°C)	E' (MPa)		E" (MPa)		tan(δ)	
Neat PHB	**-30**	6238	±1245	181	±62	0.03	±0.004
0.5 wt. % CNC/PHB	**-30**	4313	±603	75	±0	0.02	±0.003
1.0 wt. % CNC/PHB	**-30**	6441	±478	137	±18	0.02	±0.001
Neat PHB	**50**	1735	±370	264	±24	0.16	±0.048
0.5 wt. % CNC/PHB	**50**	1596	±72	88	±7	0.06	±0.007
1.0 wt. % CNC/PHB	**50**	1491	±44	122	±4	0.08	±0.000

Table 5.4. T at E''_{max} and $\tan(\delta)_{max}$ for the ASCM samples

	Temp. at E''_{max} (°C)		$\tan(\delta)_{max}$	
Neat PHB	-2	±3	0.22	±0.022
0.5 wt. % CNC/PHB	5	±3	0.11	±0.009
1.0 wt. % CNC/PHB	5	±2	0.15	±0.008

5.3.3 Comparison of the Viscoelastic behavior of SC-EtOH and ASCM samples

Differences in the E" behavior and tan (δ) behavior between the neat PHB sample and the CNC/PHB samples for the SC-EtOH and ASCM processing methods indicated that there were changes in the mobility of the amorphous component as nanoparticles were added and also indicated that different reinforcement behaviors were associated with the two processing methods. For the SC-EtOH samples, the E" curves and tan(δ) curves were similar for all SC-EtOH samples. These results suggested that there was no significant difference in the viscoelastic behavior with nanoparticle addition for the SC-EtOH based processing since E' and E" were reinforced similarly. For the ASCM samples, there was a reduction in the magnitude of E" and tan(δ) when comparing the neat PHB with the 0.5 wt.% CNC/PHB and the 1.0 wt. % CNC/PHB. These results

indicated that the viscous nature decreased with nanoparticle loading. As stated previously, De Koning et al. suggested that the value of tan(δ) was an important indicator of the toughness and aging behavior of PHB.[134,182] Differences in the value of $\tan(\delta)_{max}$ can be caused by constraint in the amorphous regions or by changes in the amorphous phases.[134] Since the crystallinity remained relatively constant in the ASCM samples (60-62%), then the change in the $\tan(\delta)_{max}$ should be due to the addition of nanoparticles . In the SC-EtOH samples, the $\tan(\delta)_{max}$ did not change as nanoparticles are added into the PHB; therefore, these results indicated that the addition of CNCs into the SC-EtOH PHB matrix did not change the toughness of the material. In the ASCM samples, the addition of nanoparticles decreased the $\tan(\delta)_{max}$. This reduction in the $\tan \delta_{max}$ indicates that the viscous dissipation that occurs in the CNC loaded samples was less than that of the neat PHB samples. These results suggested that the ASCM processing produced an interphase that caused a greater reduction in the mobility of the amorphous fraction when compared with the SC-EtOH samples. This was consistent with what was expected because the additional precipitation step was expected to change the nature of the CNC/PHB interaction, forcing the PHB to precipitate around CNCs whereas in the SC-EtOH samples, the CNCs and PHB interacted as the solvent evaporated after the film was cast. Similarly, the differences in the temperature corresponding to $E''_{max,}$ which was used to assign the value of T_g,of the SC-EtOH samples and the ASCM samples suggested that an interphase was formed in the composites. Overall, the values of T_g for the SC-EtOH samples were lower than those for the ASCM samples. It was expected that the structure of the interphase in composites produced by these two methods was different since the trends in tan(δ) at temperatures above T_g were different, but the change in the value of T_g with respect ti neat PHB was similar at a CNC loading of 1 wt.%.

The differences in the interphase should create differences in the "aging" behavior. Several studies have suggested that the RAF associated with the crystalline

phase of PHB plays a role in the progressive crystallization that occurs during storage at ambient temperatures.[132,182,202] However when nanofillers are introduced into a semicrystalline polymer matrix, another form of rigid amorphous fraction can form from the interactions between the nanofiller and the matrix, and this version of a RAF is often referred to as the interphase. The addition of CNCs into PHB processed via ASCM should inhibit the progressive crystallization that occurs during aging due to the presence of an interphase that cannot transform. Also, the results of the hot stage microscopy discussed in Chapter 3 indicated that the addition of CNCs into PHB reduced the growth rate of the PHB spherulites for both the ASCM system and the SC-EtOH system. From the hot stage microscopy results, the decrease in the growth rate for the ASCM system with CNC addition was greater than SC-EtOH system. These results suggested that the rate of crystal growth should be retarded with the addition of CNC, especially for the ASCM system. Therefore the less mobile amorphous fraction of the ASCM CNC/PHB system should retard the rate of the progressive crystallization that occurs in PHB during storage in ambient temperatures when compared with more mobile amorphous fraction of the SC-EtOH system.

5.4 **Tensile Testing**

Tensile testing was performed on ASCM and SC-EtOH samples to determine differences in the mechanical behavior of PHB at large deformations as a function of processing method, CNC loading, and aging time. Figure 5.7 and Figure 5.8 shows the differences in the stress-strain curves for the SC-EtOH and ASCM samples respectively at an aging time of 1 day. From these figures, differences in the strain at failure and tensile strength between the neat PHB samples and the CNC/PHB samples can be seen. The strains at failure values of the CNC loaded samples were greater at shorter aging times than the neat PHB sample for both processing methods. Figure 5.9 shows the change in the stress-strain curves as a result of aging time for the SC-EtOH 0.5 wt. %

CNC/PHB sample and Figure 5.10 shows the change in the stress strain curves as storage time was increased for the ASCM 0.5 wt.% CNC/PHB sample. In Figure 5.11, differences in the strain to failure and the tensile strength are shown as a function of days stored at room temperature for the SC-EtOH samples. The tensile strength remained relatively constant as the storage time increased to 30 days, but the strain at failure decreased significantly for the CNC/PHB loaded samples. This decrease in strain at failure with increasing aging times has been observed previously and attributed to embrittlement of PHB through secondary crystallization at room temperature.[132,134,143,199] The impact of CNCs on this embrittlement process was most evident at short aging times. The addition of nanoparticles significantly increased the strain at failure for the SC-EtOH sample initially, but the strain to failure of the CNC loaded samples became almost identical to the neat PHB after 15 days. These results indicated that the aging process could be slowed by the addition of CNCs but not completely suppressed.

The aging behavior of the ASCM samples was slightly different from the aging behavior of the SC-EtOH samples. Figure 5.10 shows how the 0.5 wt. % CNC/PHB sample changes with aging time. Like the SC-EtOH samples, the strain at failure decreased as the storage time was increased. Figure 5.12 shows the tensile strength and strain at failure as a function of storage time for the ASCM samples. The tensile strength did not change dramatically with aging time for most of the samples and aging times used here. The strain to failure behavior of the ASCM samples was similar to that of the SC-EtOH samples. For the 1 wt. % CNC/PHB sample, there was a drastic decrease in the strain to failure as the storage time was increased from 5 day to 15 days from 14.2% ± 3.2% to 8.5% ± 1.5%. As the storage time was further increased from 15 days to 30 days, there was small decrease in the strain at failure from 8.5% ± 1.5% to 7.8% ±0.2%.

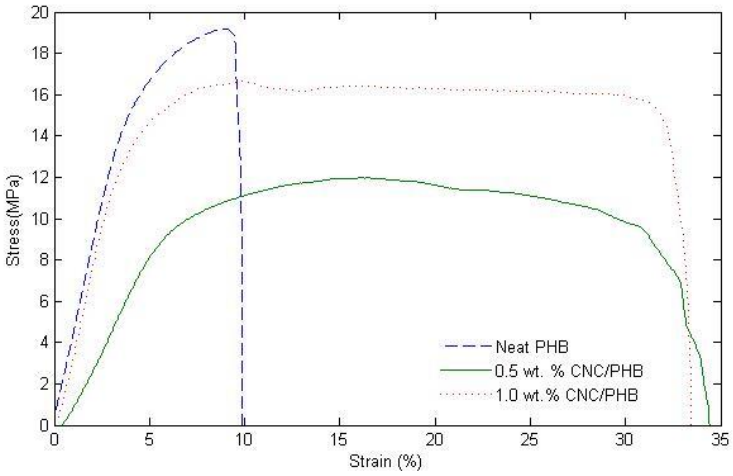

Figure 5.7. Stress-strain curves for SC-EtOH neat PHB (dash), 0.5 wt. % CNC/PHB(dot) and 1.0 wt. % CNC/PHB(solid) after 1 day

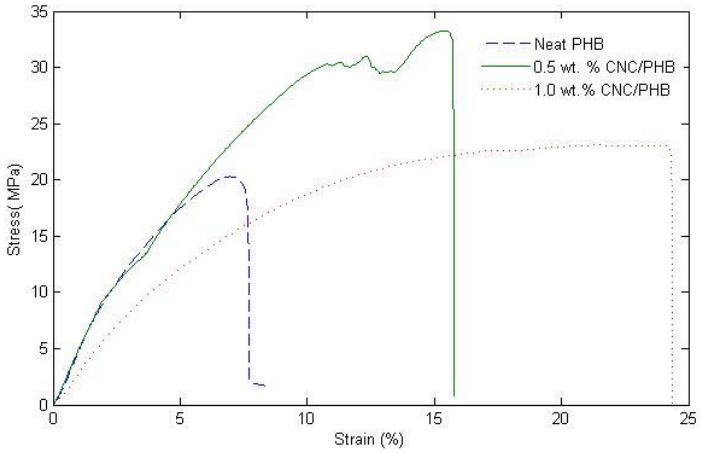

Figure 5.8. Stress strain curves for ASCM samples after 1 day.

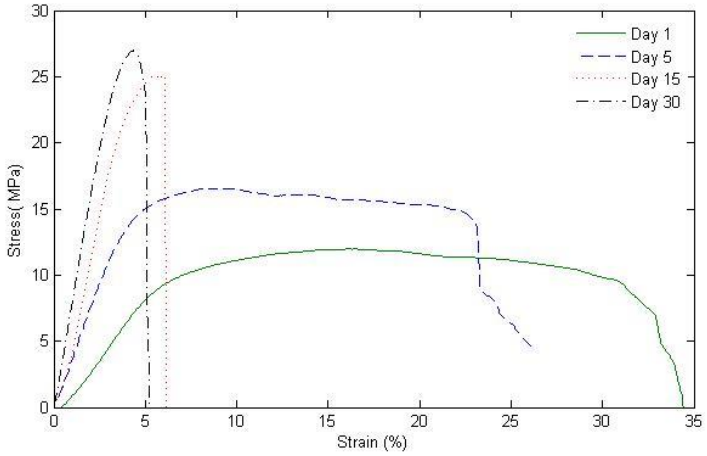

Figure 5.9. Change in the stress strain curves with time for the SC-EtOH 0.5 wt.% CNC/PHB sample

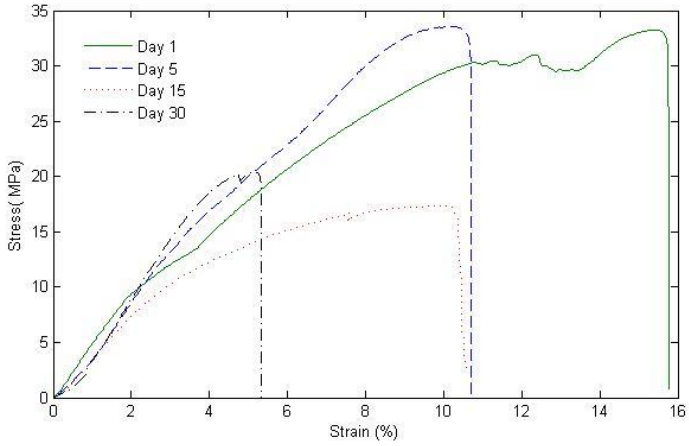

Figure 5.10. Effect of aging on the stress strain curves of ASCM 0.5 wt. % CNC/PHB sample for 1 day (bold), 5 day (dot) 15 day (dash), and 30 day (solid).

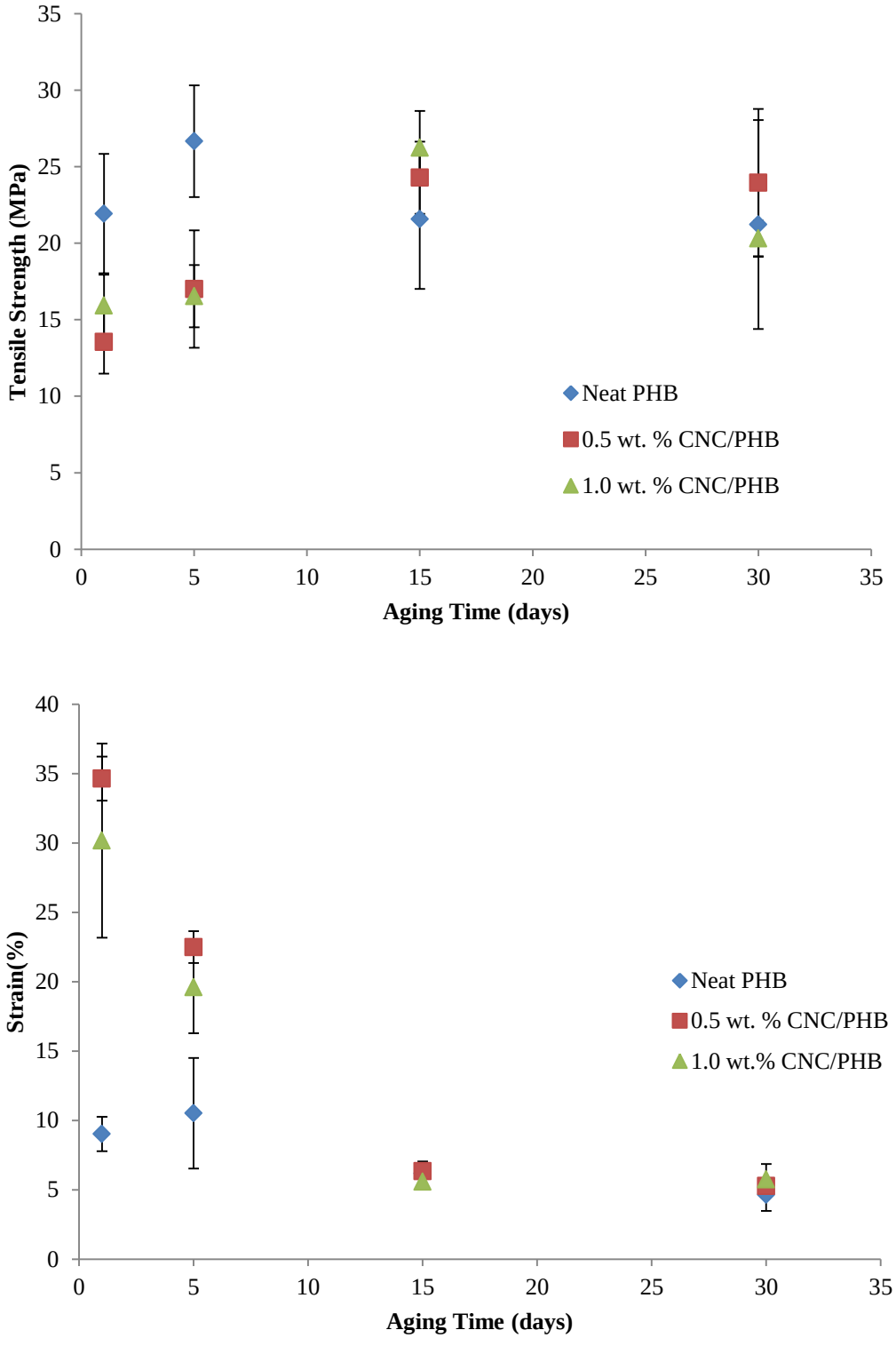

Figure 5.11. Change in the tensile strength (top) and strain at failure (bottom) for SC-EtOH samples.

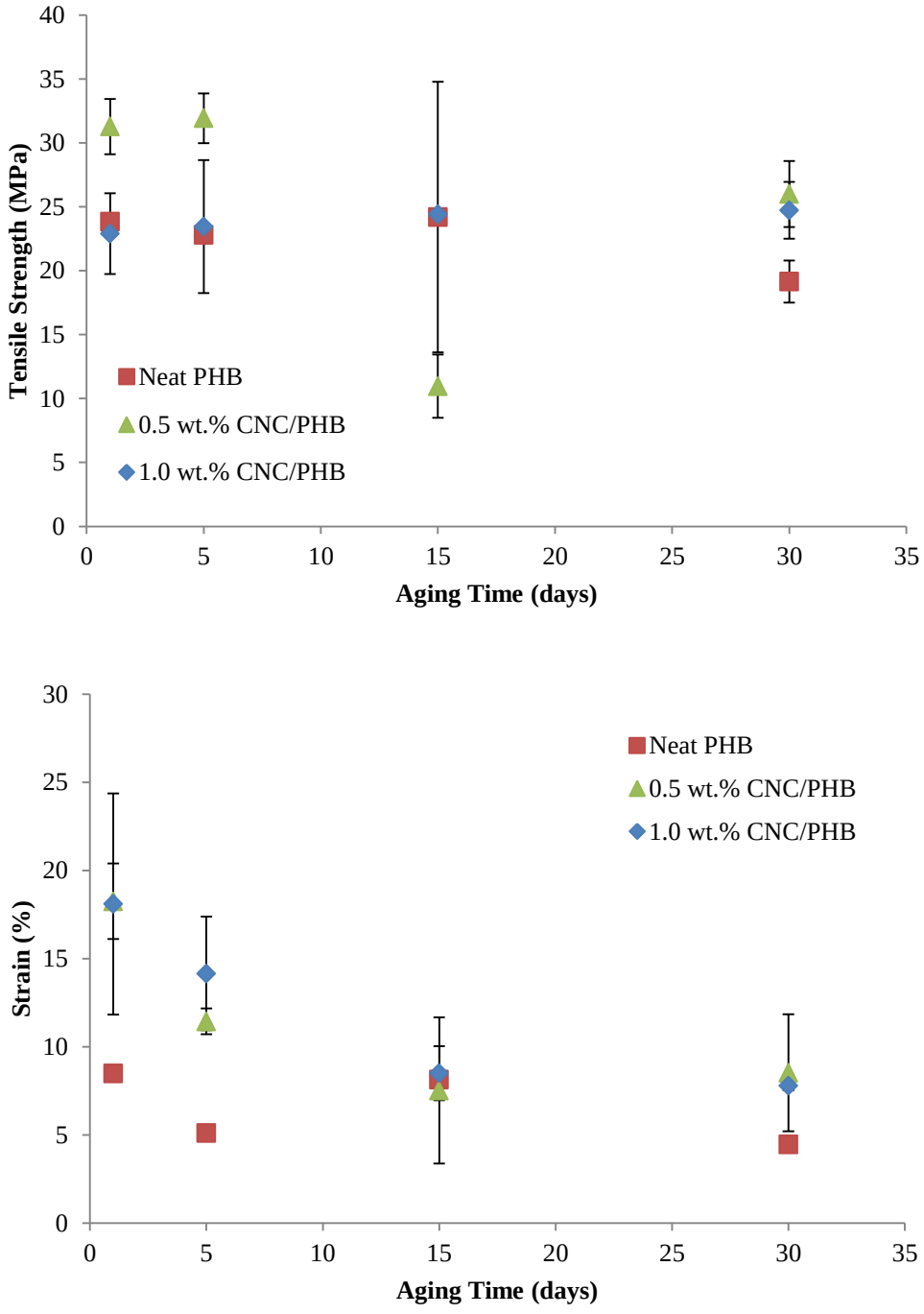

Figure 5.12. Change in the tensile strength (top) and strain at failure (bottom) for ASCM samples.

5.4.1 Discussion of tensile test results.

For all samples, the most drastic change in the strain to failure was seen between aging times of 1 day and 15 days. This decrease in properties could be due to progressive crystallization occurring within the system, and this process has been shown to be related to the thermal history of the PHB sample. Figure 5.13 illustrates how storage time at ambient temperatures changes the amounts of RAF (w_{RA}), MAF (w_A), and crystallinity (w_c) in PHB that has been cooled at 20 °C/min and 5 °C/min from a molten state.[132] For the PHB sample cooled at the faster rate, the crystallinity had increased from 35% to 55% after storage at room temperature for 1 day, and after 5 days, the crystallinity was approximately 60%, whereas for the sample cooled at 5 °C/min, the initial crystallinity was 64% and after a day of storage, the crystallinity of the sample was increased to 68%.[132] For PHB, the morphology dictates to what extent aging occurs, and in particular, the amount of RAF present. Progressive crystallization occurs in PHB at room temperature by attempting to reduce the strain at the crystalline-amorphous interface.[134,182] In the ASCM processing, the sample was cooled at a nominal rate of 12 °C/min, and from the thermal sweep DSC experiments, the samples had crystallinity values ranging between 60- 62%. These results suggested that the change in crystallinity, MAF and RAF should fall somewhere between these two scenarios for the ASCM samples.

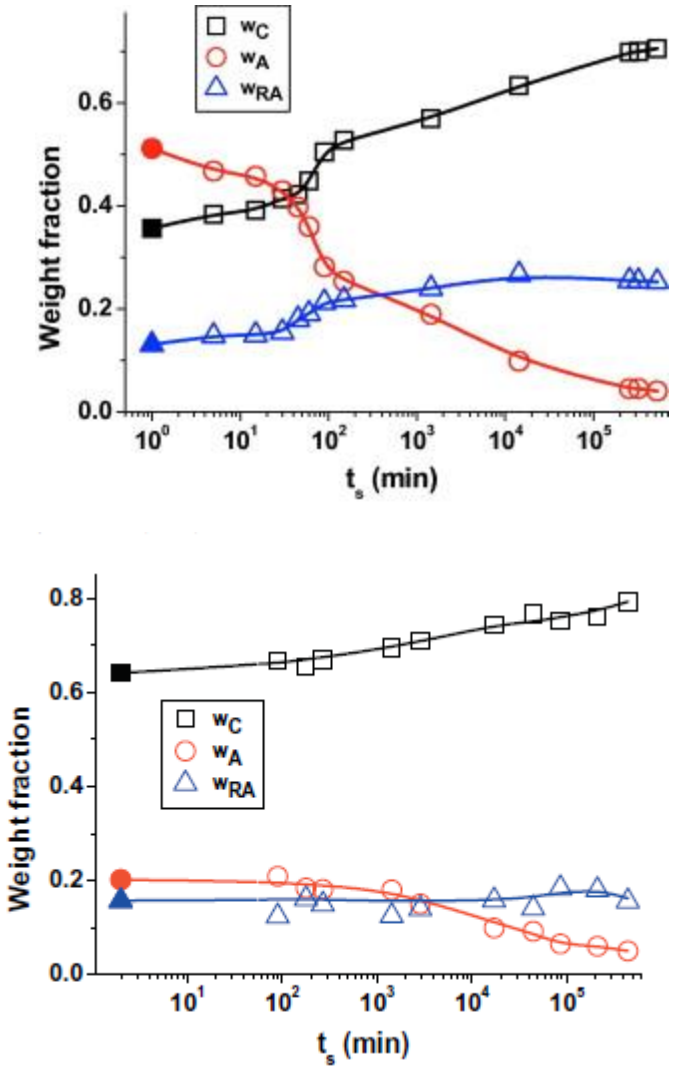

Figure 5.13. Evolution of crystallinity for PHB cooled at 20 ˚C/min (top) and 5 ˚C/min [132]

The overall strain to failure of the neat PHB samples were relatively similar at day 1 with the strain to failure of the SC-EtOH neat PHB sample of 9.0%±1.2% whereas the ASCM neat PHB sample had a strain to failure of 8.5%±0.2%. However, the for the CNC/PHB samples, there was a slight difference in the initial strain to failure of the ASCM and SC-EtOH. For the 1.0 wt. % CNC/PHB samples, the initial strain to failure was 30.2%±7.0% and 18.1%±6.3% for the SC-EtOH and ASCM samples respectively. The 0.5 wt.% CNC/PHB samples exhibited a similar trend with the initial strain to failure

of the SC-EtOH sample at 34.6%±1.6% whereas the initial strain to failure of the ASCM sample was 18.3%±2.1%. The differences in this initial strain to failure can be attributed to both the differences in morphology and the overall crystallinity of the samples. The differences in the morphology of the two processing methods were discussed in Chapter 3. The ASCM sample had large spherulites that were observed using optical microscopy. From the literature the solvent casting method typically produces spherulites with a diameter less than 2μm.[213] The finer spherulite size of the SC-EtOH should result in increased strain at failure, which is consistent with what was observed. With regards to the crystallinity of the samples, the crystallinity of the as processed samples, which were calculated from the first heating cycle melting peaks were 60.1% ±2.7% and 50.0%±0.1% for the ASCM neat PHB and SC-EtOH neat PHB respectively. Because the SC-EtOH sample contained less crystallinity, more progressive crystallization should have occurred within the SC-EtOH neat PHB sample compared with the ASCM neat PHB sample. After 30 days, the strain to failure of the neat PHB ASCM and SC-EtOH samples were 4.5 %±0.1% and 4.6%±1.2%. These results suggest that after 30 days of storage under ambient condition, the effect of progressive crystallization was similar for the two neat PHB samples.

For the CNC loaded samples, a similar difference in the initial strain to failure was observed between ASCM samples and the SC-EtOH samples. The initial crystallinity values for the SC-EtOH samples were 63.7% ±1.0% and 62.5%±2.6% for 0.5 wt. % CNC.PHB and 1.0 wt. % CNC/PHB respectively. For the ASCM samples, the initial crystallinity values were 59.4% ±4.1% and the 60.9% ±1.3%. From these crystallinity values, it was expected that the effect of progressive crystallization should be similar between the ASCM samples and the SC-EtOH samples. However, at 30 days the strains to failure of the ASCM samples are slightly higher than of the SC-EtOH samples. For the 1.0 wt. % CNC/PHB samples, the strain to failure of the ASCM sample was

7.8%±0.2% whereas the strain to failure of the SC-EtOH sample was 5.7%±1.1%. A similar trend was also observed in the 0.5 wt. % CNC/PHB sample. This deviation from the expected behavior could be due to the differences in the CNC/PHB interphase that was formed during the two different processing methods. From the results from the hot stage microscopy and the higher values of T_g for the ASCM sample, the interphase formed during ASCM processing resulted in a reduction in the overall mobility of the amorphous component. This reduction in the mobility of the amorphous component resulted in a significant decrease in the rate of crystallization of the PHB during isothermal experiments performed at 110˚C, which was discussed in Chapter 3 and should have inhibited the progressive crystallization occurring at ambient temperatures, ultimately reducing the rate at which embrittlement occurred within the sample.

5.5 **Conclusions**

The SC –EtOH and ASCM exhibited different viscoelastic behavior as nanoparticles were added. For the SC-EtOH samples, adding CNC did not significantly change the viscoelastic behavior. However, the addition of CNCs during the ASCM processing changed the viscoelastic behavior of the sample. There was a decrease in the loss modulus as CNCs were added, which decreased the tan(δ) curves. These results indicated less dissipation with the addition of CNCs for the ASCM samples. The differences in the tan(δ) of the CNC/PHB loaded samples between the two different processing methods suggested that the interphase between the CNC and PHB for the ASCM and SC-EtOH processing methods were different For both processing methods, the average T_g for each CNC loading was calculated from the peak of the individual E" curves. Samples produced by both processing methods showed significant differences in Tg for the neat PHB and the 1.0 wt.% CNC/PHB samples. These results indicated that

the CNCs and the PHB were interacting with one another, thus increasing the T_g. These results also suggested that the addition of CNCs resulted in a reduction in the mobility of the amorphous component in the ASCM samples. These results indicate that interphase formed during processing

Results from tensile testing suggested that for SC-EtOH processing, the addition of nanoparticles did increase the strain at failure but did not significantly impact the tensile strength. However, the addition of CNCs did not prevent the embrittlement of PHB; therefore at 15 days the strain at failure and tensile strength of the CNC/PHB samples were similar to the neat PHB samples. For composites produced with ASCM processing, the strain at failure were increased at shorter aging times and the tensile strength remained relatively constant. However, the strain to failure decreased as the aging time was increased but the tensile strength remained relatively constant. The differences in the embrittlement behavior between the SC-EtOH and ASCM processed samples were attributed to the differences in the mobility of the amorphous phase. The SC-EtOH samples had an amorphous component which was more mobile than the amorphous component of the ASCM samples at room temperature due to the lower values of T_g in the SC-EtOH samples, thus the increased mobility of the amorphous component in the SC-EtOH sample allowed for the progressive crystallization to occur within the SC-EtOH sample at a faster rate than in the ASCM. These results indicated that if the mobility of the amorphous component was reduced significantly, the progressive crystallization during storage at room temperature can be inhibited.

CHAPTER 6

CONCLUSIONS AND FUTURE WORK

6.1 **Conclusions**

The objective of this research was to determine the design space available for CNC/PHB nanocomposites. To achieve this objective, the morphology was examined at several different steps in a step-wise processing operation. The effect of the different processing on the development of crystallinity under different thermal treatments and also the effect of processing on the interphase formed was examined. The mechanical behavior of the CNC/PHB samples that were processed at different steps in the processing operation was examined. This research examined how the different component interactions affected the development of the semicrystalline structure, and examined the differences in the mechanical properties associated with some of the different processing methods. This research also provided valuable insight into the mechanisms associated with initial stages of primary crystallization in a semicrystalline polymer as well as the role of the RAF in the development of crystallinity during isothermal crystallization of PHB and CNC/PHB nanocomposites. This information also provides insight into how nucleation and growth of the crystalline phase changes with nanoparticle addition. This knowledge can used when designing heat treatments for PHB based materials to control the morphology of the material in order control the mechanical properties and prevent the embrittlement of the material during storage.

In the first study (Chapter 3), the effect of processing on the nanocomposite morphology was investigated. The CNC/PHB nanocomposite and neat PHB samples were examined at four different points in a stepwise processing operation. Optical microscopy revealed significant differences in the morphology between the SC samples and the ASCM samples. The experimental results also suggested that effect of

nanoparticle on the crystallization behavior changed at different steps in the processing operation. For the SC-based methods, using a water based CNC suspension resulted in slower crystallization kinetics and MRR behavior when compared with the ethanol based CNC suspension. The difference in the morphology between these two methods was attributed to the role of the water in altering the crystallization behavior of PHB by inhibiting intramolecular hydrogen bonding from occurring in the SC-H_2O samples. These results were significant because these results provided information regarding the role of the solvent (used in the dilution of the CNCs) in the development of the semicrystalline structure. Also no previous research has examined the role of AS based processing on the altering the development of the semicrystalline structure of PHB. The results from the isothermal crystallization experiments indicated that the AS-based methods produced significantly faster crystallization kinetics when CNCs were added. The addition of CNCs decreased the average spherulite size and increased the crystallization kinetics of all samples, but the results from the hot stage microscopy indicated that the growth rate of the spherulites was reduced with CNC addition of the ASCM and SC-EtOH samples whereas the growth rate of the spherulites in the SC-H_2O samples increased with increased CNC loading. The results suggest that the addition of CNCs increased the crystallization kinetics of PHB by increasing the nucleation density, not necessarily by increasing the rate of spherulite growth. These results are consistent with what has observed in the literature. Several studies have shown that cellulose based nanofillers have acted as successful nucleating agents for PHB and PHBV.[63,171,214]

In the second study (Chapter 4), the effect of initial processing and CNC addition on the evolution of the semicrystalline structure of PHB with different thermal treatments examined using the Flash DSC. To determine the effect of heating rate on the reorganization behavior, VH-CC experiments were performed. Cold crystallization at temperatures above the glass transition temperature (T_g) was observed at heating rates

lower than 10 ˚C/s (600 ˚C/min) for the neat samples and 5 ˚C/s for the CNC/loaded samples. These results suggested that the addition of CNC inhibited the recrystallization behavior upon heating. The cold crystallization peaks that were observed at 5 ˚C/s and 10 ˚C/s were not expected because the cold crystallization of PHB was suppressed in conventional DSC at a heating rate of 200 ˚C/min.[85,186] The VC-CH experiments were performed to determine development of crystallinity at different cooling rates. From these experiments, increased crystallinity was observed with nanoparticle addition, and significant amount of crystallinity was developed in the CNC loaded samples at cooling rate faster than the rates need to completely quench PHB. Therefore these results indicate that the addition of CNCs during processing allowed for CNC-PHB interactions to occur that reduced the energy need for crystallization to occur. The results obtained from these experiments are consistent with the results obtained from a study performed on the Flash DSC which was used to determine the role of OMMT in the crystallization of PA6.[206]

A series of isothermal crystallization experiments were also performed to determine the effect of nanoparticle addition on isothermal crystallization. In the isothermal crystallization experiments, different isothermal hold times were used to capture the crystallinity, MAF, and RAF at different stages of crystallization. The results from these isothermal experiments show the role of RAF in the development of crystallinity during the initial stages of primary crystallization as well as the later stages of crystallization for the neat PHB samples as well as the CNC/PHB samples. In general, the role of the RAF in the development of the crystalline phase is not well understood, and the relationship between the RAF and the crystalline phase differs for each polymer system. For PHB, the literature suggests that the RAF parallels the growth of the crystalline phase until impingement occurs. [85,87,204] The results indicated that the development of the RAF was retarded during the short isothermal hold time (initial stages of primary crystallization) when CNCs were added. But as the isothermal hold time was

increased, the development of the RAF increased significantly. These results suggest that the addition of CNCs initially retards the growth of the crystalline phase, but then significantly increases the amount of crystalline phase that is present. This result provided insight into how the addition of CNCs changed the crystallization behavior of PHB and how the structural evolution of PHB can be controlled with thermal treatment and CNC addition.

In the third study (Chapter 5), the viscoelastic behavior as well as the tensile strength and strain to failure of the CNC/PHB samples were examined. The results from the DMA experiments indicated that there was no significant change in the mechanical reinforcement when CNCs are added during SC-EtOH processing. However, the addition of CNC into ASCM processed PHB changed the viscoelastic behavior of the system. The results from the DMA experiments showed that the addition of CNCs increased the T_g, suggesting that the addition of CNC reduced the overall mobility of the amorphous content. This reduction in the mobility of the amorphous content could inhibit the progressive crystallization that occurs in PHB during storage in ambient conditions. Results from tensile testing at different storage times indicate the presence of the CNC did initially improve the strain to failure and the tensile strength of the samples; however as the storage time increased, embrittlement of the samples occurred. The reduction in the strain to failure at long hold times was greater in the SC-EtOH samples when compared with the ASCM. The increased embrittlement observed in the SC-EtOH samples was attributed to a more mobile amorphous component at room temperature.

6.2 **Potential impact of research**

Research on PHB-based nanocomposites has been focused on controlling the rate of biodegradation and biocompatibility of the nanocomposites. In order to control these properties, the effect of different processing methods as well as different thermal processing on the development of the semicrystalline structure was examined. The

information obtained from this work providing information regarding the effect of different components –interactions on the development of the semicrystalline structure of PHB with nanoparticle addition. This work also showed how the differences in the semicrystalline structure changed the viscoelastic behavior as well as the ultimate tensile strength. This works also providing insight into how thermal processing methods can be altered when nanofillers are introduced to semicrystalline polymer matrix. This insight can be used to optimize some of the quenching and annealing processing to more effectively engineer the semicrystalline structure of a polymer matrix to specific needs.

6.3 **Recommendations for future work.**

The development of CNC/PHB nanocomposites can help pave the way for the development of many different types of biorenewable nanocomposites. Also the research presented in this thesis described some of the processing-structure-properties relationships observed for polymer nanocomposites made with semicrystalline polymers. Much progress has been made in this thesis and in the literature towards understanding and controlling the interfacial interactions that control the development of the semicrystalline structure of a nanocomposite system. Some of the challenging issues that still need further study are

Structural Studies: More detailed structural analysis of the morphologies formed during the Flash DSC isothermal crystallization experiments performed should be obtained. In particular both AFM and wide angle x-ray diffraction should be used to obtained detailed information regarding the morphologies formed and the long and short range order found within these morphologies. In this work, all of the structural information pertinent to the morphology of the samples forming in the Flash DSC was obtained from the melting curves.

Aging studies: For the aging studies, annealing treatments at different temperatures and for different lengths of times should be compared with the as processed samples to determine the effect of nanoparticle addition and thermal treatment on the "aging" of PHB. Also a more detailed analysis of the changes in the mechanical behavior and crystallinity with storage time should be obtained. In particular, changes in the viscoelastic behavior of the samples as a function of time for the ASCM and SC-EtOH samples

Processing Methods: Also, different more environmentally friendly methods of processing the PHB should be examined. In this research, both the solvent casting and the anti-solvent based processing methods required large amounts of solvents that were not environmentally friendly. Therefore, it would be important to look at different techniques to process PHB without using large amounts of solvents.

RAF and interphase characterization: The interfacial interactions between the nanofiller and the matrix determined how the interphase was formed. Because of the high crystallinity of the PHB, the interphase between the CNC-PHB can play a huge role in the development of the macroscopic properties. It would be interesting to characterize the interphase that is formed as a result of different processing methods. In this thesis, only Flash DSC and other methods only observed macroscopic properties that resulted from this interphase, but it would be interesting to characterize the actual interphase through different techniques such as chemical force microscopy and nanoindentation.

APPENDIX. A

Table A.1.Summary of the parameters of the crystallization peak upon cooling for the anti-solvent processed samples

	AS				AS-CM			
	Onset (°C)	Width (°C)	Area (J/g)	Slope (W/(g·°C))	Onset (°C)	Width (°C)	Area (J/g)	Slope (W/(g·°C))
Neat PHB	94.5 ±0.1	10.6 ±0.1	58.7 ±2.1	-0.10 ±0.00	107.2 ±0.8	8.9 ±3.8	78.8 ±3.4	-0.37 ±0.20
0.5 wt.% CNC/PHB	113.3 ±0.5	5.3 ±0.2	80.3 ±8.1	-0.61 ±0.03	110.5 ±0.1	5.3 ±0.2	81.5 ±1.2	-0.65 ±0.04
1.0 wt. % CNC/PHB	113.3 ±0.5	4.9 ±0.1	74.1 ±3.3	-0.57 ±0.11	111.0 ±0.3	5.3 ±0.3	81.9 ±1.6	-0.65 ±0.07

Table A.2. Avrami analysis of the isothermal crystallization experiments of SC-H_2O from 110˚C to 120˚C

Sample		110	112	115	120
0.5 wt. % CNC/PHB	n	2.5	2.5	2.6	2.6
	k	0.0567	0.0246	0.0054	0.0015
	$t^{0.5}$	2.7	3.8	6.4	10.8
1.0 wt. % CNC/PHB	n	1.8	2.0	2.1	2.3
	k	0.3842	0.1394	0.0639	0.0063
	$t^{0.5}$	1.4	2.4	3.0	7.7

Table A.3. Modified Avrami analysis of the isothermal crystallization experiments for all processing methods 120˚C

		SC-EtOH	**SC-H_2O**	**AS**	**ASCM**
Neat PHB	n	1.09		1.19	1.25
	k	0.08		0.02	0.17
0.5 wt. % CNC/PHB	n	1.22	1.23	1.29	1.29
	k	0.11	0.05	0.37	0.20
1.0 wt. % CNC/PHB	n	1.26	1.21	1.22	1.26
	k	0.11	0.16	0.38	0.24

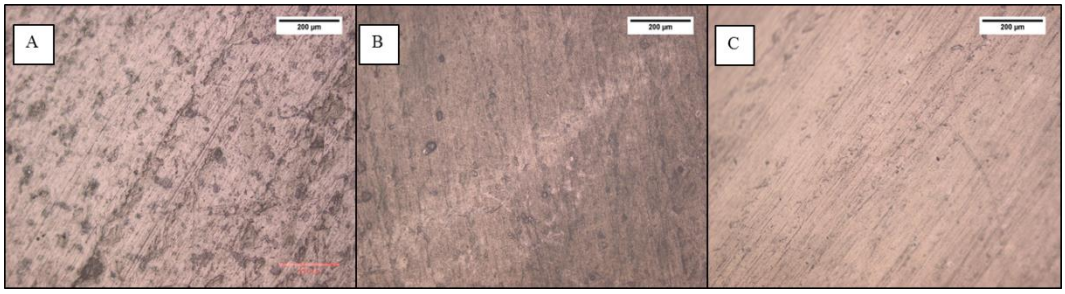

Figure A.1. Optical micrographs of SC w/EtOH samples: neat PHB (a), 0.5 wt.% CNC/PHB (b,) and 1.0wt.% CNC/PHB (c).

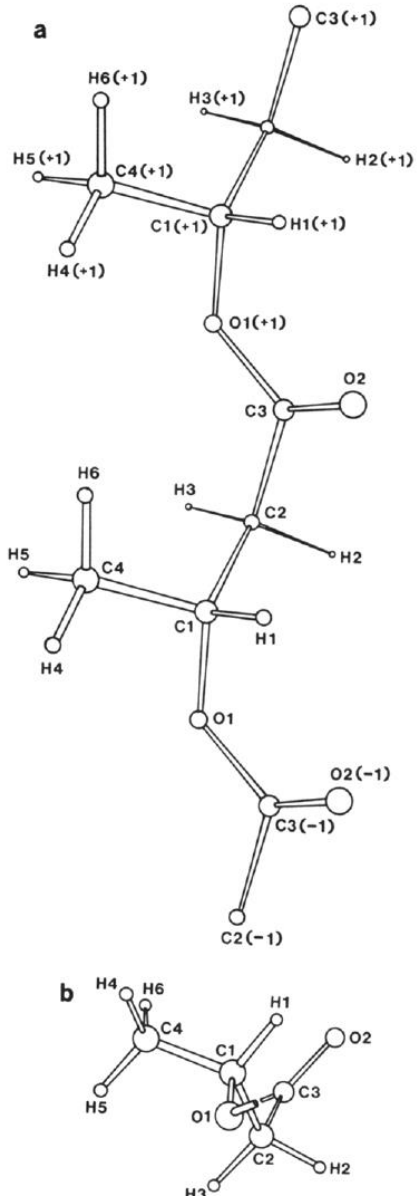

Figure A.2. Proposed chain conformation of the β- form of PHB a) perpendicular to the chain axis b) down the chain axis[215]

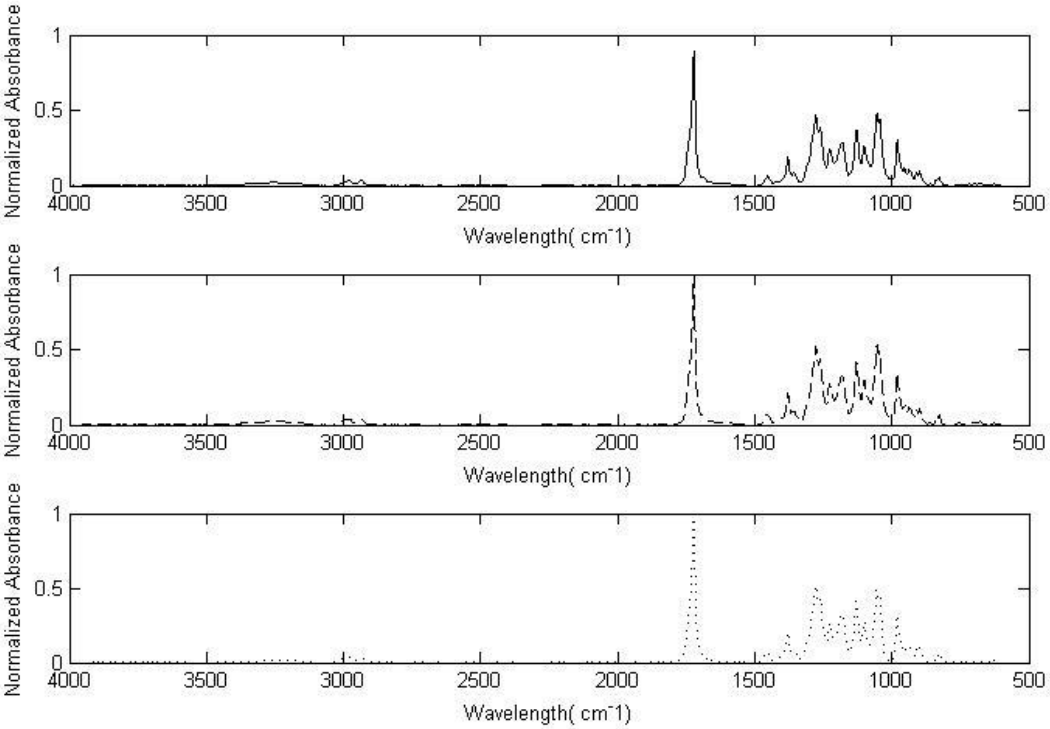

Figure A.3. FTIR spectra for SC-EtOH samples.

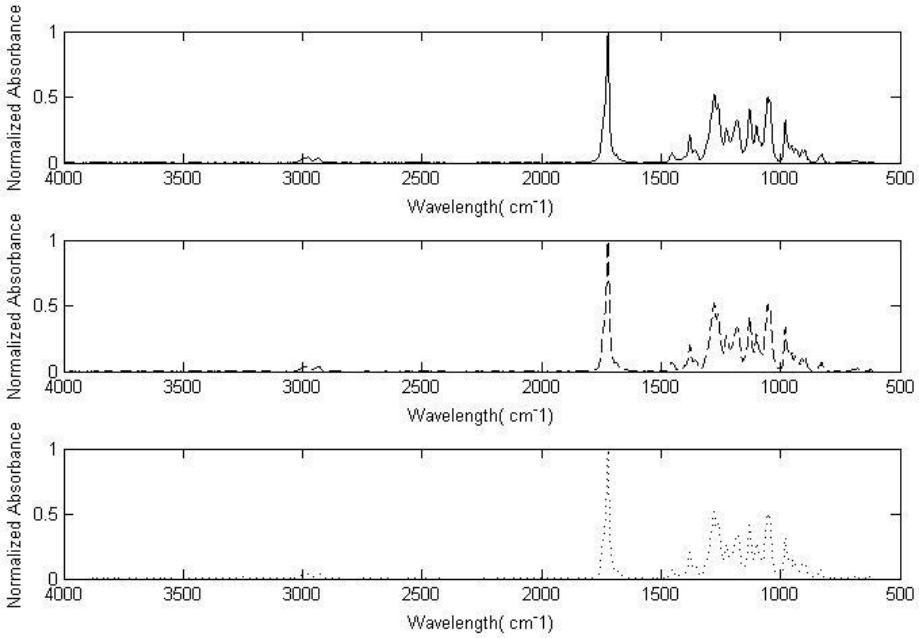

Figure A.4. FTIR for SC-H_2O samples.

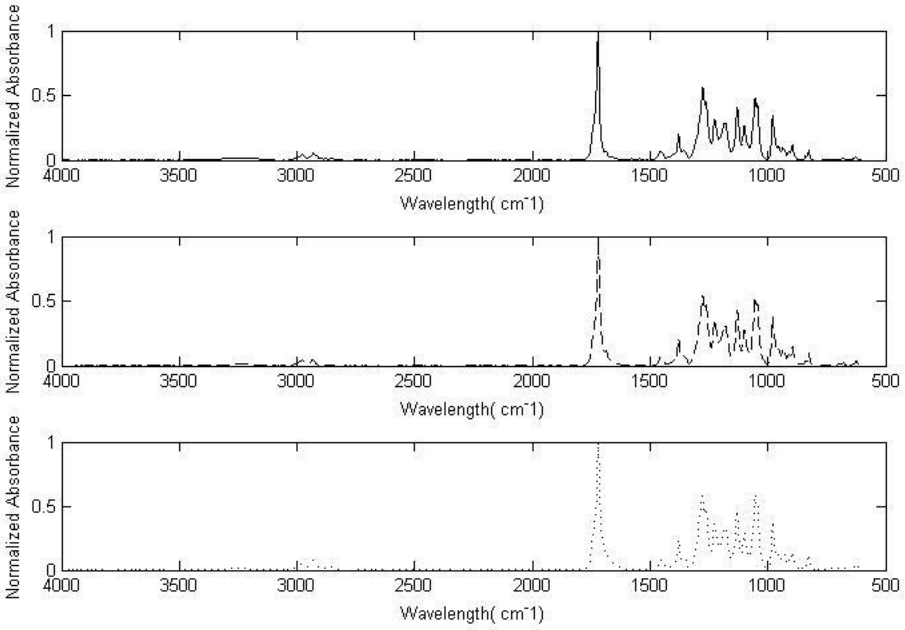

Figure A.5. FTIR spectra for the ASCM samples.

Table A.3. Band assignments for the for the neat PHB samples processed by SC w/EtOH, SC w/H20, and ASCM

Wavenumber(cm^{-1})			assignment
SC w/EtOH	SC w H20	ASCM	
3436	3436	3437	$\nu(OH\cdots O)$
		3008	$\nu(CH_3)$
2998	2996	2996	$\nu(CH_3)$
		2986	$\nu(CH_3)$
2976	2976	2977	$\nu(CH_2)$
2934	2935		
2875	2875	2875	$\nu(CH_2)$
1745	1745		
1724	1724	1724	$\nu_s(COO)$
	1687	1687	$\nu_s(COO)$
		1458	$\delta_{as}(CH_3)$
1452	1452	1453	$\delta_{as}(CH_3)$
		1445	$\delta_{as}(CH_2)$
	1403	1403	ω (CH2)
	1381		ω (CH2)
1379	1378		$\delta_s(CH_3)$
1347	1347		ν(C-O)
1304	1310		$\nu_s(COC)$
1300	1300		$\nu_s(COC)$
1184	1186		ν(C-C)+ω (CH2)
1134	1136		
1101	1101		$\nu_s(COC)$
1064	1055		
981	980		$\nu_s(COC)$
		954	$\nu_s(COC)$
		939	$\nu_s(COC)$
930	930		ν(C-C)
896	896	896	ν(C-C)
		839	$\rho(CH_2)$
826	826		ν(C-C)
754	754		
678	678		δ(COO) of the 3HB
624	624		γ(CO)
		599	γ(CO)
515	515	515	γ(CH)
459	459		δ(CCC)
		430	ρ(CCO)

REFERENCES

1. Krishnamoorti, R. & Vaia, R. A. Polymer nanocomposites. *Journal of Polymer Science Part B: Polymer Physics* **45,** 3252–3256 (2007).

2. Hussain, F. Review article: Polymer-matrix nanocomposites, processing, manufacturing, and application: an overview. *Journal of Composite Materials* **40,** 1511–1575 (2006).

3. Thostenson, E., Li, C. & Chou, T. Nanocomposites in context. *Composites Science and Technology* **65,** 491–516 (2005).

4. Moon, R. J., Martini, A., Nairn, J., Simonsen, J. & Youngblood, J. Cellulose nanomaterials review: structure, properties and nanocomposites. *Chemical Society Reviews* **40,** 3941–94 (2011).

5. Liu, H. & Brinson, L. Reinforcing efficiency of nanoparticles: A simple comparison for polymer nanocomposites. *Composites Science and Technology* **68,** 1502–1512 (2008).

6. Samir, M. A. S. A., Alloin, F. & Dufresne, A. Review of recent research into cellulosic whiskers, their properties and their application in nanocomposite field. *Biomacromolecules* **6,** 612–26 (2005).

7. Moniruzzaman, M. & Winey, K. I. Polymer nanocomposites containing carbon nanotubes. *Macromolecules* **39,** 5194–5205 (2006).

8. Song, J. H., Murphy, R. J., Narayan, R. & Davies, G. B. H. Biodegradable and compostable alternatives to conventional plastics. *Philosophical Transactions of the Royal Society of London. Series B, Biological Sciences* **364,** 2127–39 (2009).

9. Petersson, L., Kvien, I. & Oksman, K. Structure and thermal properties of poly(lactic acid)/cellulose whiskers nanocomposite materials. *Composites Science and Technology* **67,** 2535–2544 (2007).

10. Abdul Khalil, H. P. S., Bhat, A. H. & Ireana Yusra, A. F. Green composites from sustainable cellulose nanofibrils: A review. *Carbohydrate Polymers* **87,** 963–979 (2011).

11. Miloaga, D. G., Hosein, H. A., Misra, M. & Drzal, L. T. Crystallization of poly (3-hydroxybutyrate) by exfoliated graphite nanoplatelets. *Journal of Applied Polymer Science* **106,** 2548–2558 (2007).

12. Zhijiang, C., Guang, Y. & Kim, J. Biocompatible nanocomposites prepared by impregnating bacterial cellulose nanofibrils into poly(3-hydroxybutyrate). *Current Applied Physics* **11,** 247–249 (2011).

13. Morelius, E., Wolcott, M. & Holbery, J. Study of the poly(3-hydroxybutyrate-co-3-hydroxyvalerate)/cellulose nanowhisker composites prepared by solution casting and melt processing. *Journal of Composite Materials* **42,** 2629–2645 (2008).

14. Jonoobi, M. & Harun, J. Mechanical properties of cellulose nanofiber (CNF) reinforced polylactic acid (PLA) prepared by twin screw extrusion. *Composites Science and Technology* **70,** 1742–47 (2010).

15. Jalal Uddin, A., Araki, J. & Gotoh, Y. Toward "strong" green nanocomposites: polyvinyl alcohol reinforced with extremely oriented cellulose whiskers. *Biomacromolecules* **12,** 617–24 (2011).

16. Ljungberg, N., Cavaille, J. & Heux, L. Nanocomposites of isotactic polypropylene reinforced with rod-like cellulose whiskers. *Polymer* **47,** 6285–6292 (2006).

17. Chabert, E. *et al.* Filler–filler interactions and viscoelastic behavior of polymer nanocomposites. *Materials Science and Engineering: A* **381,** 320–330 (2004).

18. Fu, S., Feng, X., Lauke, B. & Mai, Y. Effects of particle size, particle/matrix interface adhesion and particle loading on mechanical properties of particulate–polymer composites. *Composites Part B Engineering* **39,** 933–961 (2008).

19. Usuki, A. & Kawasumi, M. Swelling behavior of montmorillonite cation exchanged for ω-amino acids by e-caprolactam. *Journal of Materials …* **8,** 1174–1178 (1993).

20. Kalaitzidou, K., Fukushima, H. & Drzal, L. T. A new compounding method for exfoliated graphite–polypropylene nanocomposites with enhanced flexural properties and lower percolation threshold. *Composites Science and Technology* **67,** 2045–2051 (2007).

21. Moniruzzaman, M., Du, F., Romero, N. & Winey, K. I. Increased flexural modulus and strength in SWNT/epoxy composites by a new fabrication method. *Polymer* **47,** 293–298 (2006).

22. Liu, Q. *et al.* Mechanical and Thermal Properties of Epoxy Resin Nanocomposites Reinforced with Graphene Oxide. *Polymer-Plastics Technology and Engineering* **51,** 251–256 (2012).

23. Quaresimin, M., Salviato, M. & Zappalorto, M. Fracture and interlaminar properties of clay-modified epoxies and their glass reinforced laminates. *Engineering Fracture Mechanics* **81,** 80–93 (2012).

24. Hsieh, A. J. *et al.* Mechanical response and rheological properties of polycarbonate layered-silicate nanocomposites. *Polymer Engineering and Science* **44,** 825–837 (2004).

25. Huang, C. J. *et al.* Cryogenic properties of SiO2/epoxy nanocomposites. *Cryogenics* **45,** 450–454 (2005).

26. Yang, J.-P., Yang, G., Xu, G. & Fu, S.-Y. Cryogenic mechanical behaviors of MMT/epoxy nanocomposites. *Composites Science and Technology* **67,** 2934–2940 (2007).

27. Phua, Y. J., Lau, N. S., Sudesh, K., Chow, W. S. & Mohd Ishak, Z. a. Biodegradability studies of poly(butylene succinate)/organo-montmorillonite nanocomposites under controlled compost soil conditions: Effects of clay loading and compatibiliser. *Polymer Degradation and Stability* **97,** 1345–1354 (2012).

28. Wang, S. *et al.* Characteristics and biodegradation properties of poly(3-hydroxybutyrate-co-3-hydroxyvalerate)/organophilic montmorillonite (PHBV/OMMT) nanocomposite. *Polymer Degradation and Stability* **87,** 69–76 (2005).

29. Pukanszky, B. Interfaces and interphases in multicomponent materials: past, present, future. *European Polymer Journal* **41,** 645–662 (2005).

30. Pukánszky, B. & Fekete, E. in *Mineral Fillers in Thermoplastics I SE - 3* (Jancar, J. *et al.*) **139,** 109–153 (Springer Berlin Heidelberg, 1999).

31. Dufresne, A. Dynamic mechanical analysis of the interphase in bacterial polyester/cellulose whiskers natural composites. *Composite Interfaces* **7,** 53–67 (2000).

32. Grady, B. P. Effects of carbon nanotubes on polymer physics. *Journal of Polymer Science Part B: Polymer Physics* **50,** 591–623 (2012).

33. Ciprari, D., Jacob, K. & Tannenbaum, R. Characterization of polymer nanocomposite interphase and its impact on mechanical properties. *Macromolecules* **39,** 6565–6573 (2006).

34. Ning, N. *et al.* Realizing the enhancement of interfacial interaction in semicrystalline polymer/filler composites via interfacial crystallization. *Progress in Polymer Science* **37,** 1425–1455 (2012).

35. Pukanszky, B. Effect of interfacial interactions on the deformation and failure properties of PP/CaCO3 composites. *New Polymeric Materials* **3,** 205–217 (1992).

36. Gong, L., Kinloch, I., Young, R. & Riaz, I. Interfacial stress transfer in a graphene monolayer nanocomposite. *Advanced Materials* **22,** 2694–2697 (2010).

37. Yang, J.-S., Yang, C.-L., Wang, M.-S., Chen, B.-D. & Ma, X.-G. Crystallization of alkane melts induced by carbon nanotubes and graphene nanosheets: a molecular dynamics simulation study. *Physical Chemistry Chemical Physics* **13,** 15476–15482 (2011).

38. Shi, X., Wang, J., Jiang, B. & Yang, Y. Influence of nanofiller dimensionality on the crystallization behavior of HDPE/carbon nanocomposites. *Journal of Applied Polymer Science* **128,** 3609–3618 (2013).

39. Schreiber, H. P. in *The Interfacial Interactions in Polymeric Composites SE - 2* (Akovali, G.) **230,** 21–59 (Springer Netherlands, 1993).

40. Kaur, J. Properties of Biologically Relevant Nanocomposties: Effects of Calcium Phosphate Nanoparticle Attributes and Biodegradable Polymer Morpholgy. *Engineering* (2010).

41. Avella, M., Cosco, S., Di Lorenzo, M. L., Di Pace, E. & Errico, M. E. Influence of CaCO3 nanoparticles shape on thermal and crystallization behavior of isotactic polypropylene based nanocomposites. *Journal of Thermal Analysis and Calorimetry* **80,** 131–136 (2005).

42. Avella, M. *et al.* Nucleation activity of nanosized CaCO3 on crystallization of isotactic polypropylene, in dependence on crystal modification, particle shape, and coating. *European Polymer Journal* **42,** 1548–1557 (2006).

43. Coleman, J. N. J., Khan, U., Blau, W. W. J., Gun'ko, Y. & Gun'ko, Y. K. Small but strong: A review of the mechanical properties of carbon nanotube–polymer composites. *Carbon* **44,** 1624–1652 (2006).

44. Móczó, J. & Pukánszky, B. Polymer micro and nanocomposites: Structure, interactions, properties. *Journal of Industrial and Engineering Chemistry* **14,** 535–563 (2008).

45. Wright, W. W. *Interfacial phenomena in composite materials*. *Polymer International* **24,** 125 (John Wiley & Sons, Ltd, 1991).

46. Bose, S., Bhattacharyya, A. R., Kodgire, P. V, Misra, A. & Pötschke, P. Rheology, morphology, and crystallization behavior of melt-mixed blends of polyamide6 and acrylonitrile-butadiene-styrene: Influence of reactive compatibilizer premixed with

multiwall carbon nanotubes. *Journal of Applied Polymer Science* **106,** 3394–3408 (2007).

47. Huang, J. *et al.* Organic–inorganic nanocomposites from cubic silsesquioxane epoxides: direct characterization of interphase, and thermomechanical properties. *Polymer* **46,** 7018–7027 (2005).

48. Sturcová, A., Davies, G. R. & Eichhorn, S. J. Elastic modulus and stress-transfer properties of tunicate cellulose whiskers. *Biomacromolecules* **6,** 1055–61 (2005).

49. Rusli, R., Shanmuganathan, K., Rowan, S. J., Weder, C. & Eichhorn, S. J. Stress transfer in cellulose nanowhisker composites--influence of whisker aspect ratio and surface charge. *Biomacromolecules* **12,** 1363–9 (2011).

50. Peresin, M. S., Habibi, Y., Zoppe, J. O., Pawlak, J. J. & Rojas, O. J. Nanofiber composites of polyvinyl alcohol and cellulose nanocrystals: manufacture and characterization. *Biomacromolecules* **11,** 674–81 (2010).

51. Kovačević, V., Lučić, S. & Leskovac, M. Morphology and failure in nanocomposites. Part I: Structural and mechanical properties. *Journal of Adhesion Science and Technology* **16,** 1343–1365 (2002).

52. Manias, E. Nanocomposites: Stiffer by design. *Nature Materials* **6,** 9–11 (2007).

53. Zeng, Q. H., Yu, a. B. & Lu, G. Q. Multiscale modeling and simulation of polymer nanocomposites. *Progress in Polymer Science* **33,** 191–269 (2008).

54. Du, F. *et al.* Nanotube Networks in Polymer Nanocomposites: Rheology and Electrical Conductivity. *Macromolecules* **37,** 9048–9055 (2004).

55. Bréchet, Y. *et al.* Polymer based nanocomposites: Effect of filler-filler and filler-matrix interactions. *Advanced Engineering Materials* **3,** 571 (2001).

56. Kashiwagi, T. *et al.* Relationship between dispersion metric and properties of PMMA/SWNT nanocomposites. *Polymer* **48,** 4855–4866 (2007).

57. De Souza Lima, M. M. & Borsali, R. Rodlike Cellulose Microcrystals: Structure, Properties, and Applications. *Macromolecular Rapid Communications* **25,** 771–787 (2004).

58. Hajji, P., Cavaille, J., Favier, V., Gauthier, C. & Vigier, G. Tensile behavior of nanocomposites from latex and cellulose whiskers. *Polymer Composites* **17,** 612–619 (2004).

59. Lim, S., Hyun, Y., Lee, C. & Choi, H. Preparation and characterization of microbial biodegradable poly (3-hydroxybutyrate)/organoclay nanocomposite. *Journal of materials science letters* 299–302 (2003). at <http://www.springerlink.com/index/M212004J5V72L479.pdf>

60. Suttiwijitpukdee, N., Sato, H., Zhang, J., Hashimoto, T. & Ozaki, Y. Intermolecular interactions and crystallization behaviors of biodegradable polymer blends between poly (3-hydroxybutyrate) and cellulose acetate butyrate studied by DSC , FT-IR , and WAXD. *Polymer* **52,** 461–471 (2011).

61. Pandey, J. K. *et al.* Preparation and structural evaluation of nano reinforced composites from cellulose whiskers of grass and biodegradable polymer matrix. *Journal of Composite Materials* **46,** 653–663 (2012).

62. D'Amico, D. a., Manfredi, L. B. & Cyras, V. P. Crystallization behavior of poly(3-hydroxybutyrate) nanocomposites based on modified clays: Effect of organic modifiers. *Thermochimica Acta* **544,** 47–53 (2012).

63. El-Hadi, A. M. Influence of microcrystalline cellulose fiber (MCCF) on the morphology of poly(3-hydroxybutyrate) (PHB). *Colloid and Polymer Science* **291,** 743–756 (2012).

64. Zhang, M. & Thomas, N. L. Preparation and Properties of Polyhydroxybutyrate Blended with Different Types of Starch. *Polymer* (2009). doi:10.1002/app

65. Androsch, R., Di Lorenzo, M. L., Schick, C. & Wunderlich, B. Mesophases in polyethylene, polypropylene, and poly(1-butene). *Polymer* **51,** 4639–4662 (2010).

66. Wunderlich, B. & Grebowicz, J. Thermotropic mesophases and mesophase transitions of linear, flexible macromolecules. *Advance in Polymer Science* **60,** 1–60 (1984).

67. McGenity, P., Hooper, J. & Paynter, C. Nucleation and crystallization of polypropylene by mineral fillers: relationship to impact strength. *Polymer* **33,** 5215–5224 (1992).

68. Wunderlich, B. The thermal properties of complex, nanophase-separated macromolecules as revealed by temperature-modulated calorimetry. *Thermochimica Acta* **403,** 1–13 (2003).

69. Auriemma, F., De Rosa, C. & Corradini, P. in *Interphases and Mesophases in Polymer Crystallization II SE - 107169* **181,** 1–74 (Springer Berlin Heidelberg, 2005).

70. Sirota, E. B. Polymer crystallization: Metastable mesophases and morphology. *Macromolecules* **40,** 1043–1048 (2007).

71. Mileva, D., Androsch, R., Zhuravlev, E., Schick, C. & Wunderlich, B. Formation and reorganization of the mesophase of random copolymers of propylene and 1-butene. *Polymer* **52,** 1107–1115 (2011).

72. Rosa, C. De, Guerra, G. & Petraccone, V. Temperature dependence of intramolecular disorder in the high-temperature phase of poly (tetrafluoroethylene)(phase I). *Macromolecules* **21,** 1174–1176 (1988).

73. Keum, J. K. *et al.* Crystallization and Transient Mesophase Structure in Cold-Drawn PET Fibers. *Macromolecules* **36,** 9873–9878 (2003).

74. Welsh, G., Blundell, D. & Windle, A. A transient mesophase on drawing polymers based on polyethylene terephthalate (PET) and polyethylene naphthoate (PEN). *Journal of materials science* **5,** 5225–5240 (2000).

75. Mileva, D., Androsch, R., Zhuravlev, E. & Schick, C. Critical rate of cooling for suppression of crystallization in random copolymers of propylene with ethylene and 1-butene. *Thermochimica Acta* **492,** 67–72 (2009).

76. Antipov, E. M. *et al.* Strain-induced mesophase and hard-elastic behaviour of biodegradable polyhydroxyalkanoates fibers. *Polymer* **47,** 5678–5690 (2006).

77. Wunderlich, B. Thermal properties of aliphatic nylons and their link to crystal structure and molecular motion. *Journal of Thermal Analysis and Calorimetry* **93,** 7–17 (2008).

78. Mileva, D., Androsch, R., Cavallo, D. & Alfonso, G. Structure formation of random isotactic copolymers of propylene and 1-hexene or 1-octene at rapid cooling. *European Polymer Journal* **48,** 1082–1092 (2012).

79. Schick, C., Wurm, A. & Mohammed, A. Formation and disappearance of the rigid amorphous fraction in semicrystalline polymers revealed from frequency dependent heat capacity. *Thermochimica Acta* **396,** 119–132 (2003).

80. Cole, K. C., Ajji, A. & Pellerin, É. New Insights into the Development of Ordered Structure in Poly(ethylene terephthalate). 1. Results from External Reflection Infrared Spectroscopy. *Macromolecules* **35,** 770–784 (2002).

81. Strobl, G. R. & Hagedorn, W. Raman spectroscopic method for determining the crystallinity of polyethylene. *Journal of Polymer Science: Polymer Physics Edition* **16,** 1181–1193 (1978).

82. Glotin, M. & Mandelkern, L. A Raman spectroscopic study of the morphological structure of the polyethylenes. *Colloid & Polymer Science* **260,** 182–192 (1982).

83. Androsch, R. Surface structure of folded-chain crystals of poly(R-3-hydroxybutyrate) of different chain length. *Polymer* **49,** 4673–4679 (2008).

84. Chen, H. & Cebe, P. Investigation of the Rigid Amorphous Fraction in Nylon-6. *Journal Of Thermal Analysis* **89,** 417–425 (2007).

85. Lorenzo, M. Di, Gazzano, M. & Righetti, M. The role of the rigid amorphous fraction on cold crystallization of poly (3-hydroxybutyrate). *Macromolecules* **41,** 5684–5691 (2012).

86. Androsch, R. & Wunderlich, B. The link between rigid amorphous fraction and crystal perfection in cold-crystallized poly(ethylene terephthalate). *Polymer* **46,** 12556–12566 (2005).

87. Schick, C. & Wurm, A. Vitrification and devitrification of the rigid amorphous fraction of semicrystalline polymers revealed from frequency-dependent heat capacity. *Colloid Polymer Science* **279,** 800–806 (2001).

88. Schick, C., Wurm, A. & Mohamed, A. Dynamics of reversible melting revealed from frequency dependent heat capacity. *Thermochimica Acta* **392-393,** 303–313 (2002).

89. Wu, Z., Zhou, C. & Zhu, N. The nucleating effect of montmorillonite on crystallization of nylon 1212/montmorillonite nanocomposite. *Polymer Testing* **21,** 479–483 (2002).

90. Pei, A., Zhou, Q. & Berglund, L. a. Functionalized cellulose nanocrystals as biobased nucleation agents in poly(l-lactide) (PLLA) – Crystallization and mechanical property effects. *Composites Science and Technology* **70,** 815–821 (2010).

91. Yu, H., Qin, Z. & Zhou, Z. Cellulose nanocrystals as green fillers to improve crystallization and hydrophilic property of poly(3-hydroxybutyrate-co-3-hydroxyvalerate). *Progress in Natural Science: Materials International* **21,** 478–484 (2011).

92. Koval'chuk, A. a. *et al.* Effect of carbon nanotube functionalization on the structural and mechanical properties of polypropylene/MWCNT composites. *Macromolecules* **41,** 7536–7542 (2008).

93. Mathot, V. *et al.* The Flash DSC 1, a power compensation twin-type, chip-based fast scanning calorimeter (FSC): First findings on polymers. *Thermochimica Acta* 1–10 (2011). doi:10.1016/j.tca.2011.02.031

94. Zhuravlev, E. & Schick, C. Fast scanning power compensated differential scanning nano-calorimeter: 2. Heat capacity analysis. *Thermochimica Acta* **505,** 14–21 (2010).

95. Tol, R. T., Minakov, A. A., Adamovsky, S. A., Mathot, V. B. F. & Schick, C. Metastability of polymer crystallites formed at low temperature studied by ultra fast calorimetry: Polyamide 6 confined in sub-micrometer droplets vs. bulk PA6. *Polymer* **47,** 2172–2178 (2006).

96. Mollova, A., Androsch, R. & Mileva, D. Effect of supercooling on crystallization of polyamide 11. *Macromolecules* (2013). doi:10.1021/ma302238r

97. Minakov, A., Mordvintsev, D. & Schick, C. Melting and reorganization of poly(ethylene terephthalate) on fast heating (1000 K/s). *Polymer* **45,** 3755–3763 (2004).

98. Cebe, P. *et al.* Beating the heat--fast scanning melts silk beta sheet crystals. *Nature* **3,** 1130 (2013).

99. Mileva, D., Androsch, R., Zhuravlev, E. & Schick, C. Morphology of mesophase and crystals of polyamide 6 prepared in a fast scanning chip calorimeter. *Polymer* **53,** 3994–4001 (2012).

100. Massam, J. & Pinnavaia, T. Clay nanolayer reinforcement of a glassy epoxy polymer. in *Materials Research Society Symposium Proceedings* **520,** 223–232 (1998).

101. Eichhorn, S. J. *et al.* Review: current international research into cellulose nanofibres and nanocomposites. *Journal of materials science* **45,** 1–33 (2010).

102. Hubbe, M. A., Rojas, O. J., Lucia, L. A. & Sain, M. Cellulosic nanocomposites: A review. *BioResources* **3,** 929–980 (2008).

103. Habibi, Y., Lucia, L. a & Rojas, O. J. Cellulose nanocrystals: chemistry, self-assembly, and applications. *Chemical Reviews* **110,** 3479–500 (2010).

104. Xu, S., Girouard, N., Schueneman, G., Shofner, M. L. & Meredith, J. C. Mechanical and thermal properties of waterborne epoxy composites containing cellulose nanocrystals. *Polymer* **54,** 6589–6598 (2013).

105. Favier, V. & Canova, G. Nanocomposite materials from latex and cellulose whiskers. *Polymers for Advanced Technologies* **6,** 351–355 (1995).

106. Pei, A., Malho, J.-M., Ruokolainen, J., Zhou, Q. & Berglund, L. a. Strong nanocomposite reinforcement effects in polyurethane eastomer with low volume fraction of cellulose nanocrystals. *Macromolecules* **44,** 4422–4427 (2011).

107. Shi, Q. *et al.* Mechanical properties and in vitro degradation of electrospun bio-nanocomposite mats from PLA and cellulose nanocrystals. *Carbohydrate Polymers* **90,** 301–308 (2012).

108. Ten, E., Jiang, L. & Wolcott, M. P. Crystallization kinetics of poly(3-hydroxybutyrate-co-3-hydroxyvalerate)/cellulose nanowhiskers composites. *Carbohydrate Polymers* **90,** 541–550 (2012).

109. Ten, E., Turtle, J., Bahr, D., Jiang, L. & Wolcott, M. Thermal and mechanical properties of poly(3-hydroxybutyrate-co-3-hydroxyvalerate)/cellulose nanowhiskers composites. *Polymer* **51,** 2652–2660 (2010).

110. Van den Berg, O., Capadona, J. R. & Weder, C. Preparation of homogeneous dispersions of tunicate cellulose whiskers in organic solvents. *Biomacromolecules* **8,** 1353–7 (2007).

111. Azizi Samir, M. A. S., Alloin, F., Sanchez, J.-Y., El Kissi, N. & Dufresne, A. Preparation of cellulose whiskers reinforced nanocomposites from an organic medium suspension. *Macromolecules* **37,** 1386–1393 (2004).

112. Gao, X., Chen, J.-C., Wu, Q. & Chen, G.-Q. Polyhydroxyalkanoates as a source of chemicals, polymers, and biofuels. *Current opinion in biotechnology* **22,** 768–74 (2011).

113. Lenz, R. W. & Marchessault, R. H. Bacterial polyesters: biosynthesis, biodegradable plastics and biotechnology. *Biomacromolecules* **6,** 1–8 (2005).

114. Alper, R., Lundgren, D. G., Marchessault, R. H. & Cote, W. A. Properties of poly-β-hydroxybutyrate. I. General considerations concerning the naturally occurring polymer. *Biopolymers* **1,** 545–556 (1963).

115. El-Hadi, A., Schnabel, R., Straube, E., Müller, G. & Riemschneider, M. Effect of Melt Processing on Crystallization Behavior and Rheology of Poly(3-hydroxybutyrate) (PHB) and its Blends. *Macromolecular Materials and Engineering* **287,** 363 (2002).

116. Xu, J. *et al.* In situ FTIR study on melting and crystallization of polyhydroxyalkanoates. *Polymer* **43,** 6893–6899 (2002).

117. Marchessault, R., Coulombe, S., Morikawa, H. & Okamura, K. Solid state properties of poly-β-hydroxybutyrate and of its oligomers. *Canadian Journal …* **59,** 38–44 (1981).

118. Suttiwijitpukdee, N., Sato, H., Unger, M. & Ozaki, Y. Effects of Hydrogen Bond Intermolecular Interactions on the Crystal Spherulite of Poly(3-hydroxybutyrate) and Cellulose Acetate Butyrate Blends: Studied by FT-IR and FT-NIR Imaging Spectroscopy. *Macromolecules* **45,** 2738–2748 (2012).

119. Jacquel, N. & Tajima, K. Nucleation mechanism of polyhydroxybutyrate and poly (hydroxybutyrate- • co- • hydroxyhexanoate) crystallized by orotic acid as a nucleating agent. *Journal of Applied Polymer Science* **115,** 705–715 (2010).

120. Sato, H., Murakami, R., Zhang, J. & Ozaki, Y. X-ray diffraction and infrared spectroscopy studies on crystal and lamellar structure and cho hydrogen bonding of biodegradable poly (hydroxyalkanoate). *Macromolecular Research* **14,** 408–415 (2006).

121. Savenkova, L. *et al.* Mechanical properties and biodegradation characteristics of PHB-based films. *Process Biochemistry* **35,** 573–579 (2000).

122. Furuhashi, Y., Imamura, Y., Jikihara, Y. & Yamane, H. Higher order structures and mechanical properties of bacterial homo poly(3-hydroxybutyrate) fibers prepared by cold-drawing and annealing processes. *Polymer* **45,** 5703–5712 (2004).

123. El-Shafee, E., Saad, G. R. & Fahmy, S. M. Miscibility , crystallization and phase structure of poly (3-hydroxybutyrate)/ cellulose acetate butyrate blends. *European Polymer Journal* **37,** 2091–2104 (2001).

124. Zhao, Q. & Chen, G. *Biodegradable PHB/PEG Derivatives and Their Degradation Behavior*. *New Frontiers in Polymer Research* 99–124 (Nova Science Publishers, Inc, 2006).

125. Barham, P. Nucelation behaviour of poly-3-hydroxy-butyrate. *Journal of Materials Science* **19,** 3826–3834 (1984).

126. Organ, S. J. & Barham, P. J. On the equilibrium melting temperature of polyhydroxybutyrate. *Polymer* **34,** 2169–2174 (1993).

127. Gunaratne, L. M. W. K., Shanks, R. a. & Amarasinghe, G. Thermal history effects on crystallisation and melting of poly(3-hydroxybutyrate). *Thermochimica Acta* **423,** 127–135 (2004).

128. Gunaratne, L. M. W. K. & Shanks, R. a. Thermal memory of poly(3-hydroxybutyrate) using temperature-modulated differential scanning calorimetry. *Journal of Polymer Science Part B: Polymer Physics* **44,** 70–78 (2006).

129. Kai, W., He, Y. & Inoue, Y. Fast crystallization of poly(3-hydroxybutyrate) and poly(3-hydroxybutyrate-co-3-hydroxyvalerate) with talc and boron nitride as nucleating agents. *Polymer International* **54,** 780–789 (2005).

130. Puente, J. A. S., Esposito, A., Chivrac, F. & Dargent, E. Effect of boron nitride as a nucleating agent on the crystallization of bacterial poly(3-hydroxybutyrate). *Journal of Applied Polymer Science* **128,** 2586–2594 (2013).

131. Jacquel, N., Lo, C.-W., Wei, Y.-H., Wu, H.-S. & Wang, S. S. Isolation and purification of bacterial poly(3-hydroxyalkanoates). *Biochemical Engineering Journal* **39,** 15–27 (2008).

132. Di Lorenzo, M. L. & Righetti, M. C. Effect of thermal history on the evolution of crystal and amorphous fractions of poly[(R)-3-hydroxybutyrate] upon storage at ambient temperature. *European Polymer Journal* **49,** 510–517 (2013).

133. Righetti, M. C., Tombari, E. & Di Lorenzo, M. L. The Role of the Crystallization Temperature on the Nanophase Structure Evolution of Poly[(R)-3-hydroxybutyrate]. *The Journal of Physical Chemistry B* **117,** 12303–12311 (2013).

134. Koning, G. J. M. De & Lemstra, P. J. Crystallization phenomena in bacterial poly [(R)-3- hydroxybutyrate]: 2 .Embrittlement and rejuvenation. *Polymer* **34,** 4089–4094 (1993).

135. Withey, R. & Hay, J. The effect of seeding on the crystallisation of poly (hydroxybutyrate), and co-poly (hydroxybutyrate-co-valerate). *Polymer* **40,** 5147–5152 (1999).

136. Birley, C. *et al.* Morphology of single crystals of poly (hydroxybutyrate) and copolymers of hydroxybuty rate and hydroxyvalerate. *Journal of materials science* **30,** 633–638 (1995).

137. Grassie, N., Murray, E. & Holmes, P. The thermal degradation of poly (-(D)-Î²-hydroxybutyric acid): part 2—changes in molecular weight. *Polymer degradation and stability* **6,** 95–103 (1984).

138. Koller, M., Bona, R., Chiellini, E. & Braunegg, G. Extraction of short-chain-length poly-[(R)-hydroxyalkanoates] (scl-PHA) by the “anti-solvent” acetone under elevated temperature and pressure. *Biotechnology letters* **35,** 1023–8 (2013).

139. Wang, Y., Dave, R. N. & Pfeffer, R. Polymer coating/encapsulation of nanoparticles using a supercritical anti-solvent process. *The Journal of supercritical fluids* **28,** 85–99 (2004).

140. Cocero, M. J., Martín, Á., Mattea, F. & Varona, S. Encapsulation and co-precipitation processes with supercritical fluids: Fundamentals and applications. *The Journal of Supercritical Fluids* **47,** 546–555 (2009).

141. Thiering, R., Dehghani, F. & Foster, N. R. Current issues relating to anti-solvent micronisation techniques and their extension to industrial scales. *The Journal of Supercritical Fluids* **21,** 159–177 (2001).

142. Mago, G., Kalyon, D. M. & Fisher, F. T. Membranes of polyvinylidene fluoride and PVDF nanocomposites with carbon nanotubes via immersion precipitation. *Journal of Nanomaterials* **2008,** 17 (2008).

143. Koning, G. J. M. De, Lemstra, P. J., Hill, D. J. T., Carswell, T. G. & Donnell, J. H. O. Ageing phenomena in bacterial poly [(R) - 3 - hydro xybutyrate] 1 . A study on the mobility in poly [(R) -3-hydroxybutyrate] powders by monitoring the radical decay with temperature after ~ -radiolysis at 77 K. *Polymer* **33,** 3295–3297 (1992).

144. Di Lorenzo, M. L. *et al.* Optimization of Melting Conditions of Poly(3-Hydroxybutyrate). in *AIP Conference Proceedings* **1042,** 96–98 (Aip, 2008).

145. Chen, C. Nonisothermal crystallization and melting behavior of poly(3-hydroxybutyrate) and maleated poly(3-hydroxybutyrate). *European Polymer Journal* **38,** 1663–1670 (2002).

146. Righetti, M. C. & Di Lorenzo, M. L. Melting temperature evolution of non-reorganized crystals. Poly(3-hydroxybutyrate). *Thermochimica Acta* **512,** 59–66 (2011).

147. Kaur, J., Lee, J. H. & Shofner, M. L. Influence of polymer matrix crystallinity on nanocomposite morphology and properties. *Polymer* **52,** 4337–4344 (2011).

148. Flores, a., Pieruccini, M., Nöchel, U., Stribeck, N. & Baltá Calleja, F. J. Recrystallization studies on isotropic cold-crystallized PET: Influence of heating rate. *Polymer* **49,** 965–973 (2008).

149. Buzarovska, a., Bogoeva-Gaceva, G., Grozdanov, a. & Avella, M. Crystallization behavior of polyhydroxybutyrate in model composites with kenaf fibers. *Journal of Applied Polymer Science* **102,** 804–809 (2006).

150. Ramsay, J. A., Berger, E. & Voyer, R. Extraction of poly-3-hydroxybutyrate using chlorinated solvents. *Biotechnology …* **8,** 589–594 (1994).

151. Stageman, J. F. Extraction process US Patent 4,562,245 A.

152. Suttiwijitpukdee, N. & Sato, H. Effects of Intermolecular Hydrogen Bondings on Isothermal Crystallization Behavior of Polymer Blends of Cellulose Acetate Butyrate and Poly (3-hydroxybutyrate). *Macromolecules* **44,** 3467–3477 (2011).

153. González-Obeso, C., Song, W. L., Rodríguez-Pérez, M. a. & Mano, J. F. Superhydrophobic to Superhydrophylic Biomimetic Poly(3-Hydroxybutyrate) Surfaces Made by Phase Inversion. *Materials Science Forum* **730-732,** 44–49 (2012).

154. D'Amico, D. A., Manfredi, L. B. & Cyras, V. P. Relationship between thermal properties, morphology, and crystallinity of nanocomposites based on polyhydroxybutyrate. *Journal of Applied Polymer Science* **123,** 200–208 (2012).

155. Sudesh, K., Abe, H. & Doi, Y. Synthesis, structure and properties of polyhydroxyalkanoates: biological polyesters. *Progress in Polymer Science* **25,** 1503–1555 (2000).

156. Zhang, J., Sato, H., Noda, I. & Ozaki, Y. Conformation Rearrangement and Molecular Dynamics of Poly(3-hydroxybutyrate) during the Melt-Crystallization Process Investigated by Infrared and Two-Dimensional Infrared Correlation Spectroscopy. *Macromolecules* **38,** 4274–4281 (2005).

157. Iordanskii, A. L., Kamaev, P. P. & Zaikov, G. E. Immobilization Influence on the Water Sorption and Diffusion in Poly (3-hydroxybutyrate). 981–985 (1998).

158. Vyazovkin, S. *et al.* ICTAC Kinetics Committee recommendations for performing kinetic computations on thermal analysis data. *Thermochimica Acta* **520,** 1–19 (2011).

159. Di Lorenzo, M. L. & Silvestre, C. Non-isothermal crystallization of polymers. *Progress in Polymer Science* **24,** 917–950 (1999).

160. Jing, X. & Qiu, Z. Effect of low thermally reduced graphene loadings on the crystallization kinetics and morphology of biodegradable poly (3-hydroxybutyrate). *Industrial & Engineering Chemistry Research* **51,** 13686–13691 (2012).

161. Lorenzo, A. T., Arnal, M. L., Albuerne, J. & Müller, A. J. DSC isothermal polymer crystallization kinetics measurements and the use of the Avrami equation

to fit the data: Guidelines to avoid common problems. *Polymer Testing* **26,** 222–231 (2007).

162. Gilman, J. Flammability and thermal stability studies of polymer layered-silicate (clay) nanocomposites1. *Applied Clay Science* **15,** 31–49 (1999).

163. Hobbs, J. & Barham, P. J. The effect of water on the crystallization of thin films of poly (hydroxybutyrate). *Polymer* **38,** 3879–3883 (1997).

164. Lauzier, C., Revol, J.-F. & Marchessault, R. H. Topotactic crystallization of isolated poly(β-hydroxybutyrate) granules from Alcaligenes eutrophus. *FEMS Microbiology Letters* **103,** 299–310 (1992).

165. Murakami, R., Sato, H., Dybal, J., Iwata, T. & Ozaki, Y. Formation and stability of β-structure in biodegradable ultra-high-molecular-weight poly(3-hydroxybutyrate) by infrared, Raman, and quantum chemical calculation studies. *Polymer* **48,** 2672–2680 (2007).

166. Sato, H. *et al.* Thermal Behavior and Molecular Interaction of Poly(3-hydroxybutyrate-co-3-hydroxyhexanoate) Studied by Wide-Angle X-ray Diffraction. *Macromolecules* **37,** 3763–3769 (2004).

167. Sato, H. *et al.* Infrared Spectroscopy Studies of CH···O Hydrogen Bondings and Thermal Behavior of Biodegradable Poly(hydroxyalkanoate). *Macromolecules* **37,** 7203–7213 (2004).

168. Yoshie, N., Oike, Y., Kasuya, K., Doi, Y. & Inoue, Y. Change of surface structure of poly(3-hydroxybutyrate) film upon enzymatic hydrolysis by PHB depolymerase. *Biomacromolecules* **3,** 1320–6 (2002).

169. Lagaron, J.-M. The factor group splitting phenomenon: a vibrational spectroscopy approach to assess polymer crystallinity and crystalline density. *Macromolecular Symposia* **184,** 19–36 (2002).

170. Lambeek, G. & Schouten, J. Structural Study of Langmuir-Blodgett Mono- and Multilayers of Poly(.beta.-hydroxybutyrate). *Macromolecules* **28,** 2023–2032 (1996).

171. Wróbel-Kwiatkowska, M. *et al.* Poly-3-hydroxy butyric acid interaction with the transgenic flax fibers: FT-IR and Raman spectra of the composite extracted from a GM flax. *Spectrochimica acta. Part A, Molecular and biomolecular spectroscopy* **73,** 286–94 (2009).

172. Kondo, T. The assignment of IR absorption bands due to free hydroxyl groups in cellulose. *Cellulose* (1997). at <http://link.springer.com/article/10.1023/A:1018448109214>

173. Chang, L. & Woo, E. Crystallization of poly (3-hydroxybutyrate) with stereocomplexed polylactide as biodegradable nucleation agent. *Polymer Engineering & Science* **57,** 1413–1419 (2012).

174. Kim, G.-M., Michler, G. H., Ania, F. & Calleja, F. J. B. Temperature dependence of polymorphism in electrospun nanofibres of PA6 and PA6/clay nanocomposite. *Polymer* **48,** 4814–4823 (2007).

175. Lincoln, D. M., Vaia, R. A., Wang, Z. G., Hsiao, B. S. & Krishnamoorti, R. Temperature dependence of polymer crystalline morphology in nylon 6/montmorillonite nanocomposites. *POLYMER* **42,** 9975–9985 (2001).

176. Koller, M., Niebelschütz, H. & Braunegg, G. Strategies for recovery and purification of poly[(R)-3-hydroxyalkanoates] (PHA) biopolyesters from surrounding biomass. *Engineering in Life Sciences* **13,** 549–562 (2013).

177. Van Herwaarden, A. W. Overview of calorimeter chips for various applications. *Thermochimica Acta* **432,** 192–201 (2005).

178. Iervolino, E. *et al.* Temperature calibration and electrical characterization of the differential scanning calorimeter chip UFS1 for the Mettler-Toledo Flash DSC 1. *Thermochimica Acta* 1–7 (2011). doi:10.1016/j.tca.2011.01.023

179. Van Herwaarden, A. W. *et al.* Design, performance and analysis of thermal lag of the UFS1 twin-calorimeter chip for fast scanning calorimetry using the Mettler-Toledo flash DSC 1. *Thermochimica Acta* 1–7 (2011). doi:10.1016/j.tca.2011.05.025

180. Kolesov, I., Mileva, D., Androsch, R. & Schick, C. Structure formation of polyamide 6 from the glassy state by fast scanning chip calorimetry. *Polymer* **52,** 5156–5165 (2011).

181. Minakov, a a, Wurm, a & Schick, C. Superheating in linear polymers studied by ultrafast nanocalorimetry. *The European physical journal. E, Soft matter* **23,** 43–53 (2007).

182. De Koning, G. J. M., Scheeren, a. H. C., Lemstra, P. J., Peeters, M. & Reynaers, H. Crystallization phenomena in bacterial poly[(R)-3-hydroxybutyrate]: 3. Toughening via texture changes. *Polymer* **35,** 4598–4605 (1994).

183. Heo, K. *et al.* Structural evolution in microbial polyesters. *The journal of physical chemistry. B* **112,** 4571–82 (2008).

184. Fujita, M. & Sawayanagi, T. Synchrotron SAXS and WAXS Studies on Changes in Structural and Thermal Properties of Poly Single Crystals during Heating. *Macromolecular …* 678–683 (2005). doi:10.1002/marc.200500030

185. Righetti, M. & Lorenzo, M. Nonlinear determination of the equilibrium melting temperature from initial nonreorganized crystals of poly (3- • hydroxybutyrate). *Polymer Engineering & Science* 1–8 (2012). doi:10.1002/pen

186. Ziaee, Z. & Supaphol, P. Non-isothermal melt- and cold-crystallization kinetics of poly(3-hydroxybutyrate). *Polymer Testing* **25,** 807–818 (2006).

187. Srubar, W. V. *et al.* Characterizing the effects of ambient aging on the mechanical and physical properties of two commercially available bacterial thermoplastics. *Polymer Degradation and Stability* **97,** 1922–1929 (2012).

188. Zia, Q., Mileva, D. & Androsch, R. Rigid Amorphous Fraction in Isotactic Polypropylene. *Macromolecules* **41,** 8095–8102 (2008).

189. Pizzoli, M., Scandola, M. & Ceccorulli, G. Crystallization and Melting of Isotactic Poly(3-hydroxy butyrate) in the Presence of a Low Molecular Weight Diluent. *Macromolecules* **35,** 3937–3941 (2002).

190. Pearce, R., Brown, G. R. & Marchessault, R. Crystallization kinetics in blends of isotactic and atactic poly (-hydroxybutyrate). *Polymer* **35,** 3984–3989 (1994).

191. Barham, P. J. & Keller, A. Crystallization and morphology of a bacterial thermoplastic: poly-3-hydroxybutyrate. *Journal of Materials Science* **19,** 2791–2794 (1984).

192. Lorenzo, M. L. Di, Righetti, M. C. & Gazzano, M. Competition between crystallization and vitrification of the rigid amorphous fraction in poly(3-hydroxybutyrate). in 36–38 (2012). doi:10.1063/1.4738390

193. Sargsyan, A., Tonoyan, A., Davtyan, S. & Schick, C. The amount of immobilized polymer in PMMA SiO2 nanocomposites determined from calorimetric data. *European Polymer Journal* **43,** 3113–3127 (2007).

194. Bassett, D. . & Patel, D. Isothermal lamellar thickening and the distribution of thermal stability in spherulitic isotactic poly(4-methylpentene-1). *Polymer* **35,** 1855–1862 (1994).

195. Kim, J. *et al.* Nonisothermal Crystallization Behaviors of Nanocomposites Prepared by In Situ Polymerization of High-Density Polyethylene on Multiwalled Carbon Nanotubes. *Macromolecules* **43,** 10545–10553 (2010).

196. Adhikari, a. R., Lozano, K. & Chipara, M. Non-isothermal crystallization kinetics of polyethylene/carbon nanofiber composites. *Journal of Composite Materials* **46,** 823–832 (2011).

197. Chung, J. S. & Cebe, P. Melting behaviour of poly (phenylene sulphide): 1. Single-stage melt crystallization. *Polymer* **33,** 2312–2324 (1992).

198. Wurm, A. & Schick, C. Development of thermal stability of polymer crystals during isothermal crystallisation. *e-Polymers* 1–15 (2002).

199. Scandola, M., Ceccorulli, G. & Pizzoli, M. The physical aging of bacterial poly(D-β-hydroxybutyrate). *Die Makromolekulare Chemie, Rapid Communications* **10,** 47–50 (1989).

200. Schick, C. in *Perkin Elmer Application Notes* (2009).

201. Androsch, R., Radusch, H.-J. & Funari, S. S. Crystallization, glass transition and morphology of (R)-3-hydroxybutyrate oligomers. *European Polymer Journal* **43,** 4961–4974 (2007).

202. Di Lorenzo, M. L. & Righetti, M. C. Evolution of crystal and amorphous fractions of poly[(R)-3-hydroxybutyrate] upon storage. *Journal of Thermal Analysis and Calorimetry* **112,** 1439–1446 (2012).

203. Xu, H. & Cebe, P. Heat Capacity Study of Isotactic Polystyrene : Dual Reversible Crystal Melting and Relaxation of Rigid Amorphous Fraction. 2797–2806 (2004).

204. Wunderlich, B. Reversible crystallization and the rigid–amorphous phase in semicrystalline macromolecules. *Progress in Polymer Science* **28,** 383–450 (2003).

205. Ziaee, Z. & Supaphol, P. Non-isothermal melt- and cold-crystallization kinetics of poly(3-hydroxybutyrate). *Polymer Testing* **25,** 807–818 (2006).

206. Mileva, D. *et al.* Crystallization of a polyamide 6/montmorillonite nanocomposite at rapid cooling. *Macromolecular Materials and Engineering* (2012). doi:10.1002/mame.201200253

207. Sternstein, S. S. & Zhu, A.-J. Reinforcement Mechanism of Nanofilled Polymer Melts As Elucidated by Nonlinear Viscoelastic Behavior. *Macromolecules* **35,** 7262–7273 (2002).

208. Schick, C. & Donth, E. Characteristic length of glass transition: experimental evidence. *Physica Scripta* **423,** (1991).

209. Pramoda, K. P., Hussain, H., Koh, H. M., Tan, H. R. & He, C. B. Covalent bonded polymer–graphene nanocomposites. *Journal of Polymer Science Part A: Polymer Chemistry* **48,** 4262–4267 (2010).

210. Priya, L. & Jog, J. P. Intercalated poly(vinylidene fluoride)/clay nanocomposites: Structure and properties. *Journal of Polymer Science Part B: Polymer Physics* **41,** 31–38 (2003).

211. Priya, L. & Jog, J. P. Poly(vinylidene fluoride)/clay nanocomposites prepared by melt intercalation: Crystallization and dynamic mechanical behavior studies. *Journal of Polymer Science Part B: Polymer Physics* **40,** 1682–1689 (2002).

212. Grunert, M. & Winter, W. Nanocomposites of Cellulose Acetate Butyrate Reinforced with Cellulose Nanocrystals. *Journal of Polymers and the Environment* **10,** 27–30 (2002).

213. Kumagai, Y. & Kanesawa, Y. Enzymatic degradation of microbial poly (3-hydroxybutyrate) films. *Die Makromolekulare Chemie* **57,** 53–57 (1992).

214. Gatenholm, P. & Mathiasson, A. Biodegradable natural composites. II. Synergistic effects of processing cellulose with PHB. *Journal of applied polymer …* **51,** 1231–1237 (1994).

215. Orts, W., Marchessault, R. & Blum, H. observation of Strain- Induced B Form in Poly(B-hydroxyalkanoates). *Macromolecules* **23,** 5368–5370 (1990).